Doctoral Thesis

Metal-Organic Frameworks for Catalysis and Sensing: Fragmented Ligand Installation on MOF-74 and D_2O Sensing of MIL-53(In)-$(OH)_2$

Jaewoong Lim

Department of Chemistry

Ulsan National Institute of Science and Technology

2021

Metal-Organic Frameworks for Catalysis and Sensing: Fragmented Ligand Installation on MOF-74 and D_2O Sensing of MIL-53(In)-$(OH)_2$

Jaewoong Lim

Department of Chemistry

Ulsan National Institute of Science and Technology

Metal-Organic Frameworks for Catalysis and Sensing: Fragmented Ligand Installation on MOF-74 and D_2O Sensing of MIL-53(In)-$(OH)_2$

A thesis/dissertation submitted to
Ulsan National Institute of Science and Technology
in partial fulfillment of the
requirements for the degree of
Doctor of Philosophy

Jaewoong Lim

06.16.2021 of submission

Approved by

Advisor

Myoung Soo Lah

Metal-Organic Frameworks for Catalysis and Sensing: Fragmented Ligand Installation on MOF-74 and D_2O Sensing of MIL-53(In)-$(OH)_2$

Jaewoong Lim

This certifies that the thesis/dissertation of Jaewoong Lim is approved.

06.16.2021 of submission

Signature

Advisor: Myoung Soo Lah

Signature

Wonyoung Choe

Signature

Hoi Ri Moon

Signature

Jaeheung Cho

Signature

Min Kim

*three signatures total in case of masters

Abstract

Metal-organic frameworks (MOFs) are porous crystalline materials composed of metal ions or clusters coordinated to organic ligands. Various metal ions and different organic ligands induces different topology, pore size and chemical properties of the MOFs. Such MOFs were able to predict and design the structures, resulting in 90,000 MOFs synthesized until 2020. However, the new MOFs are limited to synthesize by using common materials. To overcome the limit, modified MOFs were introduced by defective MOFs (DEMOFs) and post-synthetic modification (PSM). These MOFs provided the new active sites, some increasing the porosity, which can be applied in additional application such as gas storage, catalysts and sensors.

In the first part of the thesis, the functionalized defect-engineered MOF-74 (DEMOF-74) has been introduced by install fragmented ligand. MOF-74 is one-dimensional porous materials and the organic linkers are connected between infinite metal rod. Due to stable and potential active metal sites, MOF-74 was attractive materials for various application. However, because of the ligand and structure limitation, the additional functional groups were difficult to introduced in frameworks. Herein, DEMOF-74 was synthesized by fragmented ligands, salicylic acid with various functional groups including amino, hydroxyl, formyl groups, that can be installed in frameworks up to 40 %, increasing the porosity for N_2, CO_2 and H_2 gases.

The second part of the thesis demonstrates amine-tagged fragmented ligand installation for the covalent modification of MOF-74. MOF-74 is one of the most explored MOFs, but its functionalization is limited to the dative PSM of the monodentate solvent site. Owing to the nature of the organic ligand and framework structure of MOF-74, the covalent PSM of MOF-74 is very demanding. Herein, we report, for the first time, the covalent PSM of amine-tagged defective Ni-MOF-74, which is prepared by *de novo* solvothermal synthesis using aminosalicylic acid as a functionalized fragmented organic ligand. The covalent PSM of the amino group generates metal-binding sites, and subsequent post-synthetic metalation with Pd(II) ions affords Pd(II)-incorporated Ni-MOF-74 catalyst. This catalyst exhibits highly efficient, size-selective, and recyclable catalytic activity for the Suzuki–Miyaura cross-coupling reaction. This strategy is also useful for the covalent modification of amine-tagged defective Ni_2(DOBPDC), an expanded analog of MOF-74.

The last part of the thesis includes the fluorescence sensing of H_2O in D_2O using H_2BDC-$(OH)_2$@MIL-53(In)-$(OH)_2$. MIL-53(In)-$(OH)_2$ synthesized using mixed solvent, H_2O and DMF, (**MIL-53-H/DMF**), is unstable in water which does not include free ligand in the pore. **MIL-53-H/DMF** when dispersed in water, spits into micro-sized and nanoparticles. Two types of particles induce different fluorescence emission in H_2O and D_2O because of the different binding mode. In order to stabilize MIL-53(In)-$(OH)_2$,

MIL-53-H was synthesized using only H_2O as the synthesis solvent. **MIL-53-H** that includes removable free ligands ($H_2BDC\text{-}(OH)_2$) is stable in H_2O and air and showed the efficient fluorescence sensing properties for the ratiometric detection of H_2O and D_2O.

Table of Contents

List of Figures

Figure 2.12. PXRD patterns of (a) **5-fSA$_x$** and (b) **3-hSA$_x$**.

Figure 2.13. ^{1}H NMR spectrum of (a) **3-aSA$_{0.04}$(9/1)**, (b) **3-aSA$_{0.18}$(7/3)**, and (c) **3-aSA$_{0.46}$(5/5).**

Figure 2.14. ^{1}H NMR spectrum of (a) **5-aSA$_{0.08}$(9/1)**, (b) **5-aSA$_{0.20}$(7/3)**, and (c) **5-aSA$_{0.33}$(5/5).**

Figure 2.15. ^{1}H NMR spectrum of (a) **5-fSA$_{0.08}$(9/1)**, (b) **5-fSA$_{0.21}$(7/3)**, and (c) **5-fSA$_{0.39}$(5/5).**

Figure 2.16. ^{1}H NMR spectrum of (a) **3-hSA$_{0.06}$(9/1)**, (b) **3-hSA$_{0.17}$(7/3)**, and (c) **3-hSA$_{0.42}$(5/5).**

Figure 2.17. PXRD patterns of not incorporated fragmented linkers, **4-aSA(7/3)**, **4-hSA(7/3)** and **6-hSA(7/3)**.

Figure 2.18. ^{1}H NMR spectrum of (a) **4-aSA(7/3)**, (b) **4-hSA(7/3)**, and (c) **6-hSA(7/3).**

Figure 2.19. SEM images of Ni-MOF-74 and **SA$_x$**. (a, b) Ni-MOF-74, (c, d) **SA$_{0.02}$**, (e, f) **SA$_{0.09}$**, (g, h) **SA$_{0.22}$**, and (i, j) **SA$_{0.36}$**.

Figure 2.20. SEM images of **2-hNA$_x$**. (a, b) **2-hNA$_{0.06}$**, (c, d) **2-hNA$_{0.17}$**, and (e, f) **2-hNA$_{0.29}$**.

Figure 2.21. SEM images of **3-aSA$_x$**. (a, b) **3-aSA$_{0.04}$**, (c, d) **3-aSA$_{0.18}$**, and (e, f) **3-aSA$_{0.46}$**.

Figure 2.22. SEM images of **5-aSA$_x$**. (a, b) **5-aSA$_{0.08}$**, (c, d) **5-aSA$_{0.20}$**, and (e, f) **5-aSA$_{0.33}$**.

Figure 2.23. SEM images of **5-fSA$_x$**. (a, b) **5-fSA$_{0.08}$**, (c, d) **5-fSA$_{0.21}$**, and (e, f) **5-fSA$_{0.39}$**.

Figure 2.24. SEM images of **3-hSA$_x$**. (a, b) **3-hSA$_{0.06}$**, (c, d) **3-hSA$_{0.21}$**, and (e, f) **3-hSA$_{0.42}$**.

Figure 2.25. TGA of (a) **SA$_x$**, (b) **2-hNA$_x$**, (c) **3-aSA$_x$**. (d) **5-aSA$_x$** (e) **5-fSA$_x$** and (f) **3-hSA$_x$**.

Figure 2.26. PXRD patterns of **3-aSA$_{0.18}$** and **5-aSA$_{0.20}$** soaked in H_2O for 4 d.

Figure 2.27. N_2 sorption isotherms of pristine MOF-74 and **SA$_x$** at 77 K. and (b) NLDFT pore size distribution of the pristine MOF-74 and **SA$_x$**.

Figure 2.28. N_2 sorption isotherms of pristine MOF-74 and **2-hNA$_x$** at 77 K. and (b) NLDFT pore size distribution of the pristine MOF-74 and **2-hNA$_x$**.

Figure 2.29. N_2 sorption isotherms of pristine MOF-74 and **5-fSA$_x$** at 77 K. and (b) NLDFT pore size distribution of the pristine MOF-74 and **5-fSA$_x$**.

Figure 2.30. N_2 sorption isotherms of pristine MOF-74 and **3-hSA$_x$** at 77K. and (b) NLDFT pore size distribution of the pristine MOF-74 and **3-hSA$_x$**.

Figure 2.31. N_2 sorption isotherms of pristine MOF-74 and **3-aSA$_x$** at 77 K. and (b) NLDFT pore size distribution of the pristine MOF-74 and **3-aSA$_x$**.

Figure 4.11. MIL-53-H/DMF for ratiometric fluorescence sensing for H_2O in D_2O. (b) Peak intensity from deconvolution of two emission peaks in each ratio of H_2O contents in D_2O.

Figure 4.12. (a)N_2 at 77 K and (b) CO_2 at 195 K adsorption of **MIL-53-H/DMF** before and after soaking in H_2O.

Figure 4.13. H_2O adsorption of pristine **MIL-53-H/DMF** and after H_2O treatment of **MIL-53-H/DMF**.

Figure 4.14. Ball and stick diagrams of the single-crystal structure of **MIL-53-H** (a) Framework showing a 1D rhomboidal channel in c-axis view (b) A wall generated by ligands of the BDC-$(OH)_2$ units between 1D rods.

Figure 4.15. PXRD patterns of **MIL-53-H** and **MIL-53-H/DMF** as-synthesized (assyn), upon activation and in H_2O.

Figure 4.16. Optical image of before and after **MIL-53-H** soaked in H_2O. scale bar is 10 μm.

Figure 4.17. FT-IR of H_2BDC-$(OH)_2$, **MIL-53-H**, **MIL-53-H/DMF** and **MIL-53-D**.

Figure 4.18. TGA of **MIL-53-H** and **MIL-53-H/DMF** in air.

Figure 4.19. (a) PXRD and (b) FT-IR of **MIL-53-H** in methanol.

Figure 4.20. FT-NMR of (a) H_2BDC-$(OH)_2$ dissolved in CD_3OD (b) **MIL-53-H** soaked in CD_3OD (c) **MIL-53-H/DMF** soaked in CD_3OD. H_2BDC-$(OH)_2$ was encapsulated in **MIL-53-H**, but not encapsulated in **MIL-53-H/DMF**.

Figure 4.21. PXRD of **MIL-53-H** in acetone.

Figure 4.22. PXRD of **MIL-53-H** in different activation temperature for dried and H_2O soaking.

Figure 4.23. FT-IR of **MIL-53-H** in different activation temperature.

Figure 4.24. (a) N_2 sorption isotherm at 77K and (b) CO_2 at 195K sorption isotherm of **MIL-53-H** and **MIL-53-H/DMF**.

Figure 4.25. H_2O adsorption of **MIL-53-H** and **MIL-53-H/DMF**.

Figure 4.26. Absorbance spectrum of **MIL-53-H** and **MIL-53-H/DMF** in H_2O.

Figure 4.27. (a) Fluorescence spectrum of **MIL-53-H** sample in D_2O with different H_2O contents (b) The fluorescence maximum intensity with H_2O contents in D_2O.

Figure 4.28. The fluorescence photo image of **MIL-53-H** from H_2O to D_2O in different ratio.

Figure 4.29. Solid fluorescence of **MIL-53-H** and **MIL-53-H/DMF.**

List of Tables

Chapter I

General Introduction of Metal-Organic Framework

1.1 Metal-Organic Frameworks

In the past decades, metal-organic frameworks (MOFs) have been researched as the one of the most important porous materials.[1,2] MOFs are built using metal ions or clusters coordinated with organic ligands, which result in crystalline porous materials (**Figure 1.1**). The secondary building unit (SBU) constructed by metal ion or cluster are connected by the organic unit, that results in the various framework topology.[3] Maintaining the same topology, isoreticular MOFs gave a new class of porous materials by using different metals or expanding the organic linkers with additional phenyl units or including various functional groups (**Figure 1.2**).[4] As the consequence, over 90,000 MOFs were reported by combining metal nodes and organic ligands and 500,000 MOFs were predicted.[5] Moreover, the altered MOFs (defect engineering,[6] post-synthesis modification[7] and hierarchical assemblies[8]) provided new opportunities resulting in flexible materials, tuning the porosity and additional functionalities. The designed MOFs are used in practical applications such as gas adsorption,[9] separations,[10] catalyses,[11] chemical sensing,[12] proton conductivity,[13] and biomedical[14] (**Figure 1.3**).

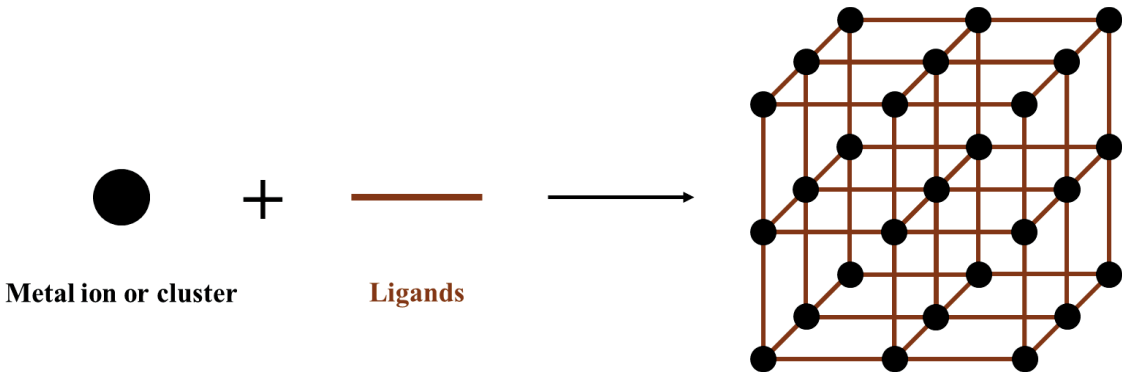

Figure 1.1 Scheme of MOFs synthesis using metal ion and organic ligands.

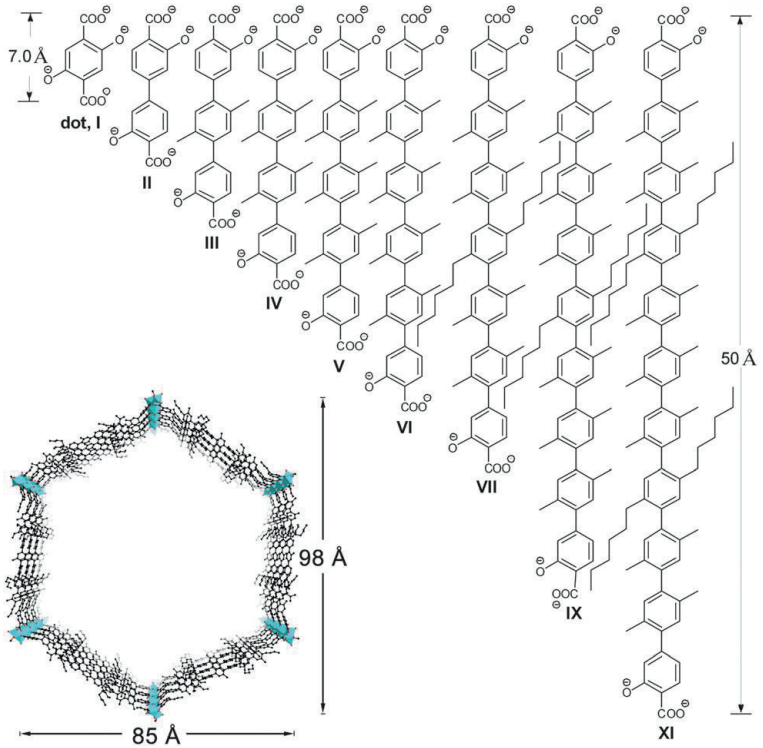

Figure 1.2 Isoreticular MOFs with different metal or organic linkers.[4]

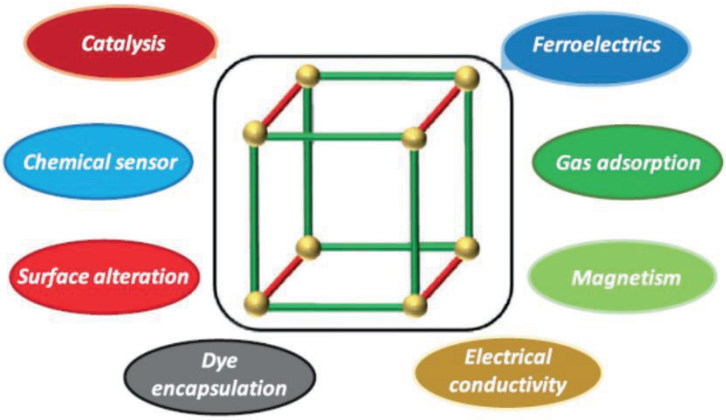

Figure 1.3 Different applications of MOFs explored.[15]

1.2 Defect-engineered MOFs

Defect crystal is the imperfect crystal including structure irregularities or disorders in real crystals. The control of defect give rise to change in the chemical and physical properties and functions. Defect-engineered MOFs (DEMOFs) is focused concept for tuning the materials that give new opportunities exhibiting various porosity,[20] functional groups[21] and catalytic sites.[22] The strategy of synthesis DEMOFs are *de novo* synthesis (mixed linker, modulator, control the crystal growth) and post synthetic treatment (mechanical, acid/base treatment, SALE/SALI and harsh activation) (**Figure 1.4**).[23]

Mixed linker approach is used to synthesize MOF using the mixture of original linker and fragmented linkers, which provide additional porosity and functional groups for catalytic sites. In addition, in order to match the charge of ligands, either metal is reduced, or metal (or metal clusters) are removed. The mixture of BTC and fragmented linker in HKUST-1 showed that depending the amount of the introduced fragmented linkers, Cu^{2+} is reduced to Cu^{1+}, Cu^{2+} ion is removed or cluster is released. The mixed linker approach has been mostly reported by cluster based MOFs like HKUST-1, UIO-66 and MOF-5. Meanwhile, the rod MOF are rarely reported such as MOF-74 because the rod net is too stable to remove metal in DEMOFs synthesis.

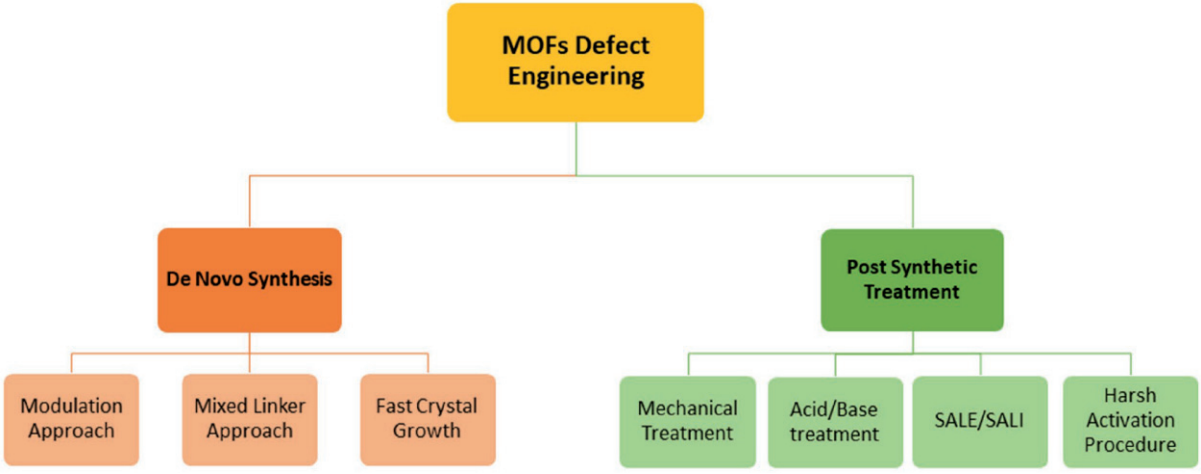

Figure 1.4. Representation of procedure to create defects in MOFs.[18]

1.3 Post-synthetic modification

Post-synthetic modification (PSM) of MOFs gave the opportunites to alter the structure and properties of MOFs. PSM are classified as dative PSM, postsynthetic deprotection (PSD) and covalent PSM (**Figure1.5**).[7] Dative PSM refers to the strategy of attaching orgamic molecules to unsaturated metal sites through coordination bond.[21] MOF-74[22,23], HKUST-1[24] and MOF-808[25] have the open metal sites at SBUs after removing the bound solvent. Amine, pyridine based molecues are coordinated and result in introducing base sites, hydrogen bond affinities and pore tuning for application as proton conductors,[22,25] gas and chemical separation.[23] Alternatively, PSD strategy is the cleavage of a chemical bond of protected fucntional groups.[26] Some linkers are unstable in special sovlothermal condtion so the protecting groups were used in primary and removed postsynthetic procedure.

Covalent PSM used the reaction between functional group in ligands and reagent via covalent bond. This strategy is useful approach for providing metal installation sites and new functional groups. Most of the studies were conducted in the MOFs made using ditopic linkers (BDC^{2-}, $BPDC^{2-}$) that are commocially available including functional groups.[27,28] Amine-tagged MOFs were the representive strategy for covalent PSM, for example, amine groups were combined with aldehyde forming imine bond and with carboxylate forming amide bond. Yaghi and co-workers introduced the Pd incorporated isoreticular UMCM-1 in which NH_2-BDC^{2-} was reacted with 2-pyridinecarboyxladehyde to give metal incorporated sites.[29] Whereas, since tritopic linkers (BTC^{3-}, BTB^{3-}) and tetratopic linkers ($DOBDC^{4-}$, $DOBPDC^{4-}$) were difficult to synthesize the functionized ligands, the few covalent PSM cases were reported.[30,31]

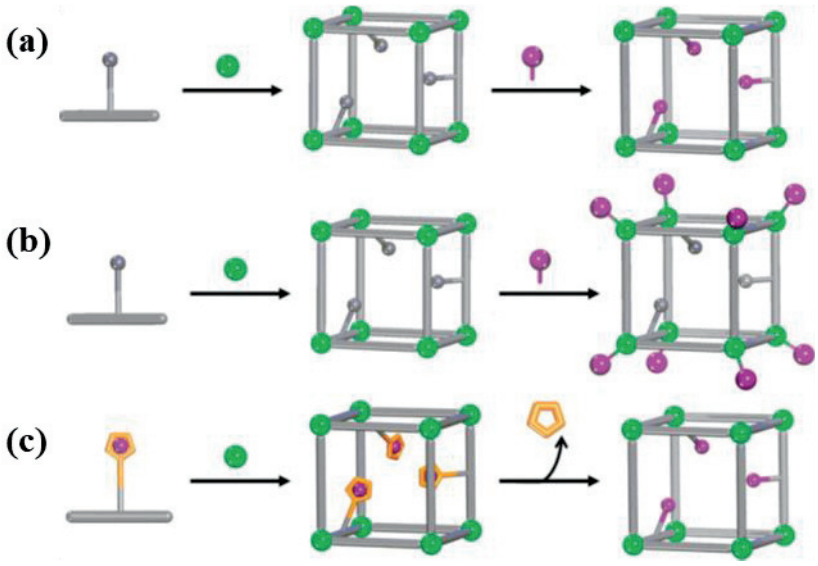

Figure 1.5. General approach for (a) covalent PSM, (b) dative PSM, and (c) PSD.[7]

1.4 Flexible MOFs

Flexible MOFs, also called soft porous crystals, are structural changes without bond breaking in external stimuli such as guest molecules, heat, pressure and light (**Figure 1.6**).[32,33] MOFs contain guest molecules in their pores, among which flexible MOFs undergo structural changes when guest molecules are removed. Based on the guest removal phenomenon, flexible MOFs are classified as breathing, swelling, linker rotation and subnetwork displacement.[34,35,36] Since the flexibility can be controlled, frameworks are studied in a variety of application such as gas adsorption, separation and sensors by controlling the pore.

Breathing behavior are sometimes based on host-guest interaction and guest-guest interaction representatively known through MIL-53.[37,38] The cooperative effect of metal nodes and organic linker is lead to the structure transformation from open pore state (op) to close pore state (cp). Flexibility can be controlled by functional groups in linker, type and amount of guest molecules and crystal sizes as the result of change in the host-guest and guest interactions. The proper rigidity control is especially a critical issue for gas storage and separation.

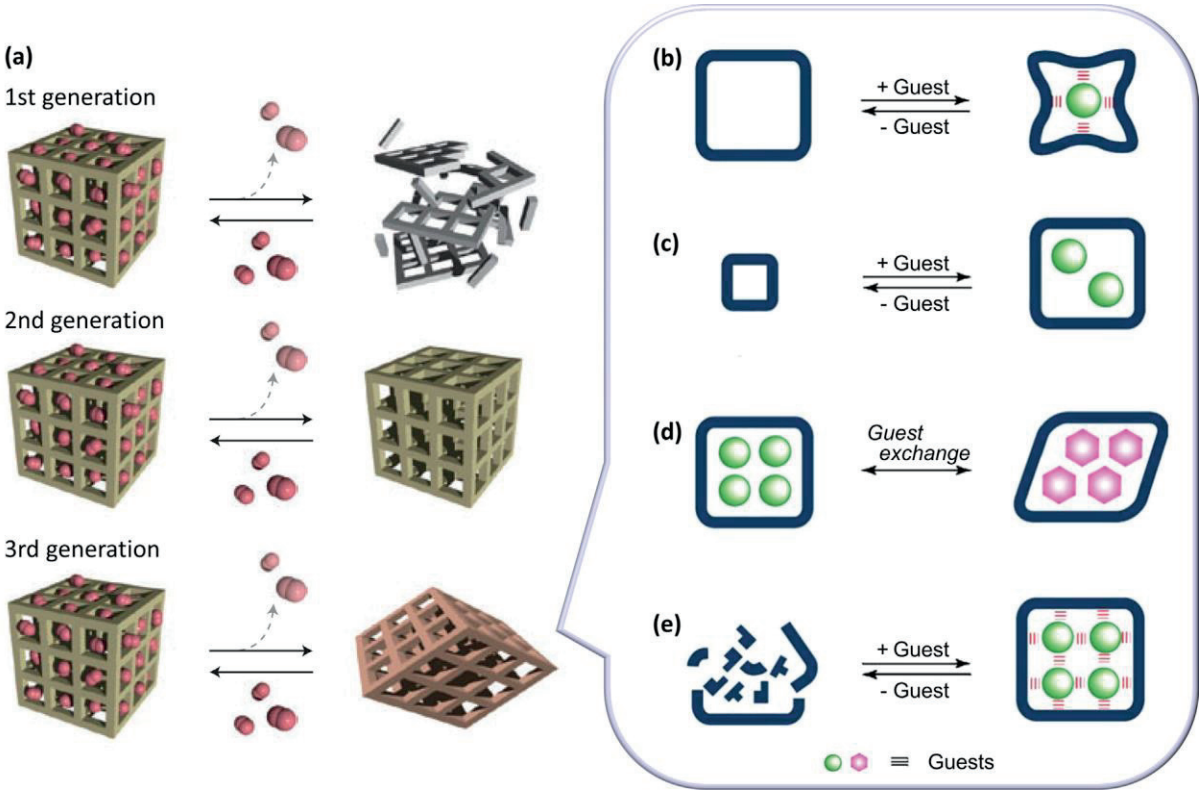

Figure 1.6. MOFs are classified as 1st, 2nd and 3rd generation. (b)~(e) the classification of dynamic structures behaviors upon adsorption/desorption of guest molecules.[32]

1.5 References

1. Furukawa, H.; Cordova, K. E.; Keeffe, M. O.; Yaghi, O. M. The Chemistry and Applications of Metal-Organic Frameworks. *Science* **2013**, 341, 1230444.
2. Férey, G. Hybrid porous solids: past, present, future. *Chem. Soc. Rev*. **2008**, 37, 191-214.
3. Guillerm, V.; Kim, D.; Eubank, J. F.; Luebke, R.; Liu, X.; Adil, K.; Lah, M. S.; Eddaoudi, M. A supermolecular building approach for the design and construction of metal–organic frameworks. *Chem. Soc. Rev*. **2014**, 43, 6141-6172.
4. Lu, W.; Wei, Z.; Gu, Z.-Y.; Liu, T.-F.; Park, J.; Park, J.; Tian, J.; Zhang, M.; Zhang, Q.; Ill, T. G.; Bosch, M.; Zhou, H.-C. Tuning the structure and function of metal–organic frameworks *via* linker design. *Chem. Soc. Rev*. **2014**, 43, 5561-5593.
5. Moosavi, S. M.; Nandy, A.; Jablonka, K. M.; Ongari, D.; Janet, J. P.; Boyd, P. G.; Lee, Y.; Smit, B.; Kulik, H. J. Understanding the diversity of the metal-organic framework ecosystem. *Nat. Commun*. **2020**, 11, 4068.
6. Fang, Z.; Bueken, B.; De Vos, D. E.; Fischer, R. A. Defect-Engineered Metal-Organic Frameworks. *Angew. Chem. Int. Ed*. **2015**, 54, 7234-7254.
7. Cohen, S. M. Postsynthetic Methods for the Functionalization of Metal-Organic Frameworks. *Chem. Rev*. **2012**, 112, 970-1000.
8. Feng, L.; Wang, K.-Y.; Powell, J.; Zhou, H.-C. Controllable Synthesis of Metal-Organic Frameworks and Their Hierarchical Assemblies. *Matter*. **2019**, 1, 801-824.
9. Li, J.; Bhatt, P. M.; Li, J.; Eddaoudi, M.; Liu, Y. Recent Progress on Microfine Design of Metal–Organic Frameworks: Structure Regulation and Gas Sorption and Separation. *Adv. Mater*. **2020**, 32, 2002563.
10. Li, J.-R.; Sculley, J.; Zhou, H.-C. Metal-Organic Frameworks for Separations. *Chem. Rev*. **2012**, 112, 869-932.
11. Wei, Y.-S.; Zhang, M.; Zou, R.; Xu, Q. Metal−Organic Framework-Based Catalysts with Single Metal Sites. *Chem. Rev*. **2020**, 120, 12089-12174.
12. Kreno, L. E.; Leong, K.; Farha, O. K.; Allendorf, M.; Duyne, R. P. V.; Hupp, J. T. Metal-Organic Frameworks Materials as Chemical Sensors. *Chem. Rev*. **2012**, *112*, 1105–1125.
13. Lim, D.-W.; Kitagawa. Proton Transport in Metal-Organic Frameworks. *Chem. Rev*. **2020**, *120*, 8416−8467.
14. Horcajada, P.; Gref, R.; Baati, T.; Allan, P. K.; Maurin, G.; Couvreur, P.; Férey, G.; Morris, R. E.; Serre, C. Metal-Organic Frameworks in Biomedicine. *Chem. Rev*. **2012**, *112*, 1232–1268.
15. Fang, Z.; Dürholt, J. P.; Kauer, M.; Zhang, W.; Lochenie, C.; Jee, B.; Albada, B.; Metzler-Nolte, N.; Pöppl, A.; Weber, B.; Muhler, M.; Wang, Y.; Schmid, R.; Fischer, R. A. Structural Complexity

in Metal−Organic Frameworks: Simultaneous Modification of Open Metal Sites and Hierarchical Porosity by Systematic Doping with Defective Linkers. *J. Am. Chem. Soc*. **2014**, 136, 9627-9636.

16. Lim, J.; Lee, S.; Ha, H.; Seong, J.; Jeong, S.; Kim, M.; Baek, S. B.; Lah, M. S. Amine-Tagged Fragmented Ligand Installation for Covalent Modification of MOF-74. *Angew. Chem. Int. Ed*. **2021**, 60, 9296-9300.
17. Kozachuk, O.; Luz, I.; Xamena, F. X. L.; Noei, H.; Kauer, M.; Albada, H. B.; Bloch, E. D.; Marler, B.; Wang, Y.; Muhler, M.; Fischer, R. A. Multifunctional, Defect-Engineered Metal–Organic Frameworks with Ruthenium Centers: Sorption and Catalytic Properties. *Angew. Chem. Int. Ed*. **2014**, 53, 7058-7062.
18. Dissegna, S.; Epp, K.; Heinz, W. R.; Kieslich, G.; Fischer, R. A. Defective Metal-Organic Frameworks. *Adv. Mater*. **2018**, 30, 1704501.
19. Shearer, G. C.; Chavan, S.; Bordiga, S.; Svelle, S.; Olsbye, U.; Lillerud, K. P. Defect Engineering: Tuning the Porosity and Composition of the Metal−Organic Framework UiO-66 via Modulated Synthesis. *Chem. Mater*. **2016**, 28, 3749-3761.
20. Choi, K. M.; Jeon, H. J.; Kang, J. K.; Yaghi, O. M. Heterogeneity within Order in Crystals of a Porous Metal-Organic Framework. *J. Am. Chem. Soc*. **2011**, 133, 11920-11923.
21. Kökçam-Demir, Ü.; Goldman, A.; Esrafili, L.; Gharib, M.; Morsali, A.; Weingart, O.; Janiak, C. Coordinatively unsaturated metal sites (open metal sites) in metal–organic frameworks: design and applications. *Chem. Soc. Rev*. **2020**, 49, 2751-2798.
22. Sarango-Ramírez, M. K.; Lim, D.-W.; Kolokolov, D. I.; Khudozhitkov, A. E.; Stepanov, A. G.; Kitagawa, H. Superprotonic Conductivity in Metal–Organic Framework via Solvent-Free Coordinative Urea Insertion. *J. Am. Chem. Soc*. **2020**, 142, 6861-6865.
23. Kim, J. Y.; Balderas-Xicohténcatl, R.; Zhang, L.; Kang, S. G.; Hirscher, M.; Oh, H.; Moon, H. R. Exploiting Diffusion Barrier and Chemical Affinity of Metal–Organic Frameworks for Efficient Hydrogen Isotope Separation. *J. Am. Chem. Soc*. **2017**, 139, 15135-15141.
24. Ingleson, M. J.; Heck, R.; Gould, J. A.; Rosseinsky, M. J. Nitric Oxide Chemisorption in a Postsynthetically Modified Metal-Organic Framework. *Inorg. Chem*. **2009**, 48, 9986-9988.
25. Sharma, A.; Lim, J.; Jeong, S.; Won, S.; Seong, J.; Lee, S.; Kim, Y. S.; Baek, S. B.; Lah, M. S. Superprotonic Conductivity of MOF-808 Achieved by Controlling the Binding Mode of Grafted Sulfamate. *Angew. Chem. Int. Ed*. **2021**, 60,
26. Yamada, T.; Kitagawa, H. Protection and Deprotection Approach for the Introduction of Functional Groups into Metal-Organic Frameworks. *J. Am. Chem. Soc*. **2009**, 131, 6312-6313.
27. Yin, Z.; Wan, S.; Yang, J.; Kurmoo, M.; Zeng, M.-H.; Recent advances in post-synthetic modification of metal–organic frameworks: New types and tandem reactions. *Coord. Chem. Rev*. **2019**, 378, 500-512.

28. Wang. Z.; Cohen, S. M.; Tandem Modification of Metal-Organic Frameworks by a Postsynthetic Approach. *Angew. Chem. Int. Ed*. **2008**, 47, 4699-4702.
29. Doonan, C. J.; Morris, W.; Furukawa, H.; Yaghi, O. M. Isoreticular Metalation of Metal-Organic Frameworks. *J. Am. Chem. Soc*. **2009**, 131, 9492-9493.
30. Peikert, K.; Hoffmann, F.; Fröba, M. Amino substituted $Cu_3(btc)_2$: a new metal–organic framework with a versatile functionality. *Chem. Commum*. **2012**, 48, 11196-11198.
31. Helten, S.; Sahoo, B.; Müller, P.; Janßen- Müller, D.; Klein, N.; Grünker, R.; Bon, V.; Glorius, F.; Kaskel, S.; Senkovska, I. Functional group tolerance in BTB-based metal-organic frameworks (BTB - benzene-1,3,5-tribenzoate). *Microporous and Mesoporous Mater*. **2015**, 216, 42-50.
32. Horike, S.; Shimomura, S.; Kitagawa, S.; Soft porous crystals. *Nat. Chem.* **2009**, 1, 695-704.
33. Schneemann, A.; Bon, V.; Schwedler, I.; Senkovska, I.; Kaskel, S.; Fischer, R. A. Flexible metal-organic frameworks. *Chem. Soc. Rev*. **2014**, 43, 6062-6096.
34. Férey, G.; Serre, C. Large breathing effects in three-dimensional porous hybrid matter: facts, analyses, rules and consequences. *Chem. Soc. Rev*. **2009**, 38, 1380-1399.
35. Krause, S.; Hosono, N.; Kitagawa, S. Chemistry of Soft Porous Crystals: Structural Dynamics and Gas Adsorption Properties. *Angew. Chem. Int. Ed*. **2020**, 59, 153235-15341.
36. Lee, J. H.; Jeoung, S.; Chung. Y. G.; Moon, H. R. Elucidation of flexible metal-organic frameworks: Research progresses and recent developments. *Coord. Chem. Rev*. **2019**, 389, 161-188.
37. Serre, C.; Millange, F.; Thouvenot, C.; Noguès, M.; Marsolier, G.; Louër, D.; Férey, G. Very Large Breathing Effect in the First Nanoporous Chromium(III)-Based Solids: MIL-53 or $Cr^{III}(OH)\cdot\{O_2C{-}C_6H_4{-}CO_2\}\cdot\{HO_2C{-}C_6H_4{-}CO_2H\}_x\cdot H_2O_y$. *J. Am. Chem. Soc*. **2002**, 124, 13519-13526.
38. Loiseau, T.; Serre, C.; Huguenard, C.; Fink, G.; Taulelle, F.; Henry, M.; Bataille, T.; Férey, G. A Rationale for the Large Breathing of the Porous Aluminum Terephthalate (MIL-53) Upon Hydration. *Chem. Eur. J*. **2004**, 10, 1373-1382.

Chapter II

Functionalized Defect-Engineered MOF-74 by Fragmented Linker Installation

2.1 Introduction

MOF-74 is one-dimensional hexagonal channel structure including the high density of potential unsaturated metal sites.[1,2] Infinite metal chains are connected by linker (2,5-dihydroxyl-1,4-benzenedicarboxylate, $DOBDC^{4-}$) in which one metal cation is coordinated with five oxygen of linker and other one solvent site. MOF-74, known as $M_2(DOBDC)$, have been able to synthesize using various 2+ metal ions (M: Mg, Ca, Mn, Fe, Co, Ni, Zn) and depending on the metal types, MOF-74 exhibits inherent properties, stability, catalytic activity and interaction with open metal sites and guest molecules in frameworks.[3-11] Owing to the diverse characteristics of MOF-74, it is focused in various applications such as gas storage,[2,4] separations,[8] catalysts,[6,9] electrochemistry[10] and proton conductors.[11]

Isoreticular MOF was the designed structure with extending different length of organic ligand and introducing functional groups into ligands.[12-16] The chemical moieties of MOFs are converted by functional groups such as amine, halide, hydroxyl, sulfuric and thiol that enhanced the gas and metal ion affinity, catalyst effect. However, H_4DOBDC, the linker of MOF-74, had the problem to insert the functional group in the framework.[17,18] The functional groups of H_4DOBDC has not been reported yet because of crucial organic synthesis and if the ligand was synthesized then the steric hindrance between functional groups and metal nodes in framework made the issue. For these reasons, the functional groups of linkers are reported in the IRMOF-74-III, where various residues are inserted into the central phenyl groups of linkers.[19,20]

Defect-engineered MOF (DEMOF) with mixed ligands of original and fragmented linker was used to produce the porosity (missing metal nodes and linker vacancies), catalytic metal sites (partial metal node reduction) and second functionalities.[21-25] Defect-engineered MOF-74 with fragmented linker was mostly reported with 2-hydroxy-1,4-benzene dicarboxylic acid (H_2BDC-OH) and one case of 1,4-benzenedicarboxylic acid (H_2BDC) with only 6% introduced.[26-28] Whereas, different fragmented linkers were difficult to introduce in MOF-74 even salicylic acid was used as modulator to fabricate nano-rod Zn-MOF-74.[29]

Herein, we introduce the fragmented linker (salicylic acid, SA) that has mono carboxylate and hydroxyl group into Ni-MOF-74 (**Figure 2.1**). SA are commercially available to obtain substances with various functional groups. In order to synthesis defect-engineered MOF-74 with SA, the proper synthesis condition, metal ions and solvent system was needed. SA-incorporated DEMOF-74 was successfully synthesized in proper solvent condition (DMF/EtOH/H_2O, 15:1:1, v/v/v) with nickel. In order to install a functional group into the DEMOF-74, the electronic effect and the functional group position play the important role. Up to 30-40% of fragmented linkers are available to be inserted in the framework and maintained the crystal structure as MOF-74. Depending on the position of functional group, affects the porosity, CO_2 and H_2 gas adsorption.

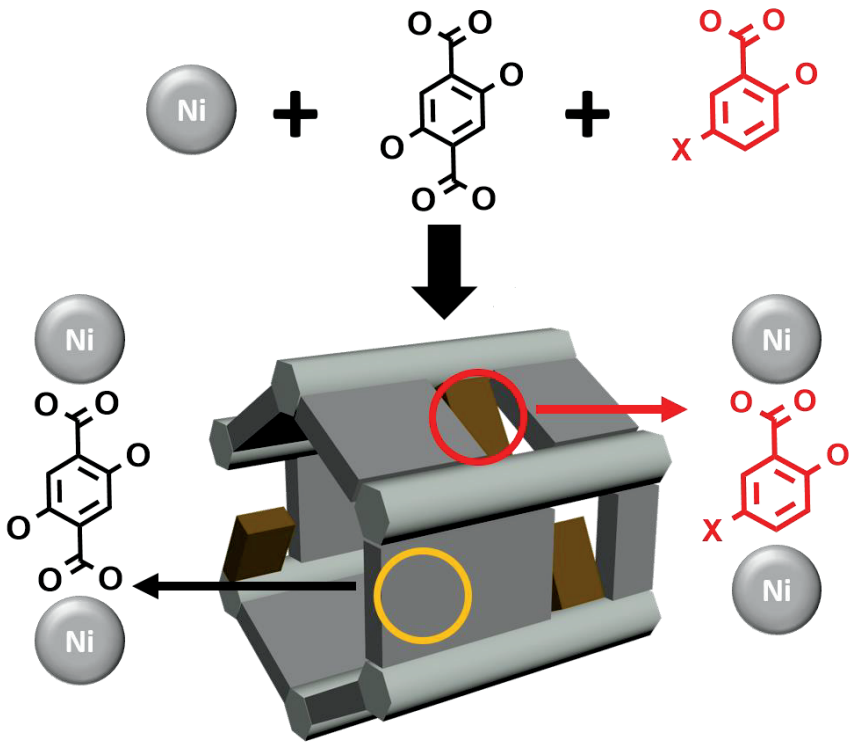

Figure 2.1. Scheme of defect-engineered MOF-74 with salicylic acid derivatives.

2.2 Experimental section

General procedure

All reagents were purchased from commercial sources and used without further purification. Powder X-ray diffraction (PXRD) data were recorded using a Bruker D2 Phaser automated diffractometer at room temperature, with a step size of $2\theta = 0.02°$. ^{1}H nuclear magnetic resonance (NMR) spectra were recorded using a Varian 400 MHz FT-NMR spectrometer at the UNIST Central Research Facilities. Fourier-transformation infrared spectroscopy (FT-IR) spectra were recorded using a NICOLET iS 10 FT-IR spectrometer (4000-650 cm^{-1}). Thermogravimetric analysis (TGA) was performed using a Q-600 series instrument from TA Instruments at a heating rate of 5 °C min^{-1} under flowing nitrogen gas. The sample was dried before the TGA measurement using flowing N_2 for 60 min. Scanning Electron Microscopy (SEM) was performed using SU-8220 from Hitachi High-Technologies. For the gas adsorption experiments, at least 40 mg of each sample exchanged with methanol was charged into a sample cell and heated at 150 °C under the vacuum for 24 hours. All of the gas sorption isotherms were measured using a BELSORP-max (BEL Japan, Inc.) low-pressure adsorption measuring system employing a standard volumetric technique up to saturation pressure. The N_2 (purity of 99.999%) sorption isotherms were monitored at 77 K. The adsorption data in the pressure range of < 0.1 P/P_0 were fitted to the Brunauer−Emmett−Teller (BET) equation to determine the BET surface area. CO_2 (purity of 99.999%) adsorption isotherms were measured at 273 and 298 K, respectively. H_2 (purity of 99.999 %) adsorption isotherms were measured at 77 K. All the adsorption data were manipulated by BEL-Master software provided by BEL Japan, Inc.

Preparation of MOFs

Synthesis of Ni-MOF-74 and defective derivatives

[Ni_2(DOBDC)(H_2O)$_2$](Ni-MOF-74). A solid mixture of $Ni(NO_3)_2 \cdot 6H_2O$ (198 mg, 0.680 mmol) and 2,5-dihydroxy-1,4-benzenedicarboxylic acid (H_4DOBDC) (95 mg, 0.48 mmol) was dissolved in 10 mL of a mixed solvent (15:1:1, *N,N*-dimethylformamide (DMF)/ethanol (EtOH)/H_2O, v/v/v) with a sonication. The solution was transferred to a 20 mL vial, tightly sealed, and heated at 100 °C for 24 hours. The precipitate was harvested and washed several times using DMF and methanol (MeOH) for several days. The activated Ni-MOF-74 sample was prepared by vacuum-drying the MeOH-exchanged sample overnight at 150 °C for 1 24 hours.

[Ni_2(DOBDC)$_{1-x}$(SA)$_x$(OH)$_{2x}$(H_2O)$_{2+x}$] (SA$_x$). A solid mixture of H_4DOBDC, salicylic acid (H_2SA) and $Ni(NO_3)_2 \cdot 6H_2O$ with different feed ratios (90:10, 70:30, 50:50, 30:70) was added to a 15:1:1 (v/v/v) mixture of DMF/ethanol/water (10 mL). The suspension was sonicated until it was homogeneous. Then, the mixture was heated in an oven at 100 °C for 24 hours. After cooling down to room temperature, the mother liquor was decanted and DMF was added and replenished three times. Finally, the DMF was replaced with methanol, which was refreshed several times over 3 days.

[Ni_2(DOBDC)$_{1-x}$(2-hNA)$_x$(OH)$_{2x}$(H_2O)$_{2+x}$](2-hNA$_x$). A solid mixture of H_4DOBDC, 2-hydroxynicotinic acid (H_2-2-hNA) with different feed ratios (90:10, 70:30, 50:50) and $Ni(NO_3)_2 \cdot 6H_2O$ was added to a 15:1:1 (v/v/v) mixture of DMF/ethanol/water (10 mL). The suspension was sonicated until it was homogeneous. Then, the mixture was heated in an oven at 100 °C for 24 hours. After cooling down to room temperature, the mother liquor was decanted and DMF was added and replenished three times. Finally, the DMF was replaced with methanol, which was refreshed several times over 3 days.

[Ni_2(DOBDC)$_{1-x}$(n-aSA)$_x$(OH)$_{2x}$(H_2O)$_{2+x}$](n-aSA$_x$). A solid mixture of H_4DOBDC, n-aminosalicylic acid (H_2n-aSA) (n= 3 or 5) with different feed ratios (90:10, 70:30, 50:50) and $Ni(NO_3)_2 \cdot 6H_2O$ was added to a 15:1:1 (v/v/v) mixture of DMF/ethanol/water (10 mL). The suspension was sonicated until it was homogeneous. Then, the mixture was heated in an oven at 100 °C for 24 hours. After cooling down to room temperature, the mother liquor was decanted and DMF was added and replenished three times. Finally, the DMF was replaced with methanol, which was refreshed several times over 3 days.

[Ni_2(DOBDC)$_{1-x}$(3-hSA)$_x$(OH)$_{2x}$(H_2O)$_{2+x}$](3-hSA$_x$). A solid mixture of H_4DOBDC, 3-hydroxysalicylic acid (H_2-3-hSA) with different feed ratios (90:10, 70:30, 50:50) and $Ni(NO_3)_2 \cdot 6H_2O$ was added to a 15:1:1 (v/v/v) mixture of DMF/ethanol/water (10 mL). The suspension was sonicated until it was homogeneous. Then, the mixture was heated in an oven at 100 °C for 24 hours. After cooling down to room temperature, the mother liquor was decanted and DMF was added and replenished three times. Finally, the DMF was replaced with methanol, which was refreshed several times over 3 days.

$[Ni_2(DOBDC)_{1-x}(5\text{-}fSA)_x(OH)_{2x}(H_2O)_{2+x}](5\text{-}fSA_x)$. A solid mixture of H_4DOBDC, 5-formylsalicylic acid (H_2-5-fSA) with different feed ratios (90:10, 70:30, 50:50) and $Ni(NO_3)_2{\cdot}6H_2O$ was added to a 15:1:1 (v/v/v) mixture of DMF/ethanol/water (10 mL). The suspension was sonicated until it was homogeneous. Then, the mixture was heated in an oven at 100 °C for 24 hours. After cooling down to room temperature, the mother liquor was decanted and DMF was added and replenished three times. Finally, the DMF was replaced with methanol, which was refreshed several times over 3 days.

Attempts to synthesize defect-engineered Ni-MOF-74 with salicylic acid by different synthesis solvent conditions

SA(7/3) in DMF/EtOH/H_2O (1:1:1, v/v).[2] A mixture of $Ni(NO_3)_2{\cdot}6H_2O$ (2.38 g, 8.2 mmol), H_4DOBDC (333 mg, 1.68 mmol), and H_2SA (100 mg, 0.72 mmol) were dissolved in 200 mL of a mixed solvent (1:1:1, DMF/EtOH/H_2O, v/v). The solution was transferred to a 500 mL vial, which was tightly sealed and heated at 100 °C for 1 d to form a crystalline powder precipitate.

I-SA(7/3) in H_2O.[8] A mixture of $Ni(CH_3COO)_2{\cdot}4H_2O$ (1.00 g, 4 mmol), H_4DOBDC (277 mg, 1.4 mmol), and H_2SA (82.9 mg, 0.6 mmol) were added in 15 mL of H_2O. The solution was refluxed with stirring for 1h and cooled to room temperature. The yellow powder was collected by centrifugation.

2.3 Results and discussions.

Attempts to synthesize isostructural defect-engineered M-MOF-74

All attempts to incorporate a salicylate (SA), as a fragmented ligand, into the framework of M-MOF-74 (M = Mg, Mn, Co, and Zn) were unsuccessful (**Figures 2.2** and **2.3**). While adopting the same procedure used in the **Ni-SA$_{0.09}$**, all attempts to synthesize isostructural defect-engineered **M-SA$_X$** using other metal sources, such as $Mg(NO_3)_2{\cdot}6H_2O$, $Mn(NO_3)_2{\cdot}6H_2O$, $Co(NO_3)_2{\cdot}6H_2O$, and $Zn(NO_3)_2{\cdot}6H_2O$, instead of $Ni(NO_3)_2{\cdot}6H_2O$ were unsuccessful.

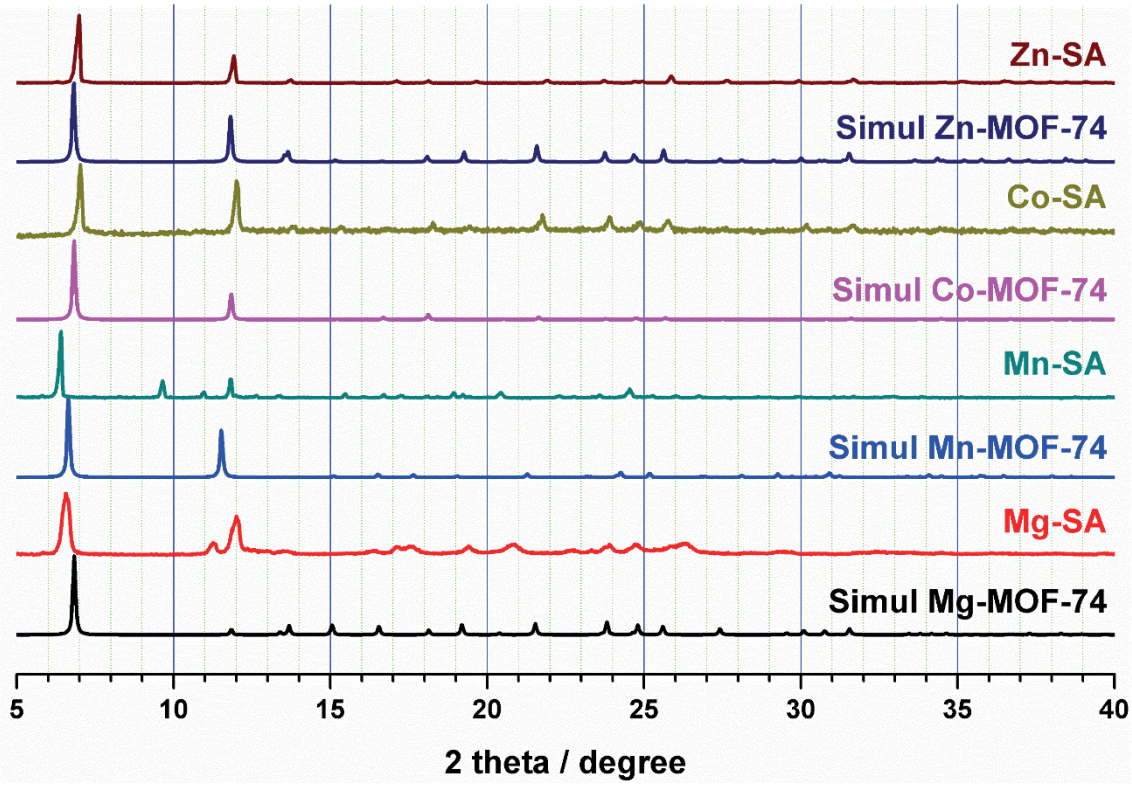

Figure 2.2. PXRD patterns of defect-engineered M-MOF-74 series. **Mg-SA** and **Mn-SA** produced unidentified crystalline phases.

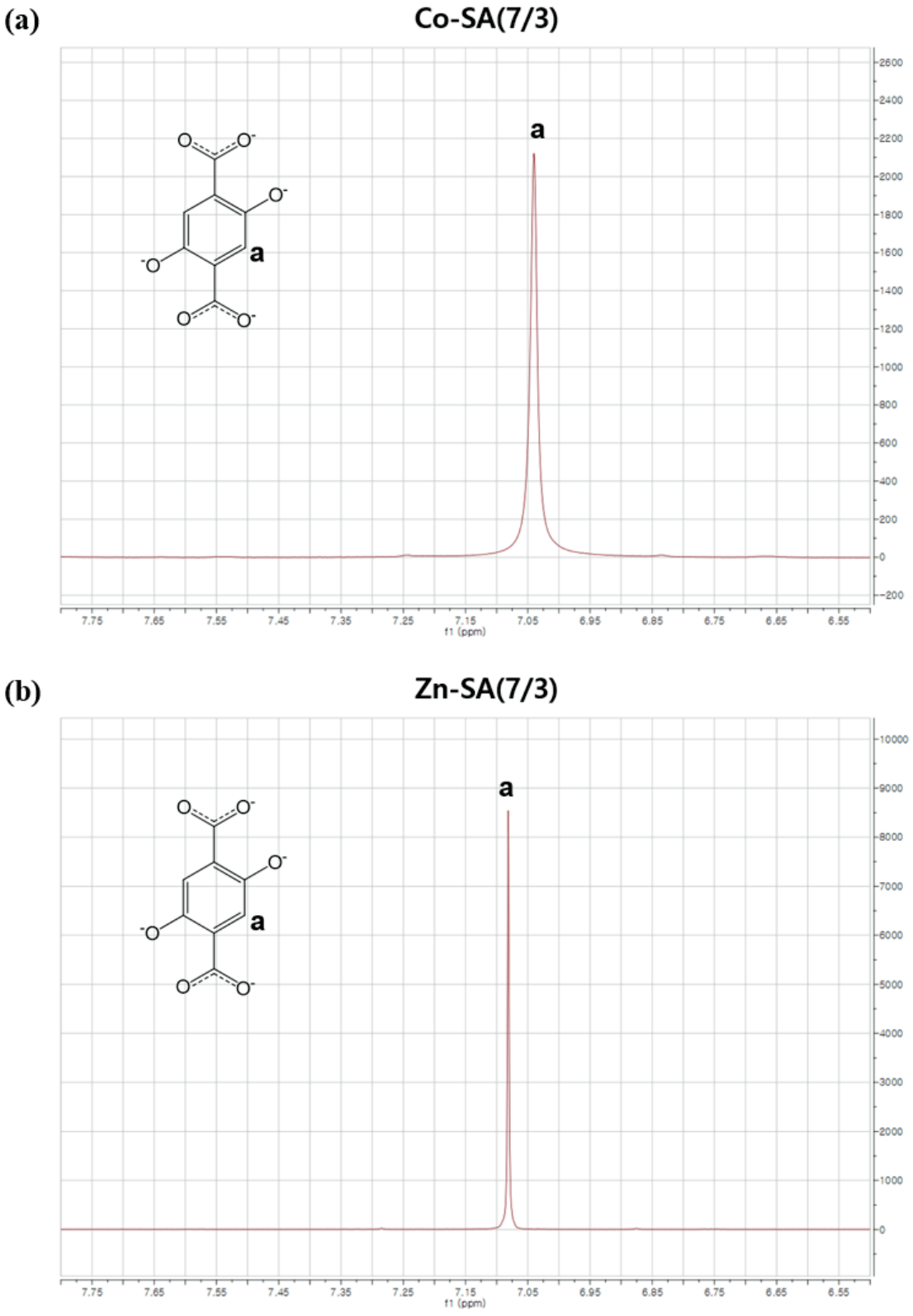

Figure 2.3. ^{1}H NMR spectrum of (a) **Co-SA(7/3)** and (b) **Zn-SA(7/3),** where 7/3 is the molar ratio of H_4DOBDC and H_2SA used for the preparation of the MOFs. Both of them do not contain any SA in the framework.

Attempts to synthesize defect-engineered Ni-MOF-74 with salicylic acid by different synthesis solvent conditions

Contrarily, for Ni-MOF-74, the SA-incorporated DEMOF (**SA_x**, where x represents Ni-MOF-74 and the mole fraction of the integrated SA at the DOBDC ligand sites of the framework) was successfully synthesized in a DMF/EtOH/H_2O (15:1:1, v/v/v) solvent mixture (**Figures 2.4** and **2.5**).

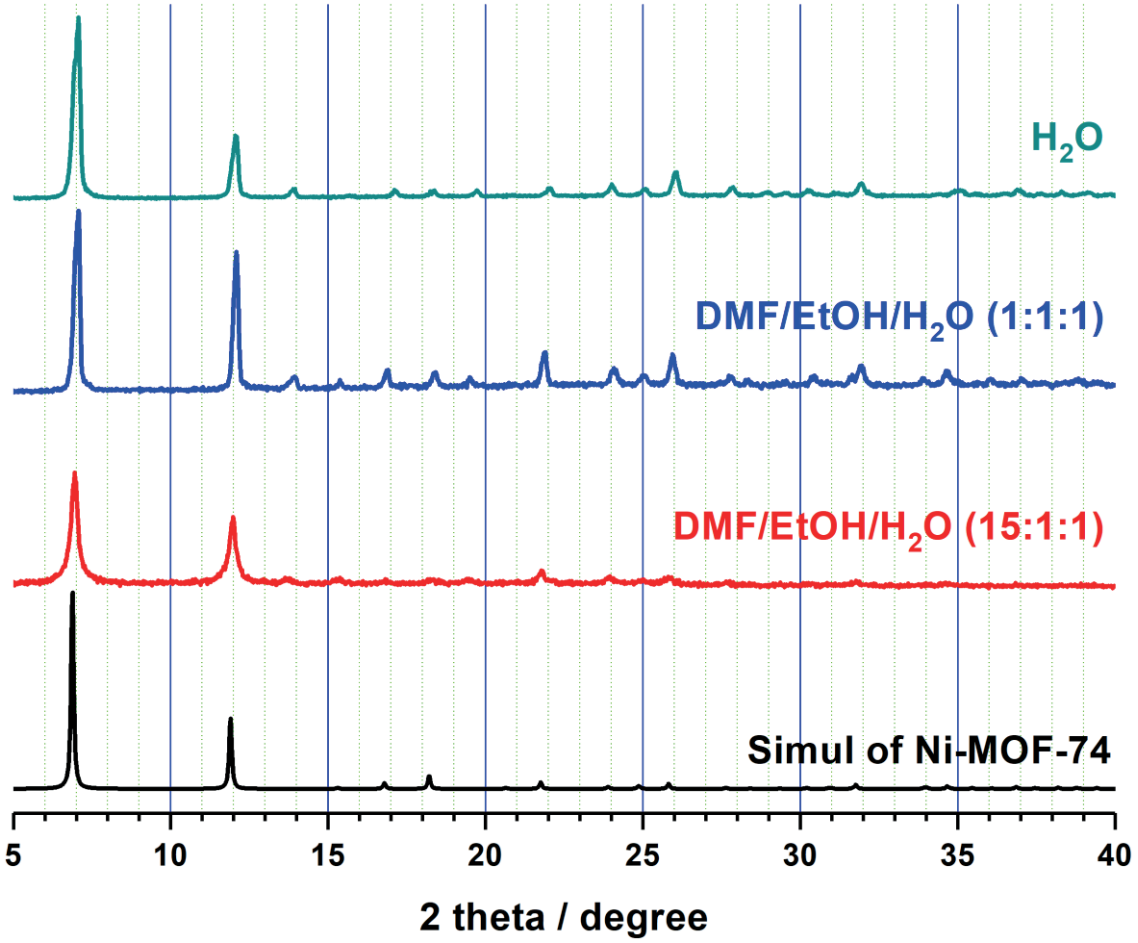

Figure 2.4. PXRD patterns of **Ni-SA(7/3)** obtained in various synthesis conditions.

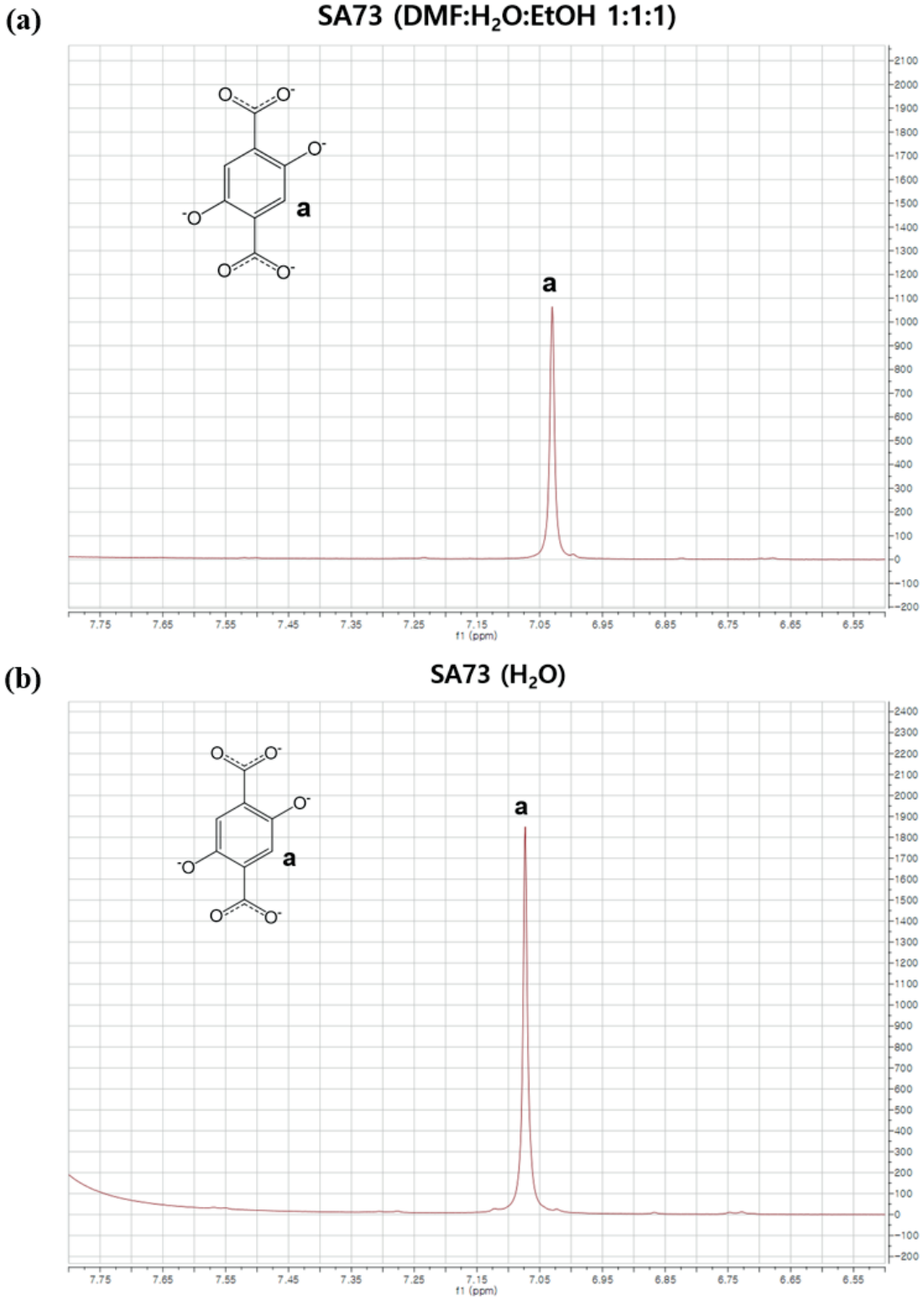

Figure 2.5. ^{1}H NMR spectrum of **Ni-SA(7/3)** obtained in (a) DMF/EtOH/H_2O (1:1:1, v/v) and (b) H_2O.

SA-incorporated Defect-engineered MOF-74

To investigate the doping level of salicylate (SA^{2-}) in the Ni-MOF-74 framework with respect to the initial feed ratios, defect-engineered Ni-MOF-74 derivatives were synthesized by mixing the original linker H_4DOBDC with different molar ratios (from 10 to 70%) of H_2SA via the direct solvothermal synthesis. All the SA-incorporated defect-engineered Ni-MOF-74 derivatives (named $\mathbf{SA_x}$, where **x** represent the mole fraction of the integrated SA^{2-} at the $DOBDC^{4-}$ linker sites of the framework) retained crystallinity and are isostructural to the defect-free Ni-MOF-74 as revealed in the PXRD analysis (**Figure 2.6**). As the molar ratios of H_2SA in the synthesis media increased, the diffraction peaks of $\mathbf{SA_x}$ became broad and their intensities decreased, indicating the poor crystallinity at the higher concentrations of SA^{2-}. An analysis of ^{1}H NMR spectra of $\mathbf{SA_x}$ samples digested in an acidic media revealed that 3~37% of $DOBDC^{4-}$ sites in the framework can be replaced by SA^{2-} when 90:10 (H_4DOBDC:H_2SA) and 30:70 (H_4DOBDC:H_2SA) feed ratios were used for the synthesis of $\mathbf{SA_x}$ derivatives (**Figures 2.7** and **2.8** and **Table 2.1**). On the basis of the PXRD patterns and the ^{1}H NMR spectroscopy results, it can be concluded that the Ni-MOF-74 framework is tolerant of incorporation of SA^{2-} up to ca. 35%.

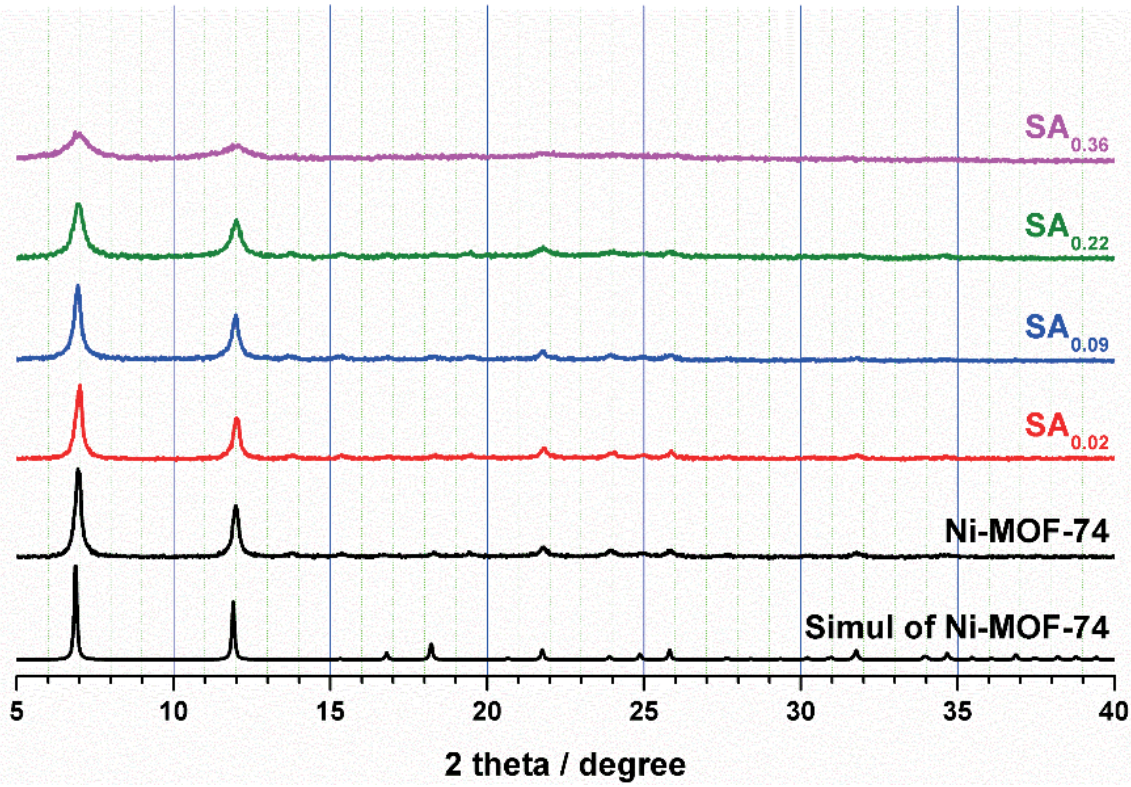

Figure 2.6. PXRD patterns of Ni-MOF-74 and $\mathbf{SA_x}$.

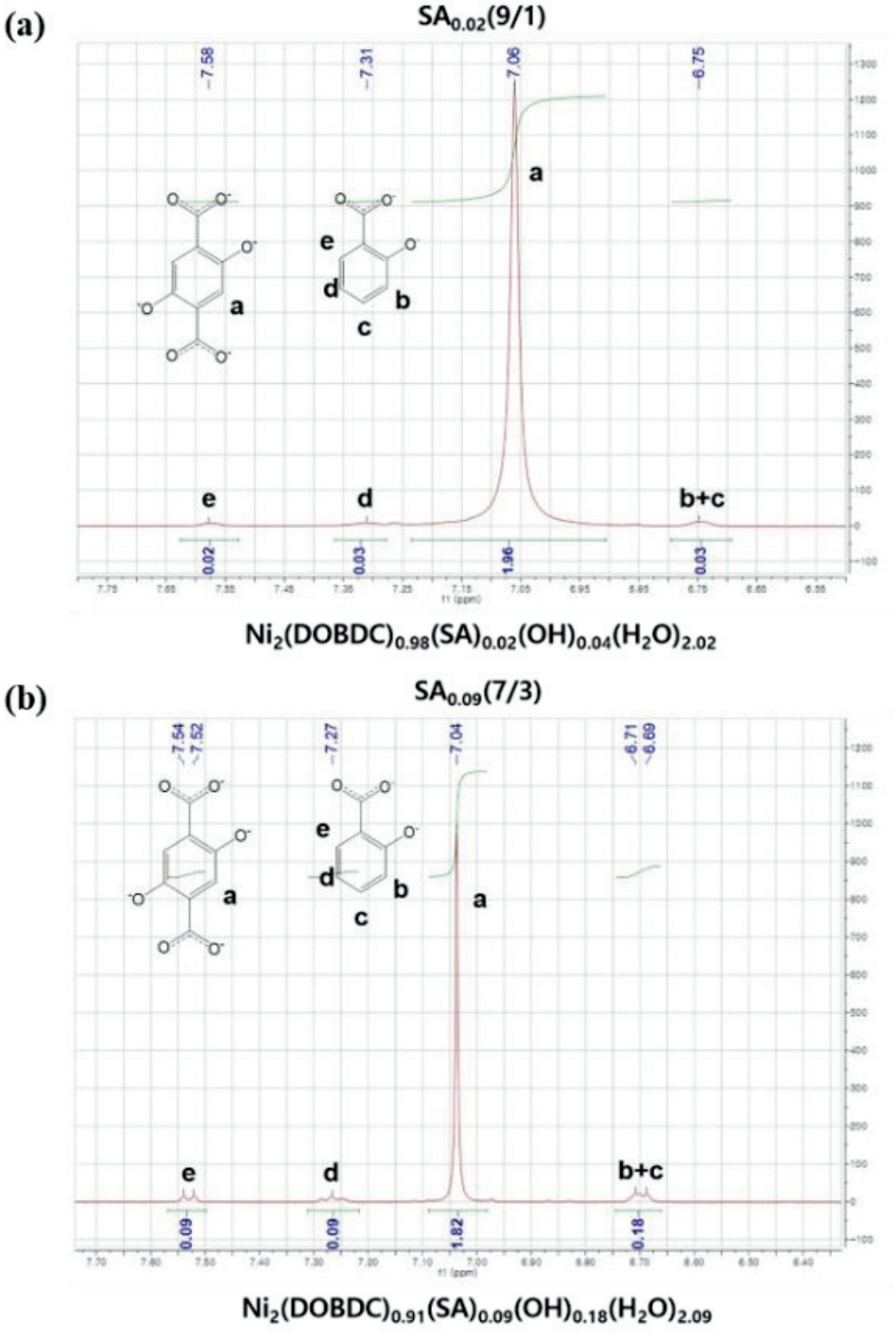

Figure 2.7. ^{1}H NMR spectrum of (a) **$SA_{0.02}$(9/1)** and (b) **$SA_{0.09}$(7/3)**. In **SA_x(a/b)**, x is the observed molar fraction of SA ligand in the framework from ^{1}H NMR spectrum, and a/b is the molar ratio of H_4DOBDC and H_2SA used for the preparation of the MOFs.

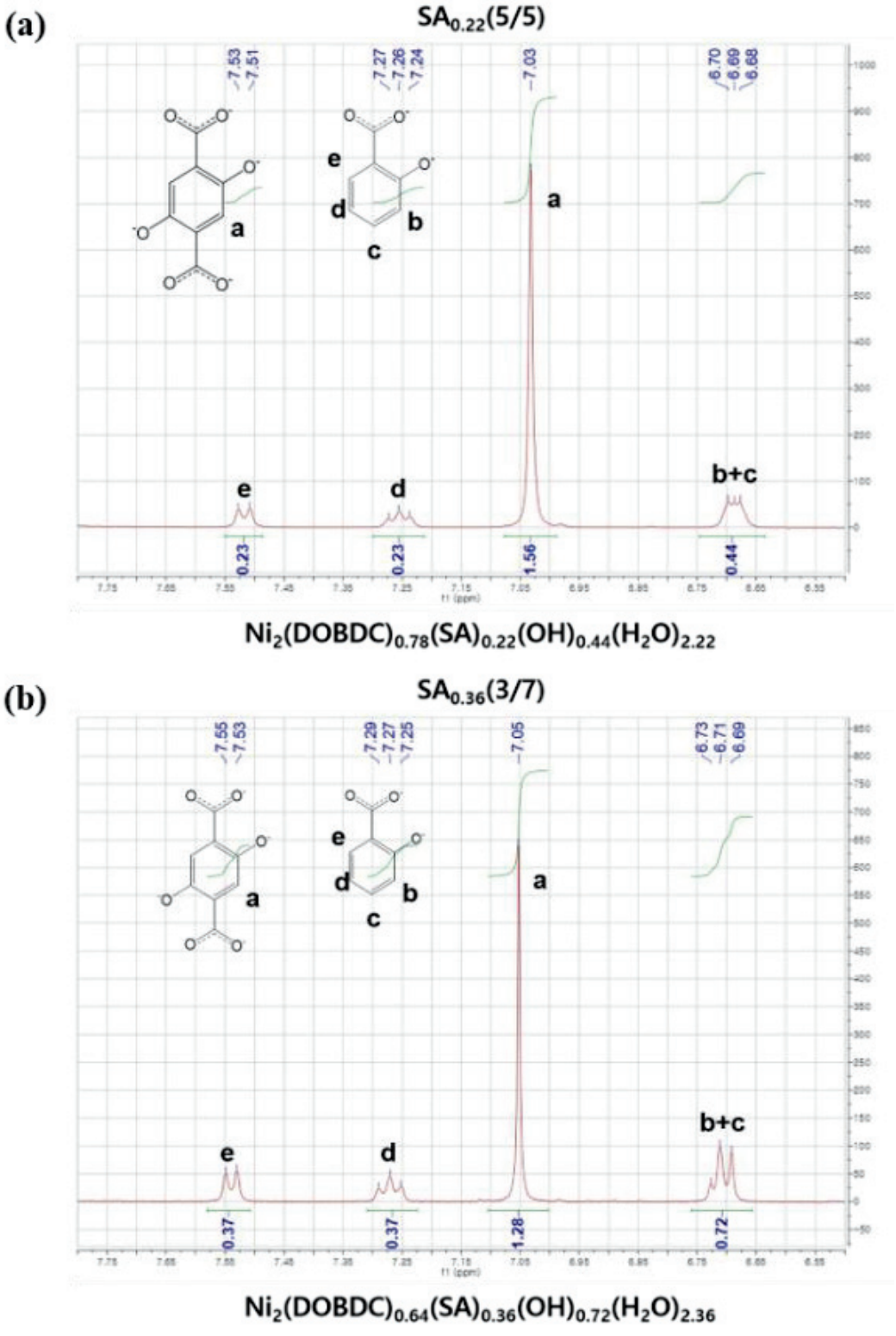

Figure 2.8. [1]H NMR spectrum of (a) **$SA_{0.22}$(5/5)** and (b) **$SA_{0.36}$(3/7)**.

Similarly, an attempt to incorporate an N-containing aromatic monocarboxylic acid into Ni-MOF-74 was made using the same synthetic protocol. 2-hydroxynicotinic acid (H_2-2-hNA) was chosen as the N-containing fragmented linker, where -COOH and -OH groups are positioned in the same way as in H_2SA. Defect-engineered Ni-MOF-74 derivatives were synthesized by mixing the H_4DOBDC with different molar ratios (from 10 to 50%) of H_2-2-hNA via the direct solvothermal synthesis. All the 2-hNA-incorporated defect-engineered Ni-MOF-74 derivatives (named **2-hNA$_x$**, where **x** represents the mole fraction of the integrated 2-hNA^{2-} at the DOBDC^{4-} linker sites of the framework) maintained crystallinity and are also isostructural to the defect-free Ni-MOF-74 as revealed in the PXRD analysis (**Figure 2.9**). Interestingly, the ^{1}H NMR analysis of digested **2-hNA$_x$** samples revealed that the incorporation of 2-hNA^{2-} is more efficient than that of SA^{2-} into **SA$_x$**, where the incorporated amount of 2-hNA^{2-} is approximately twice as large as that of SA^{2-} at the same feed ratios (**Figure 2.10** and **Table 2.1**). The fragmented linker 2-hNA^{2-} can replace the DOBDC^{4-} linker sites in the Ni-MOF-74 framework up to 29% when a 50:50 feed ratio of H_4DOBDC:H_2-2-hNA was used.

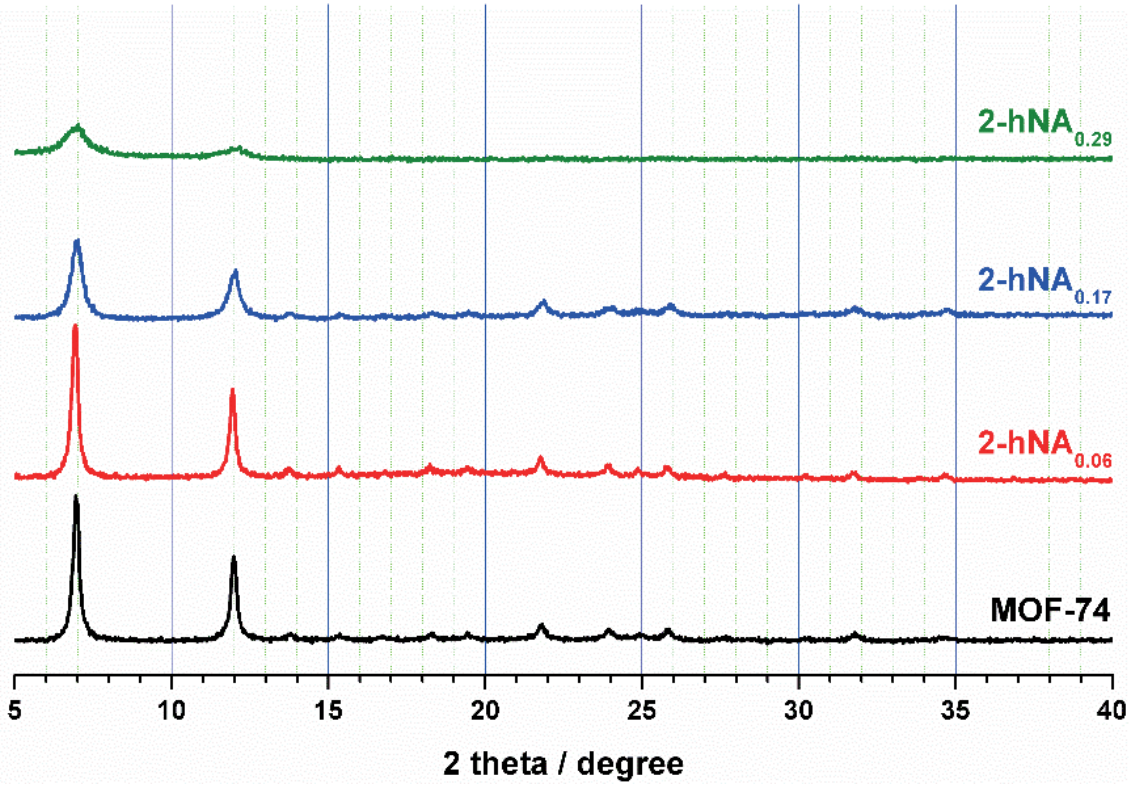

Figure 2.9. PXRD patterns of MOF-74 and **2-hNA$_x$**.

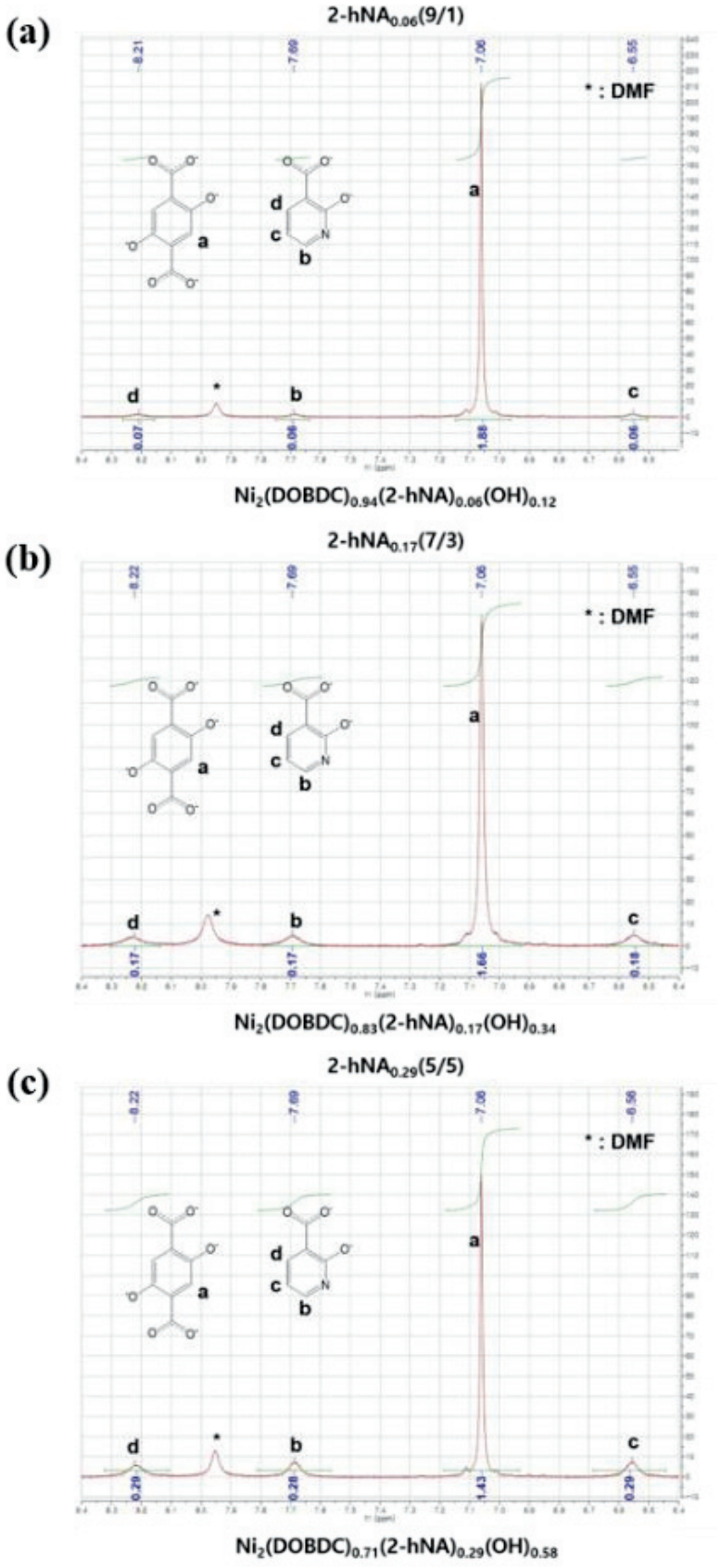

Figure 2.10. ^{1}H NMR spectrum of (a) **2-hNA$_{0.06}$(9/1)**, (b) **2-hNA$_{0.17}$(7/3)**, and (c) **2-hNA$_{0.29}$(5/5).**

The successful incorporation of H_2SA and H_2-2-hNA into the Ni-MOF-74 without disturbing the framework structure prompted the testing of other salicylic acid derivatives with useful functional groups. It was found that this fragmented linker installation approach is also effective for introducing various functionalized fragmented linkers (such as amine, formyl and hydroxyl groups) into the framework of Ni-MOF-74. Functionalized salicylic acid derivatives, 3-aminosalicylic acid (H_2-3-aSA), 5-aminosalicylic acid (H_2-5-aSA), 5-formylsalicylic acid (H_2-5-fSA) and 3-hydroxysalicylic acid (H_2-3-hSA) were incorporated into the framework of Ni-MOF-74 using the same reaction condition used for H_2SA and H_2-2-hNA installation. The PXRD patterns for all the resulting defect-engineered Ni-MOF-74 derivatives (denoted as **3-aSA$_x$**, **5-aSA$_x$**, **5-fSA$_x$** and **3-hSA$_x$**) with functional groups showed that all those MOFs are isostructural to the defect-free Ni-MOF-74 (**Figures 2.11** and **2.12**). As the mole fraction (or molar ratio) of the fragmented linkers increased, all the resulting defect-engineered Ni-MOF-74 exhibited poorer crystallinity. From the analysis of ^{1}H NMR spectra, the installed amounts of fragmented linkers within the framework of defect-engineered Ni-MOF-74 derivatives were found to range from ca. 10% to ca. 40% depending on the mole fraction of fragmented linkers in the synthetic media (**Figures 2.13-2.16** and **Table 2.1**). Again, it is found that the incorporation of functionalized SA^{2-} linkers is more efficient than that of SA^{2-} into **SA$_x$**. From the changes in PXRD patterns and ^{1}H NMR results, it can be concluded that the functionalized fragmented linkers can be incorporated in the Ni-MOF-74 framework with retaining good crystallinity up to ca. 20% mole fraction of the functionalized fragmented linkers. Interestingly, **5-aSA$_x$** and **5-fSA$_x$** exhibited better crystallinity at almost the same doping levels of the fragmented linkers compared to those of **3-aSA$_x$** and **3-hSA$_x$**, indicating that additional factors stabilizing the framework of defect-engineered MOFs might exist in **5-aSA$_x$** and **5-fSA$_x$**. Whereas, 4 and 6 position of functionalized salicylic acid derivatives, **4-aSA$_x$**, **4-hSA$_x$,** and **6-hSA$_x$**, were not installed into the framework because the steric hindrance between metal nodes and functional group (**Figures 2.17** and **2.18**).

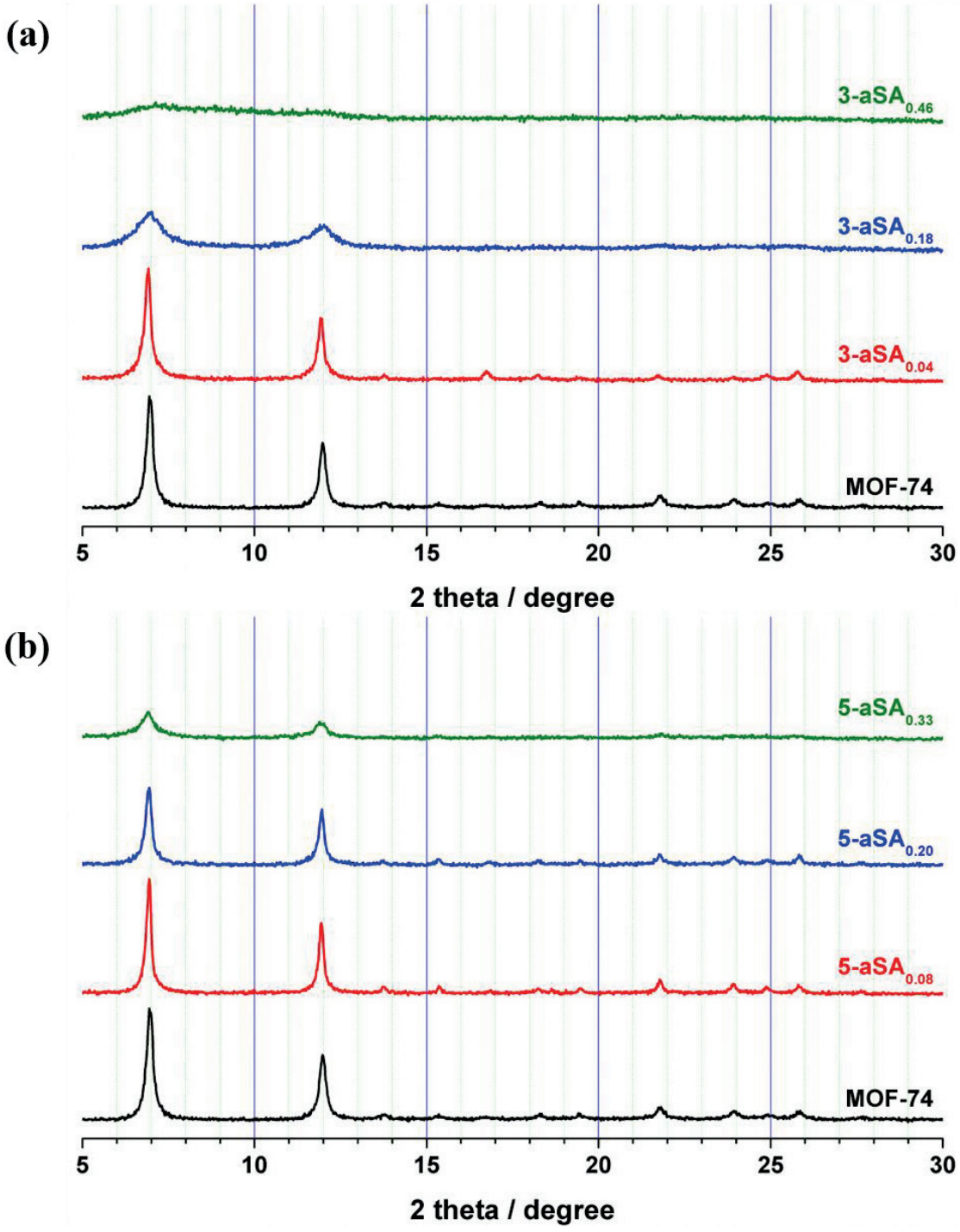

Figure 2.11. PXRD patterns of (a) **3-aSA$_x$** and (b) **5-aSA$_x$**.

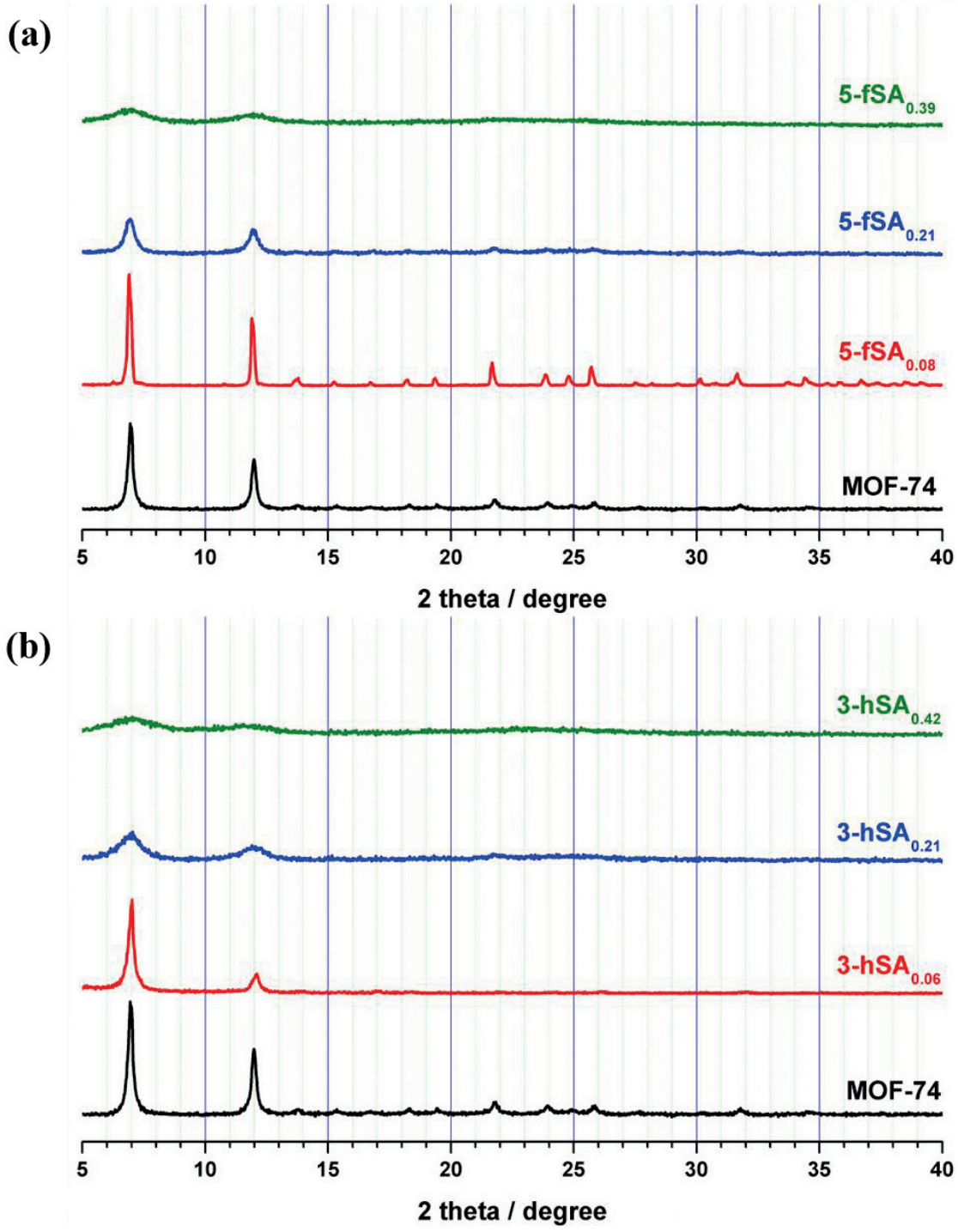

Figure 2.12. PXRD patterns of (a) **5-fSA$_x$** and (b) **3-hSA$_x$**.

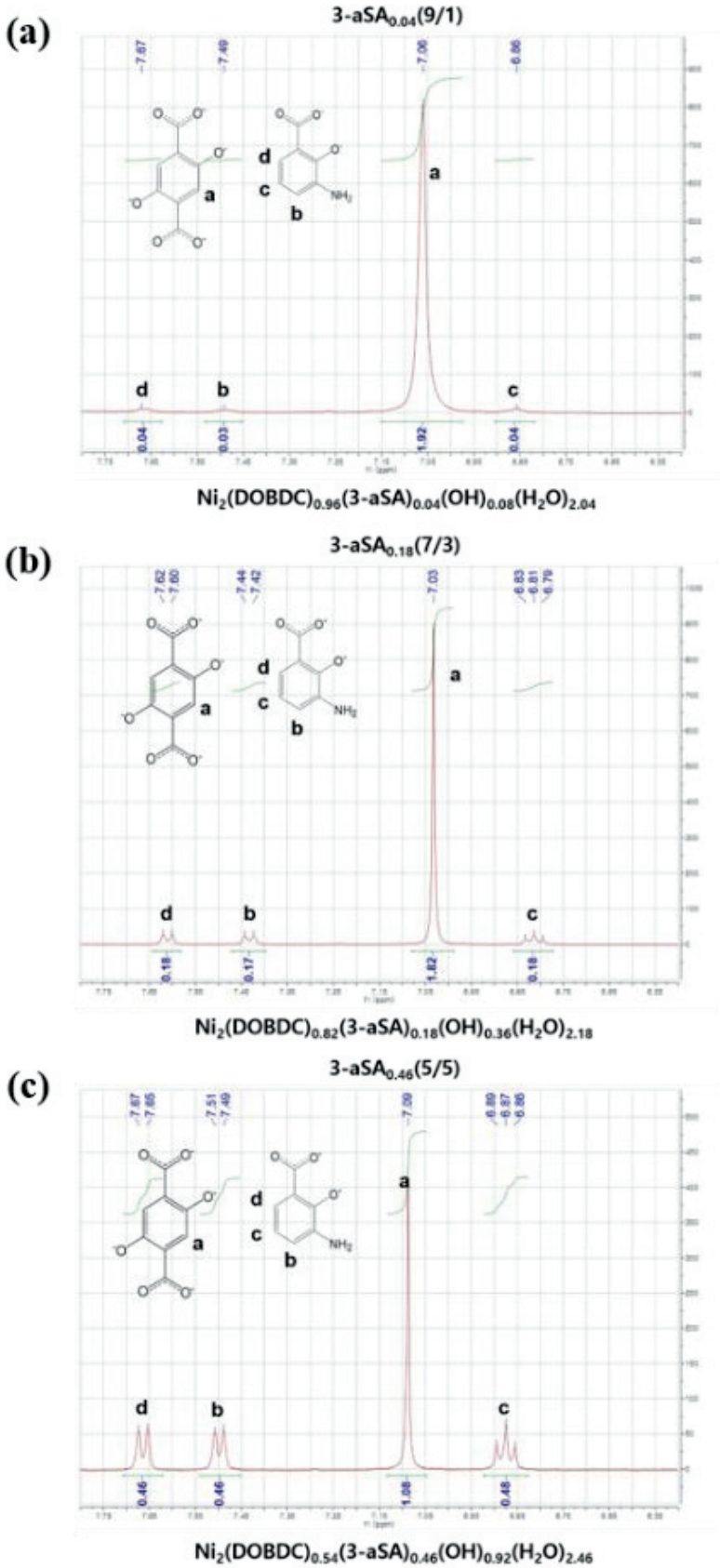

Figure 2.13. [1]H NMR spectrum of (a) **3-aSA$_{0.04}$(9/1)**, (b) **3-aSA$_{0.18}$(7/3)**, and (c) **3-aSA$_{0.46}$(5/5).**

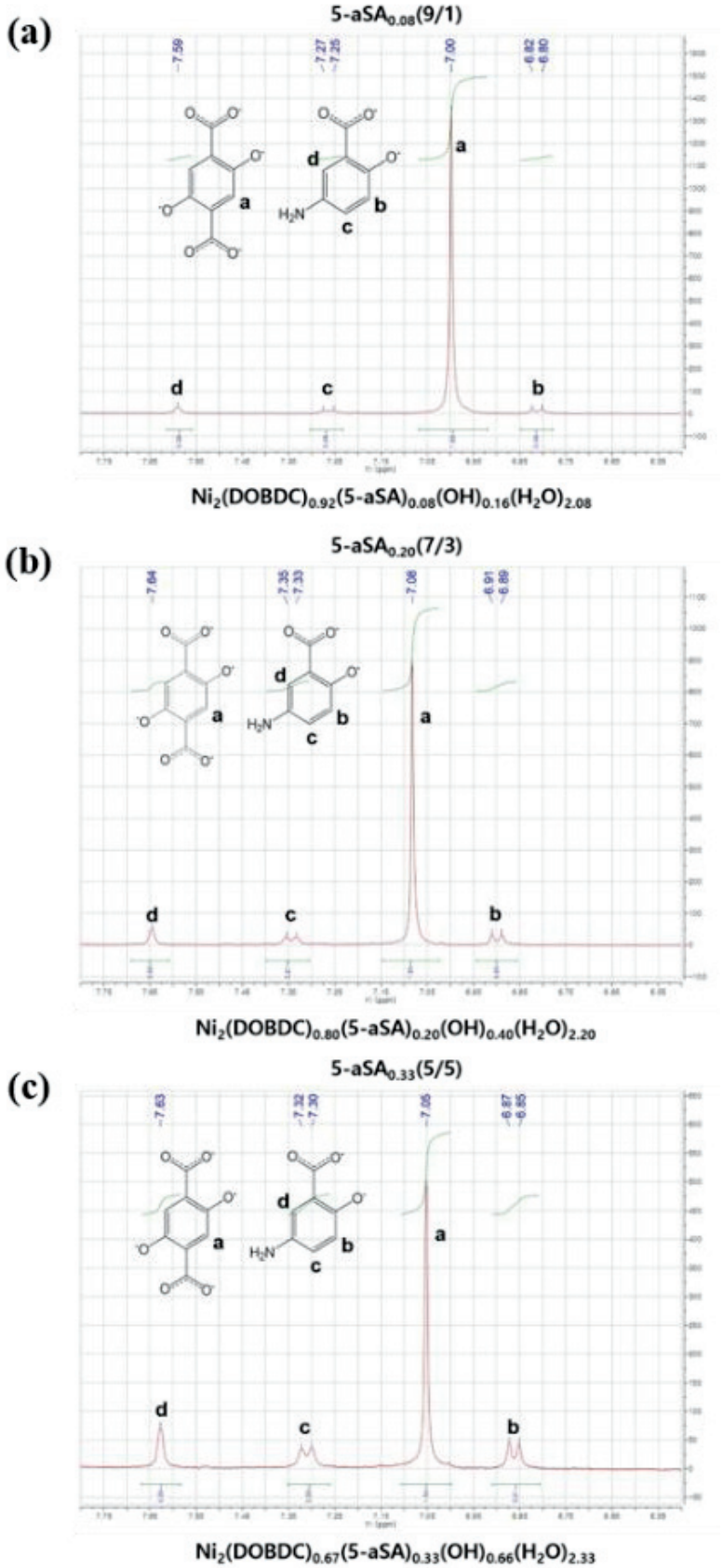

Figure 2.14. [1]H NMR spectrum of (a) **5-aSA$_{0.08}$(9/1)**, (b) **5-aSA$_{0.20}$(7/3)**, and (c) **5-aSA$_{0.33}$(5/5).**

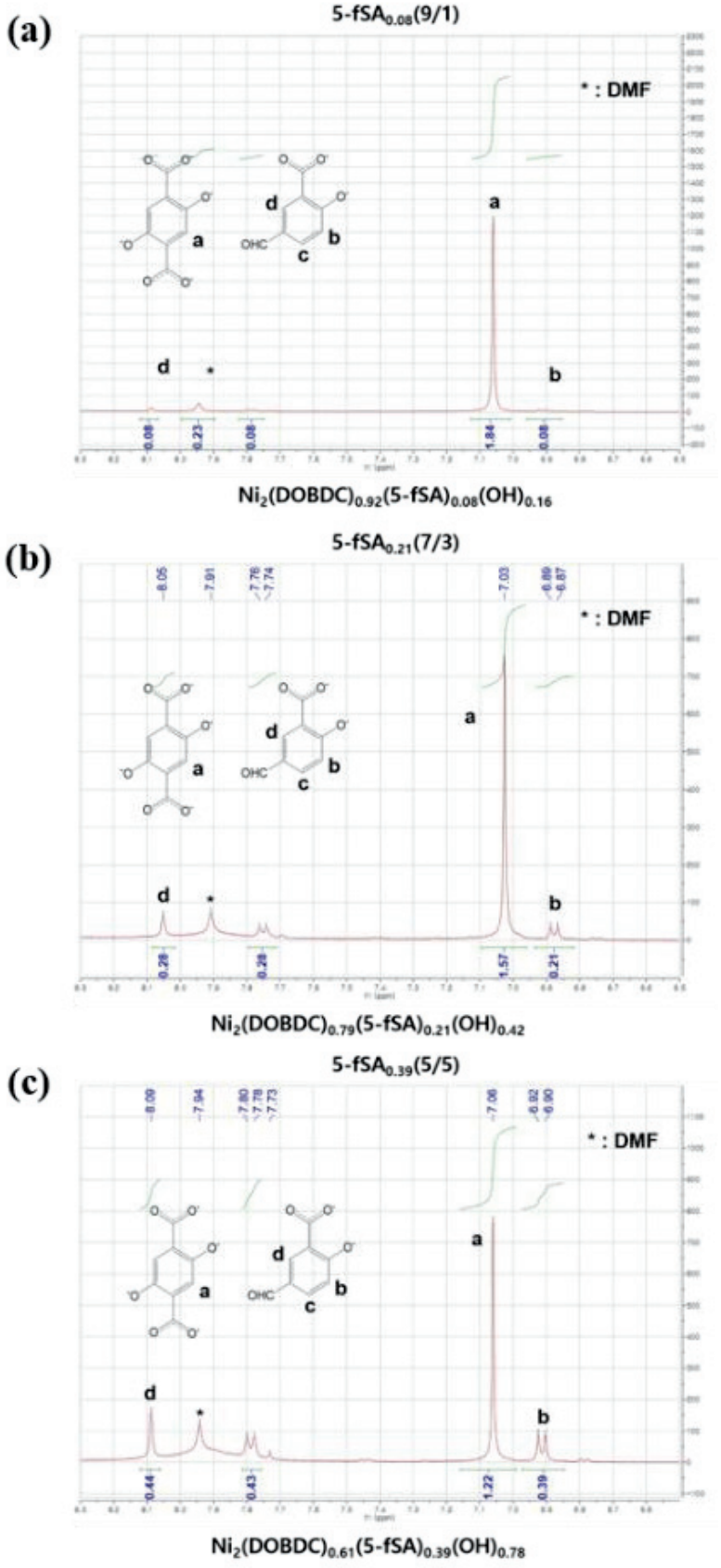

Figure 2.15. [1]H NMR spectrum of (a) **5-fSA$_{0.08}$(9/1)**, (b) **5-fSA$_{0.21}$(7/3)**, and (c) **5-fSA$_{0.39}$(5/5).**

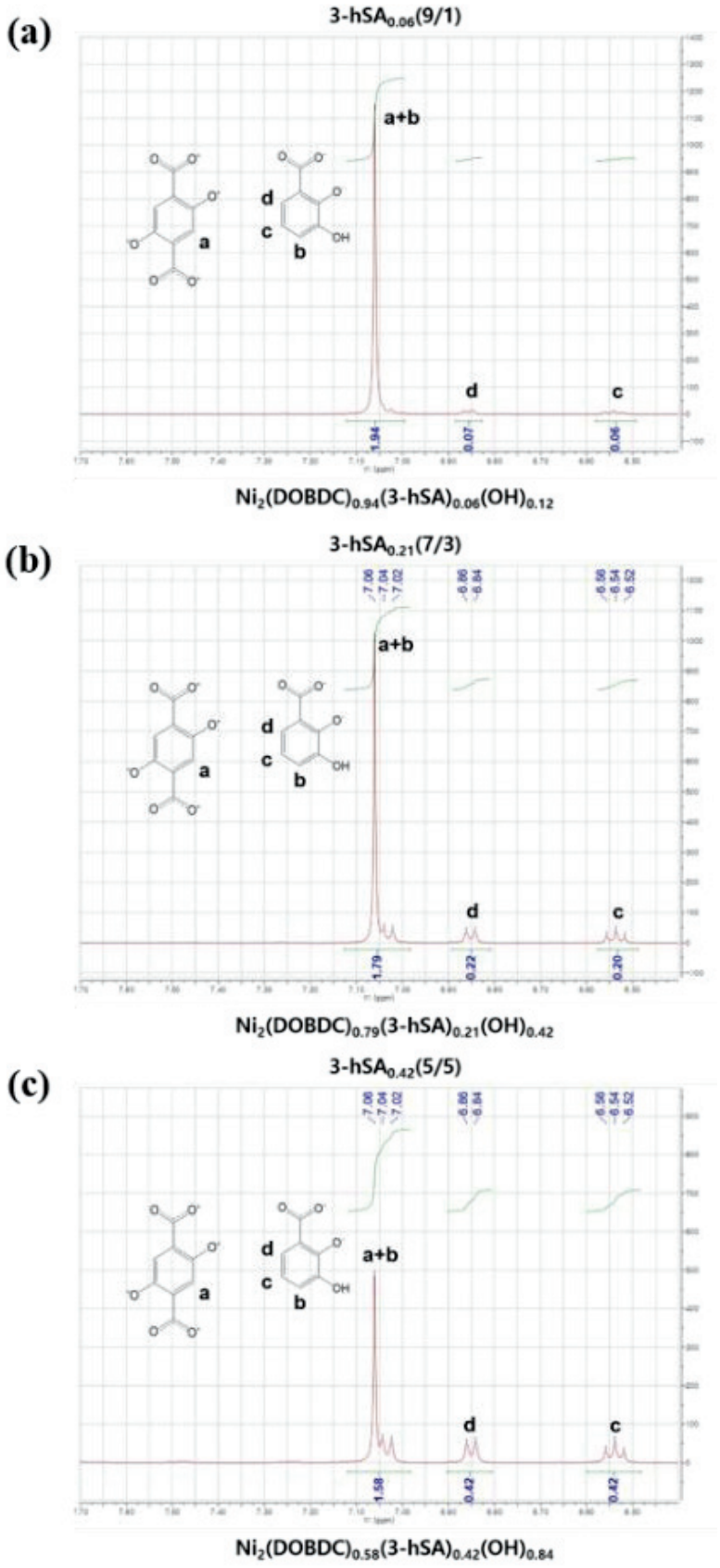

Figure 2.16. ^{1}H NMR spectrum of (a) **3-hSA$_{0.06}$(9/1)**, (b) **3-hSA$_{0.17}$(7/3)**, and (c) **3-hSA$_{0.42}$(5/5).**

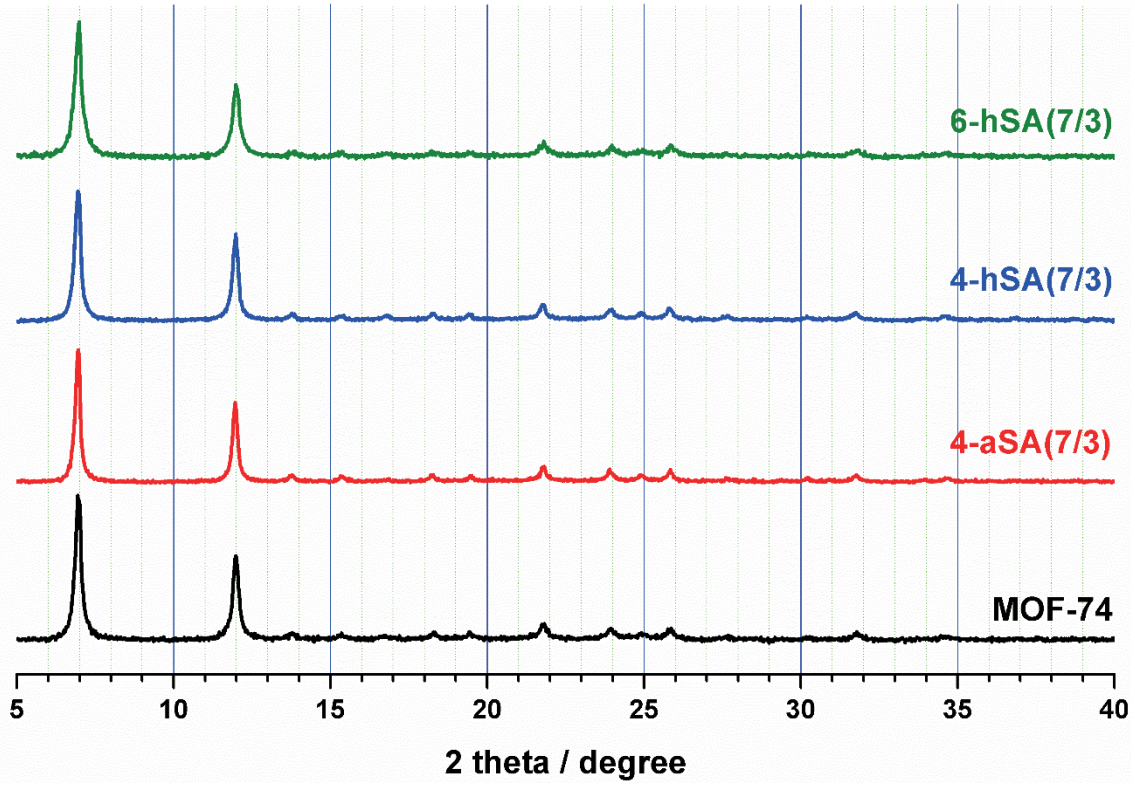

Figure 2.17. PXRD patterns of not incorporated fragmented linkers, **4-aSA(7/3)**, **4-hSA(7/3)** and **6-hSA(7/3)**.

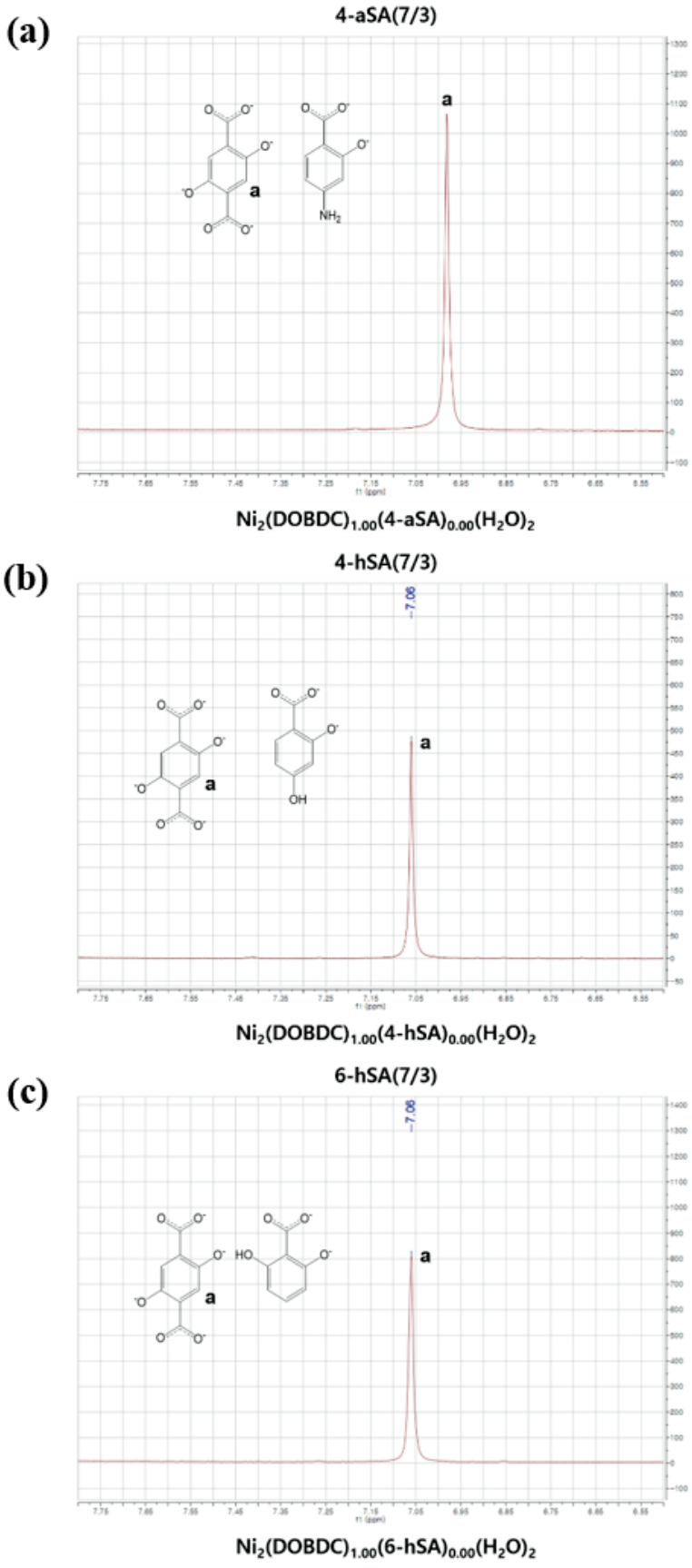

Figure 2.18. [1]H NMR spectrum of (a) **4-aSA(7/3)**, (b) **4-hSA(7/3)**, and (c) **6-hSA(7/3).**

Table 2.1. The doping ratios of the amount of defective linkers of defect-engineered MOF-74.

Sample Name	Dopling Linkers	Feeding ratios / %	Obtained ratios / %
SA$_{0.02}$	H_2-SA	10	2
SA$_{0.09}$	H_2-SA	30	9
SA$_{0.22}$	H_2-SA	50	22
SA$_{0.36}$	H_2-SA	70	36
2-hNA$_{0.06}$	H_2-2-hNA	10	6
2-hNA$_{0.17}$	H_2-2-hNA	30	17
2-hNA$_{0.29}$	H_2-2-hNA	50	29
3-aSA$_{0.04}$	H_2-3-aSA	10	4
3-aSA$_{0.18}$	H_2-3-aSA	30	18
3-aSA$_{0.46}$	H_2-3-aSA	50	46
5-aSA$_{0.08}$	H_2-5-aSA	10	8
5-aSA$_{0.20}$	H_2-5-aSA	30	20
5-aSA$_{0.33}$	H_2-5-aSA	50	33
5-fSA$_{0.08}$	H_2-5-fSA	10	8
5-fSA$_{0.21}$	H_2-5-fSA	30	21
5-fSA$_{0.39}$	H_2-5-fSA	50	39
3-hSA$_{0.06}$	H_2-3-hSA	10	6
3-hSA$_{0.21}$	H_2-3-hSA	30	21
3-hSA$_{0.42}$	H_2-3-hSA	50	42

Morphology of DEMOF-74

In this synthetic condition, DEMOF-74 was formed in rod shapes (MOF-74, **SA_x**, **2-hNA_x**, **5-aSA_x**, **5-fSAx** and **3-hSA_x**) or spherical particles (**3-aSA_x**) in nanometer dimensions (**Figures 2.19-2.24**).

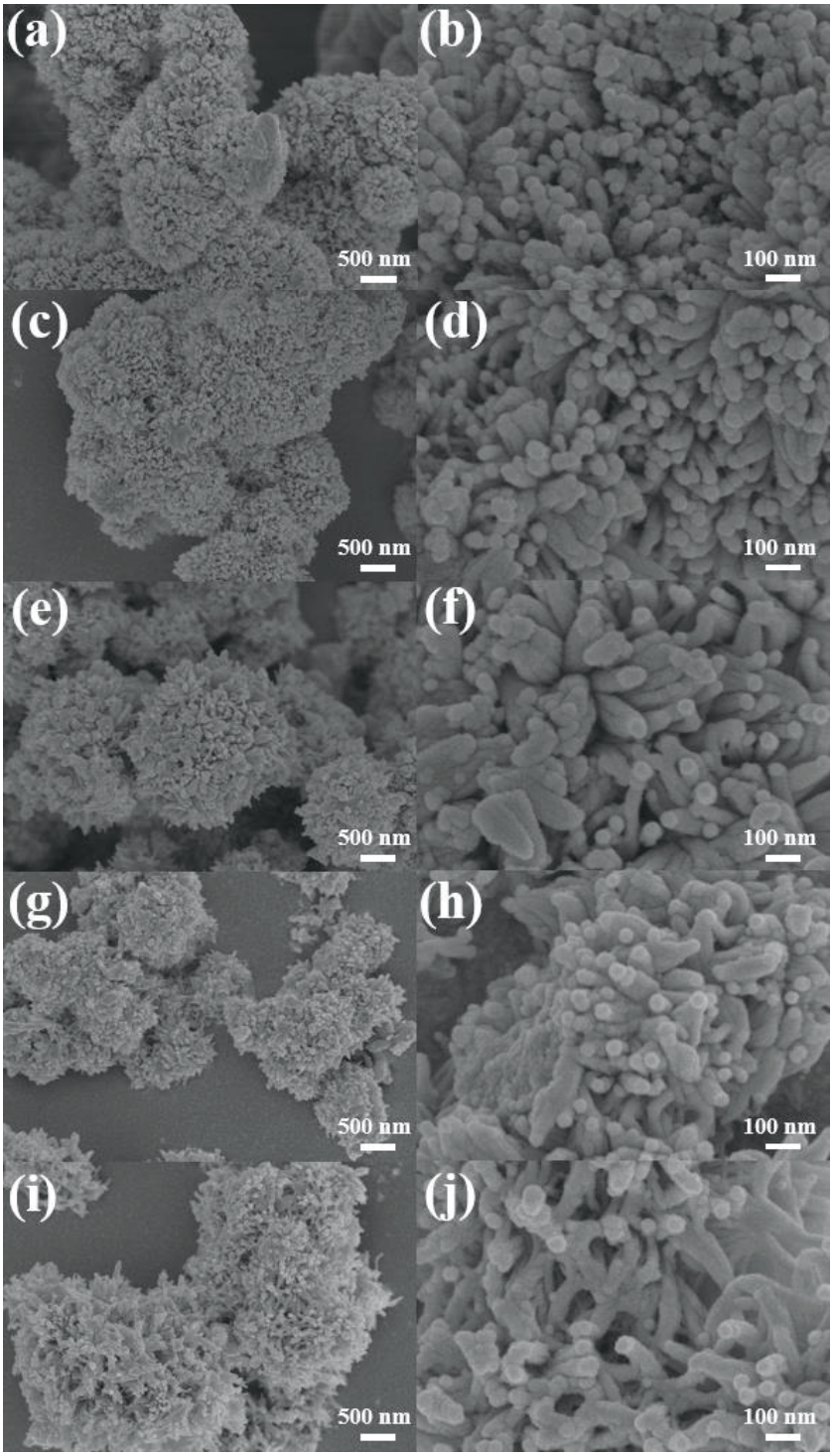

Figure 2.19. SEM images of Ni-MOF-74 and **SA_x**. (a, b) Ni-MOF-74, (c, d) **$SA_{0.02}$**, (e, f) **$SA_{0.09}$**, (g, h) **$SA_{0.22}$**, and (i, j) **$SA_{0.36}$**.

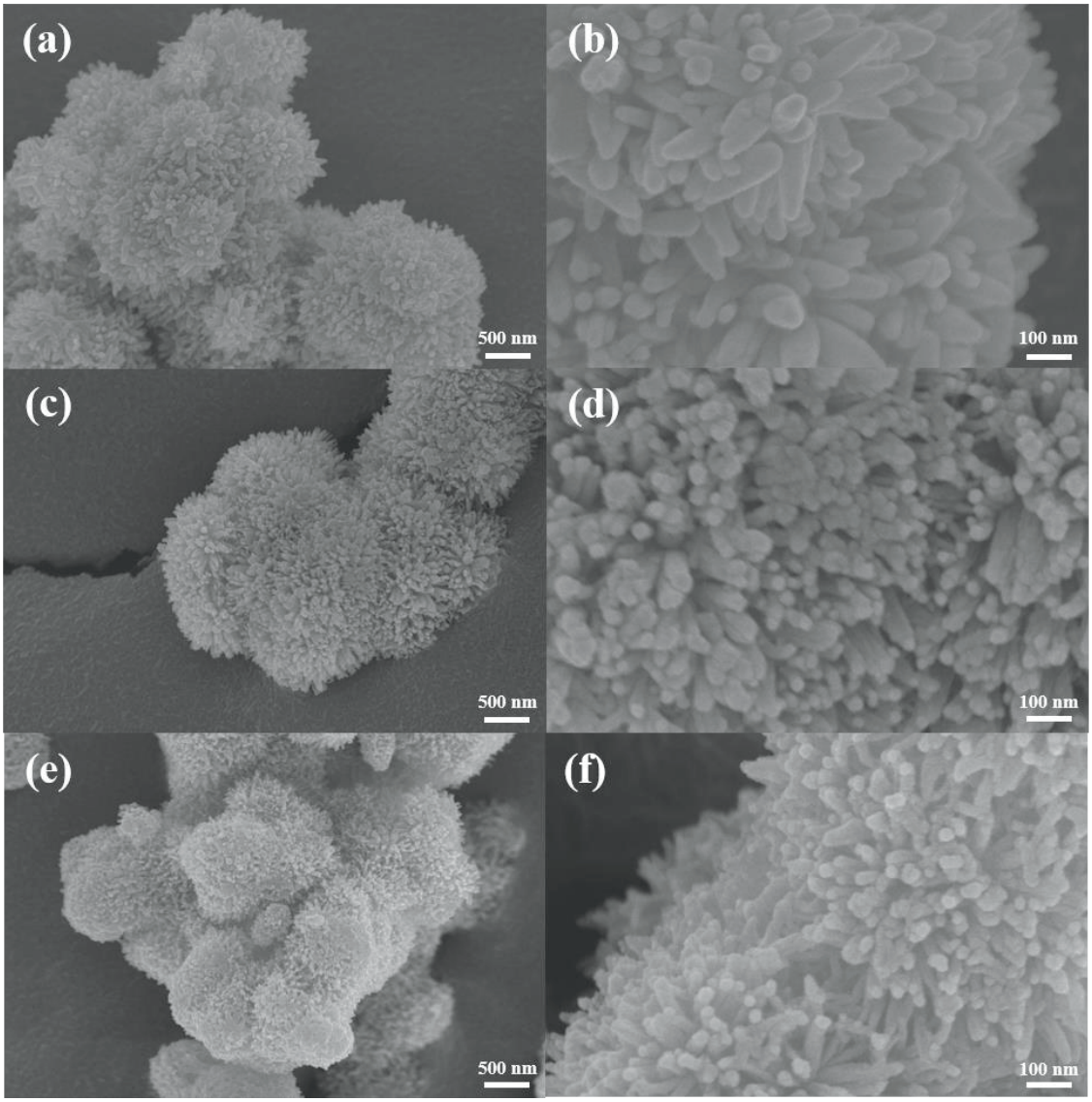

Figure 2.20. SEM images of **2-hNA$_x$**. (a, b) **2-hNA$_{0.06}$**, (c, d) **2-hNA$_{0.17}$**, and (e, f) **2-hNA$_{0.29}$**.

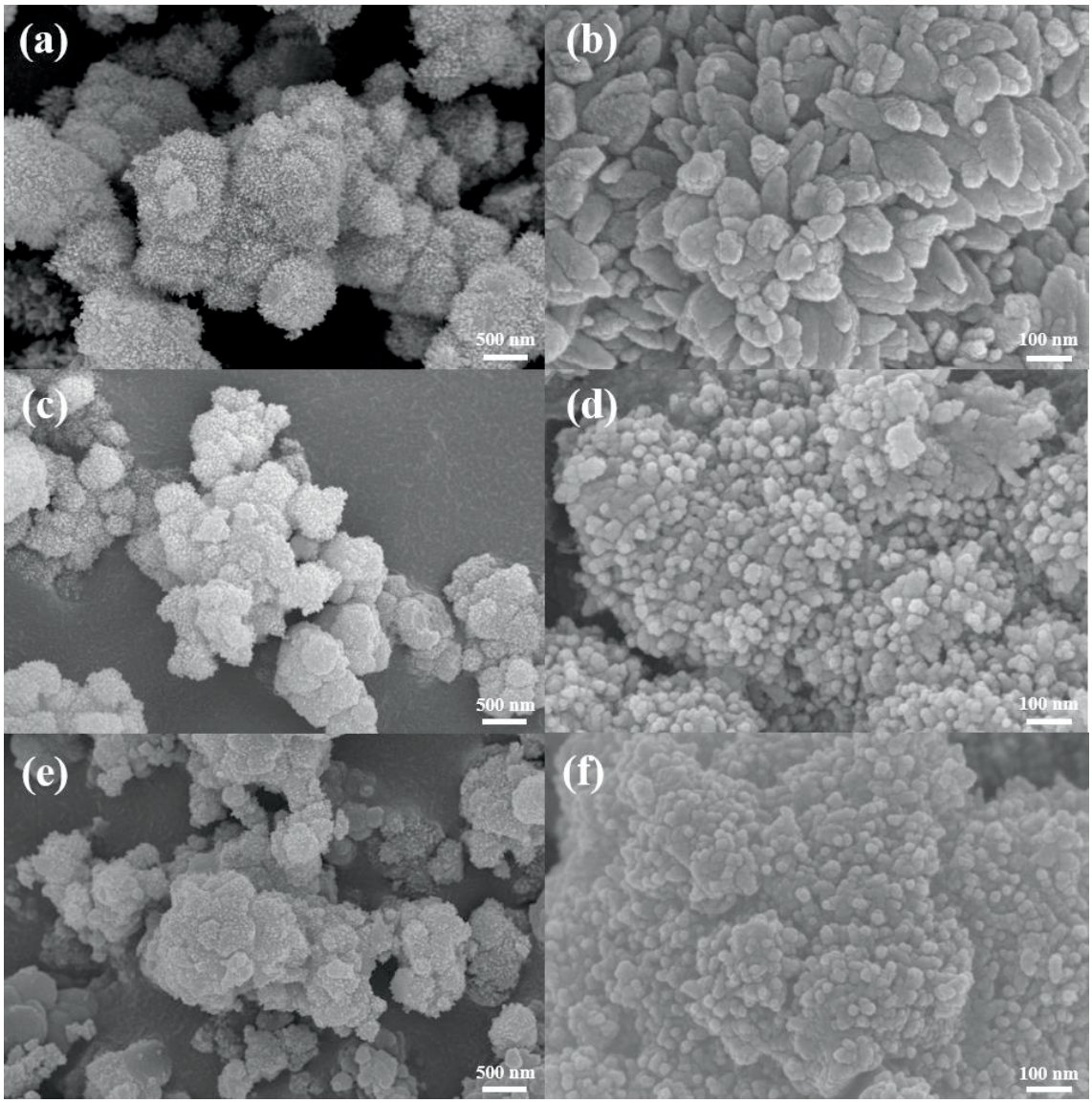

Figure 2.21. SEM images of **3-aSA$_x$**. (a, b) **3-aSA$_{0.04}$**, (c, d) **3-aSA$_{0.18}$**, and (e, f) **3-aSA$_{0.46}$**.

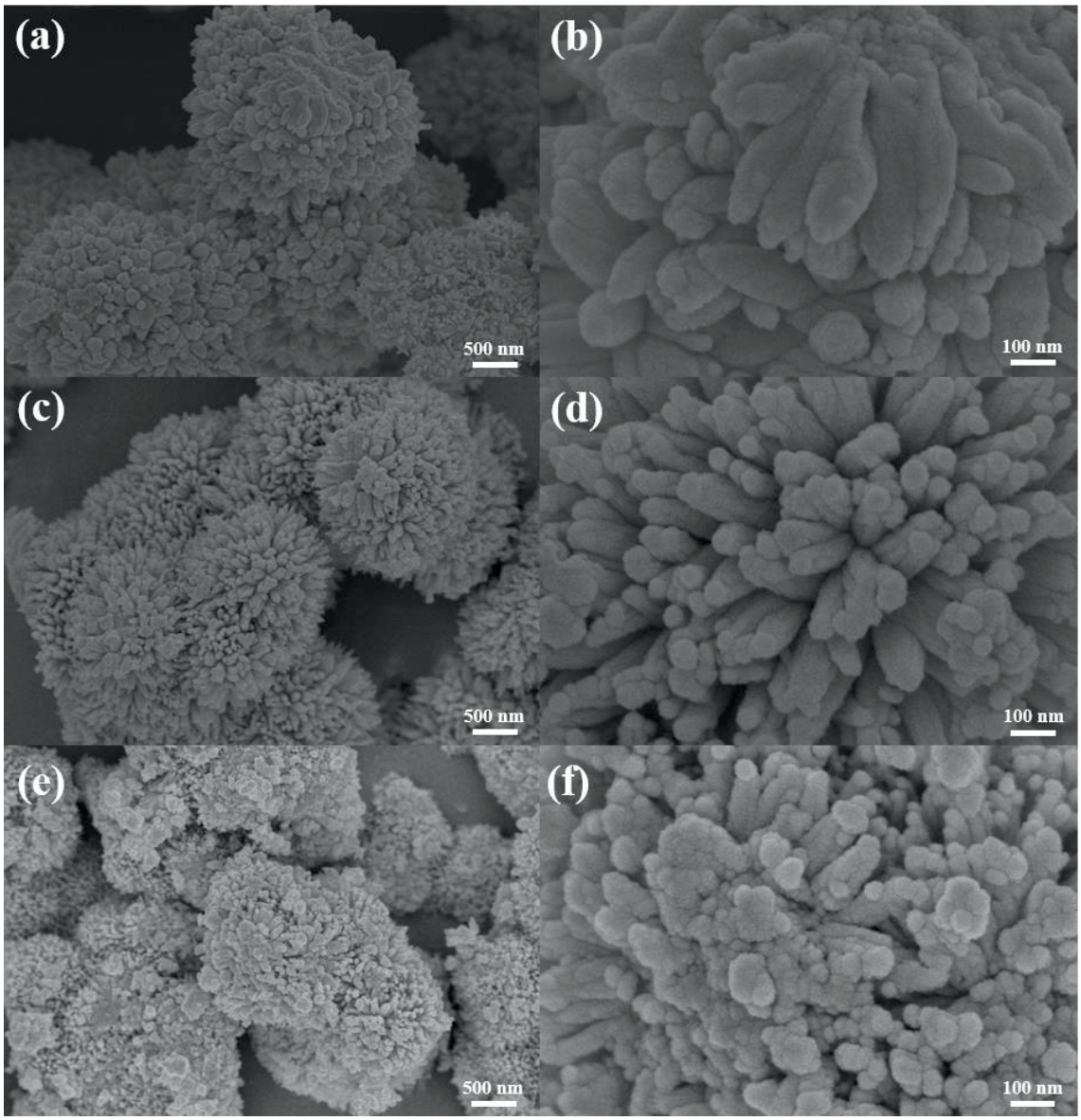

Figure 2.22. SEM images of **5-aSA$_x$**. (a, b) **5-aSA$_{0.08}$**, (c, d) **5-aSA$_{0.20}$**, and (e, f) **5-aSA$_{0.33}$**.

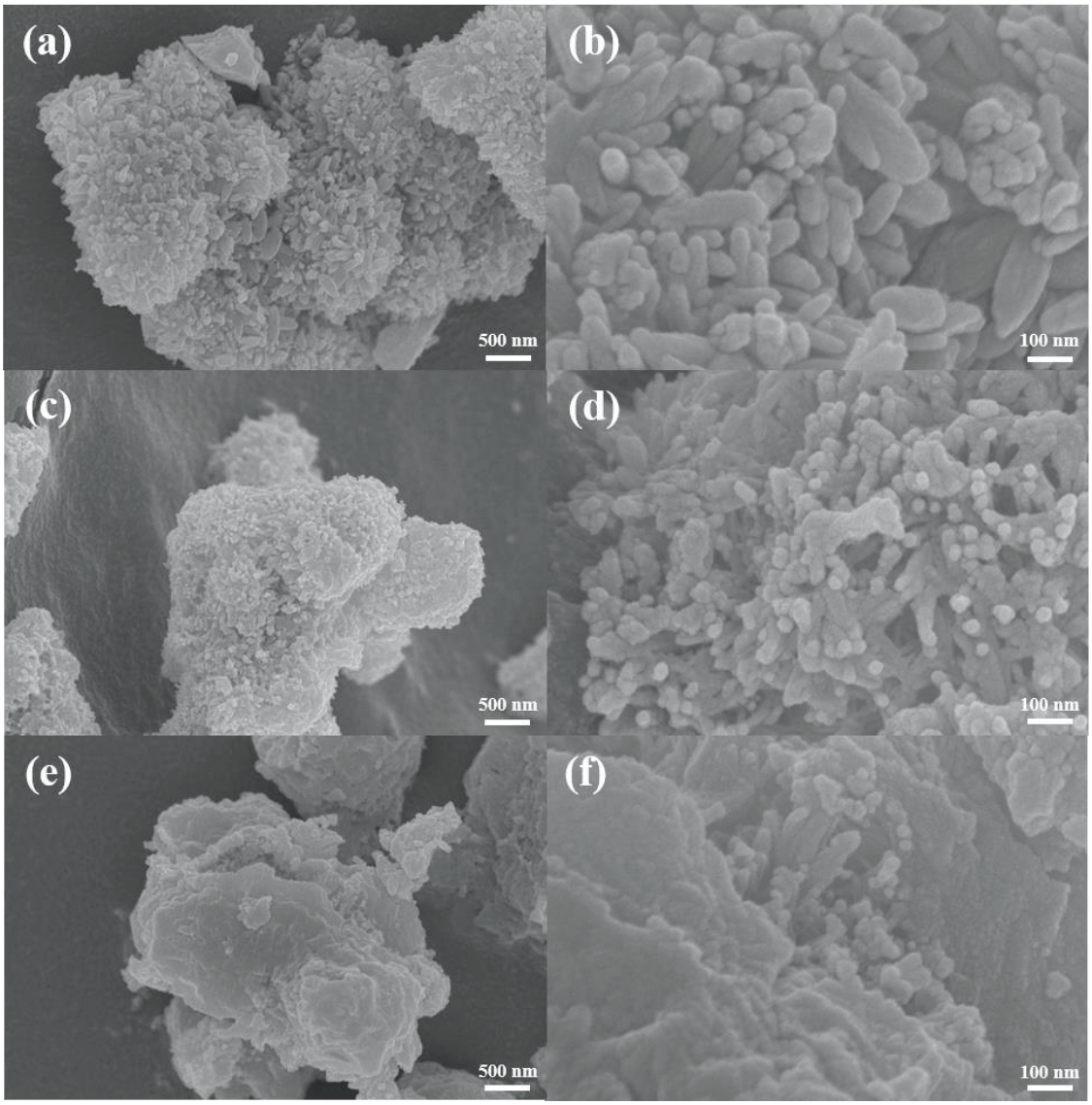

Figure 2.23. SEM images of **5-fSA$_x$**. (a, b) **5-fSA$_{0.08}$**, (c, d) **5-fSA$_{0.21}$**, and (e, f) **5-fSA$_{0.39}$**.

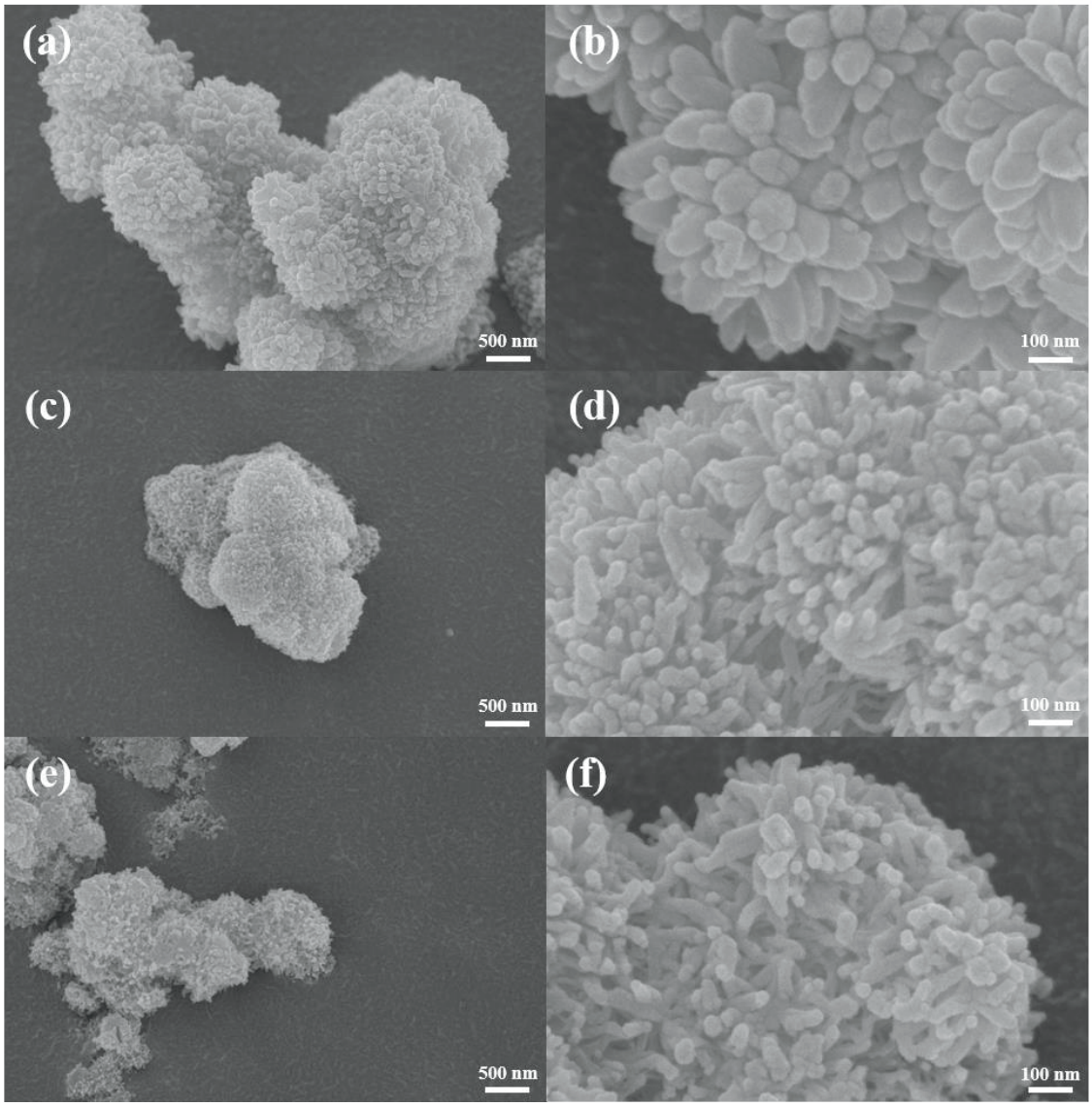

Figure 2.24. SEM images of **3-hSA$_x$**. (a, b) **3-hSA$_{0.06}$**, (c, d) **3-hSA$_{0.21}$**, and (e, f) **3-hSA$_{0.42}$**.

Thermal stability of DEMOF-74

Thermogravimetric analysis (TGA) of the defect-engineered Ni-MOF-74 derivatives showed that there are essentially no significant changes in thermal stability upon the fragmented linker installation into the framework of defect-free Ni-MOF-74 (**Figure 2.25**).

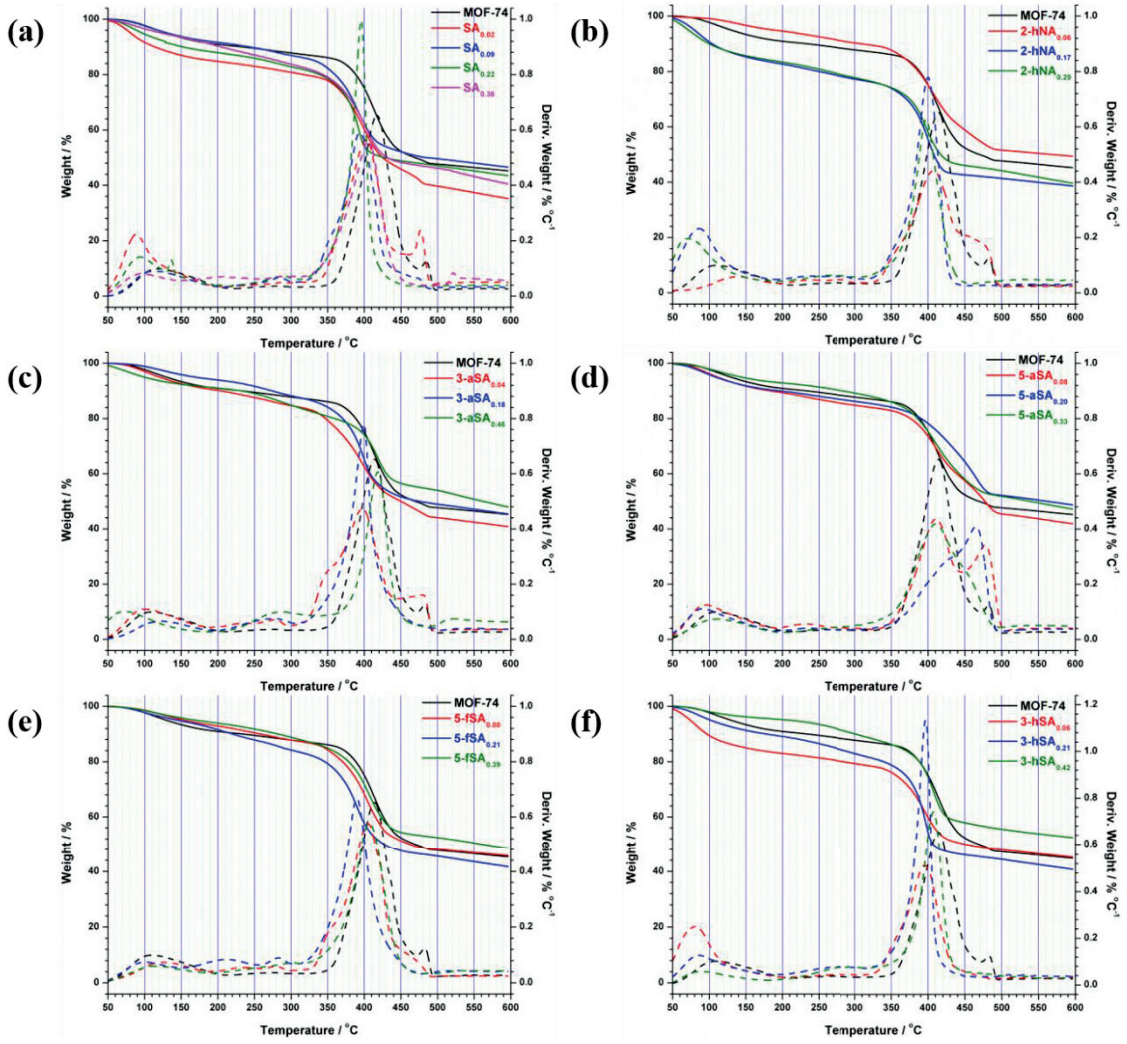

Figure 2.25. TGA of (a) **SA$_x$**, (b) **2-hNA$_x$**, (c) **3-aSA$_x$**. (d) **5-aSA$_x$** (e) **5-fSA$_x$** and (f) **3-hSA$_x$**.

Water stability of DEMOF

In contrast to the typical defect-engineered MOFs reported earlier,[25] **3-aSA$_{0.18}$** and **5-aSA$_{0.20}$** are very stable in water, and the crystallinities of both crystals were considerably maintained (**Figure 2.26**).

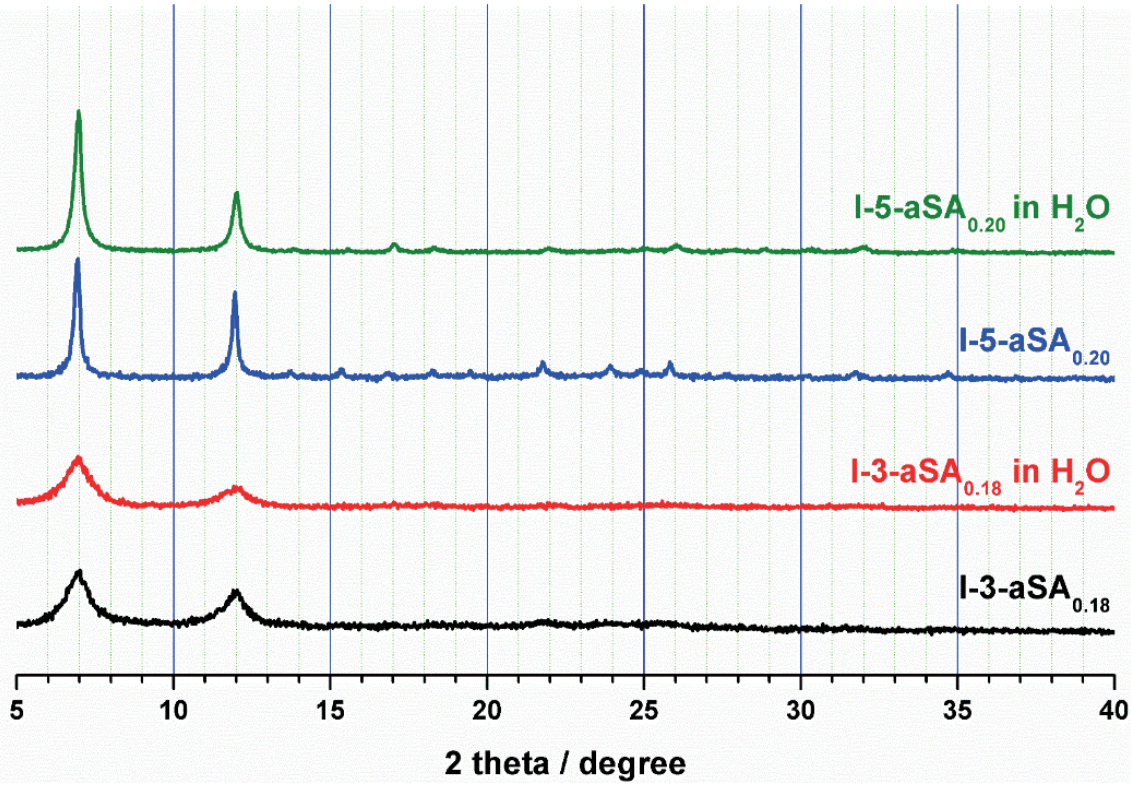

Figure 2.26. PXRD patterns of **3-aSA$_{0.18}$** and **5-aSA$_{0.20}$** soaked in H_2O for 4 d.

Porosity of Defect-Engeineered and Functionalized MOF-74 Derivatives

In order to evaluate the permanent porosities of defect-engineered functionalized MOFs, N_2 adsorption isotherms were measured at 77 K (**Figure 2.27a**). All of the activated MOFs exhibit rapid N_2 uptake at low pressures ($P/P_0 < 0.1$), which is typical for a Type I isotherm curve and is also typical characteristic for microporous solids. However, as expected, the doping of the fragmented linkers affected the porosities of the resulting defect-engineered MOFs. Pristine Ni-MOF-74 shows a Brunauer-Emmett-Teller (BET) surface area of 1085 $m^2 g^{-1}$. By introducing fragmented linkers, i.e. defect sites, into the parent framework, activated defect-engineered MOFs showed BET surface areas ranging from 627 to 1428 $m^2 g^{-1}$, depending on the doping levels of the fragmented linkers (**Table 2.2**). For SA-incorporated Ni-MOF-74 (**SA$_x$**), as the mole fraction of incorporated SA^{2-} increased, the adsorption amounts of N_2 increased to 350 $cm^3 g^{-1}$ at $P/P_0 = 0.9$ for **SA$_{0.09}$** and **SA$_{0.22}$**, which is larger than that of the pristine Ni-MOF-74 (310 $cm^3 g^{-1}$). In case of **SA$_{0.36}$**, in contrast, the adsorption amount of N_2 at $P/P_0 = 0.9$ was drastically decreased to 190 $cm^3 g^{-1}$, indicating the poor crystallinity of **SA$_{0.36}$**. This N_2 adsorption behavior for **SA$_{0.36}$** is consistent with the result observed in the PXRD pattern, where the crystallinity of **SA$_{0.36}$** is inferior to the defect-free Ni-MOF-74. The pristine Ni-MOF-74 and DEMOF-74 showed almost the same mean pore diameters that peaked at 11 Å (**Figure 2.27b**). As the mole fraction of fragmented linkers increased, the pore size distribution became wider while the average pore dimension was the same as that of the pristine Ni-MOF-74, which is related to the increase in the number of defect sites.

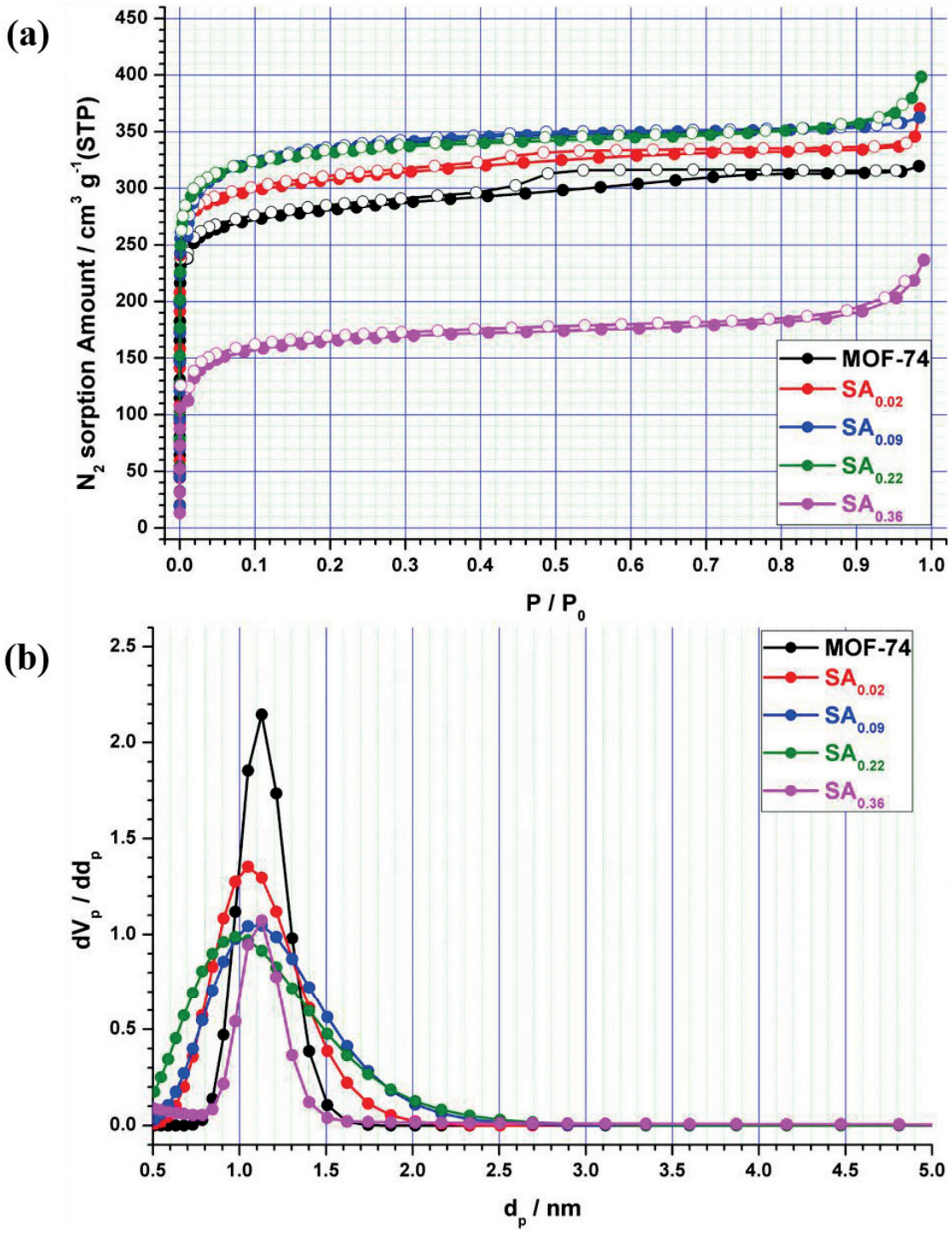

Figure 2.27. N_2 sorption isotherms of pristine MOF-74 and $\mathbf{SA_x}$ at 77 K. and (b) NLDFT pore size distribution of the pristine MOF-74 and $\mathbf{SA_x}$.

A similar trend can also be found in the N_2 adsorption of **2-hNA$_x$**, **5-fSA$_x$** and **3-hSA$_x$** (**Figures 2.28-2.30**). For **5-fSA$_x$**, while **5-fSA$_{0.10}$** and **5-fSA$_{0.22}$** exhibited the enhanced porosities with the maximum adsorption amounts of 350 cm^3 g^{-1} at P/P_0 = 0.9, whereas **5-fSA$_{0.39}$** showed slightly smaller adsorption amount (270 cm^3 g^{-1} at P/P_0 = 0.9) compared to that of the pristine Ni-MOF-74. Besides, the N_2 adsorption in **2-hNA$_{0.10}$** and **3-hSA$_{0.07}$** reached adsorption amounts as high as the N_2 uptake amounts as observed in **5-fSA$_{0.10}$**. N_2 uptake amounts of **2-hNA$_{0.20}$** and **3-hSA$_{0.26}$** were almost equivalent to that of pristine Ni-MOF-74. The N_2 adsorption amounts of **2-hNA$_{0.43}$** and **3-hSA$_{0.45}$** were smaller than that of defect-free Ni-MOF-74, and a drastic decrease in N_2 uptake amount (240 cm^3 g^{-1} at P/P_0 = 0.9) was obtained for **3-hSA$_{0.45}$**.

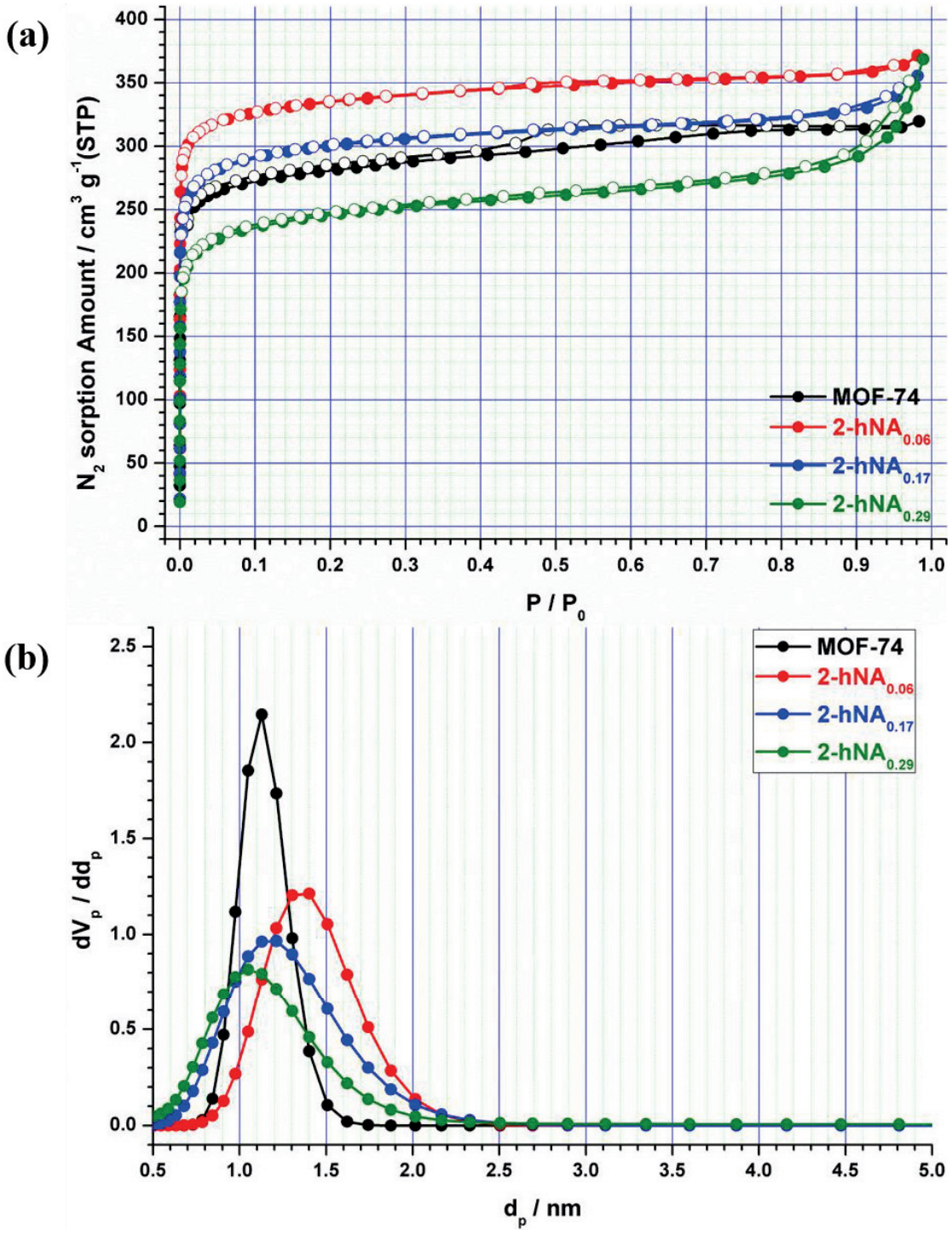

Figure 2.28. N_2 sorption isotherms of pristine MOF-74 and **2-hNA$_x$** at 77 K. and (b) NLDFT pore size distribution of the pristine MOF-74 and **2-hNA$_x$**.

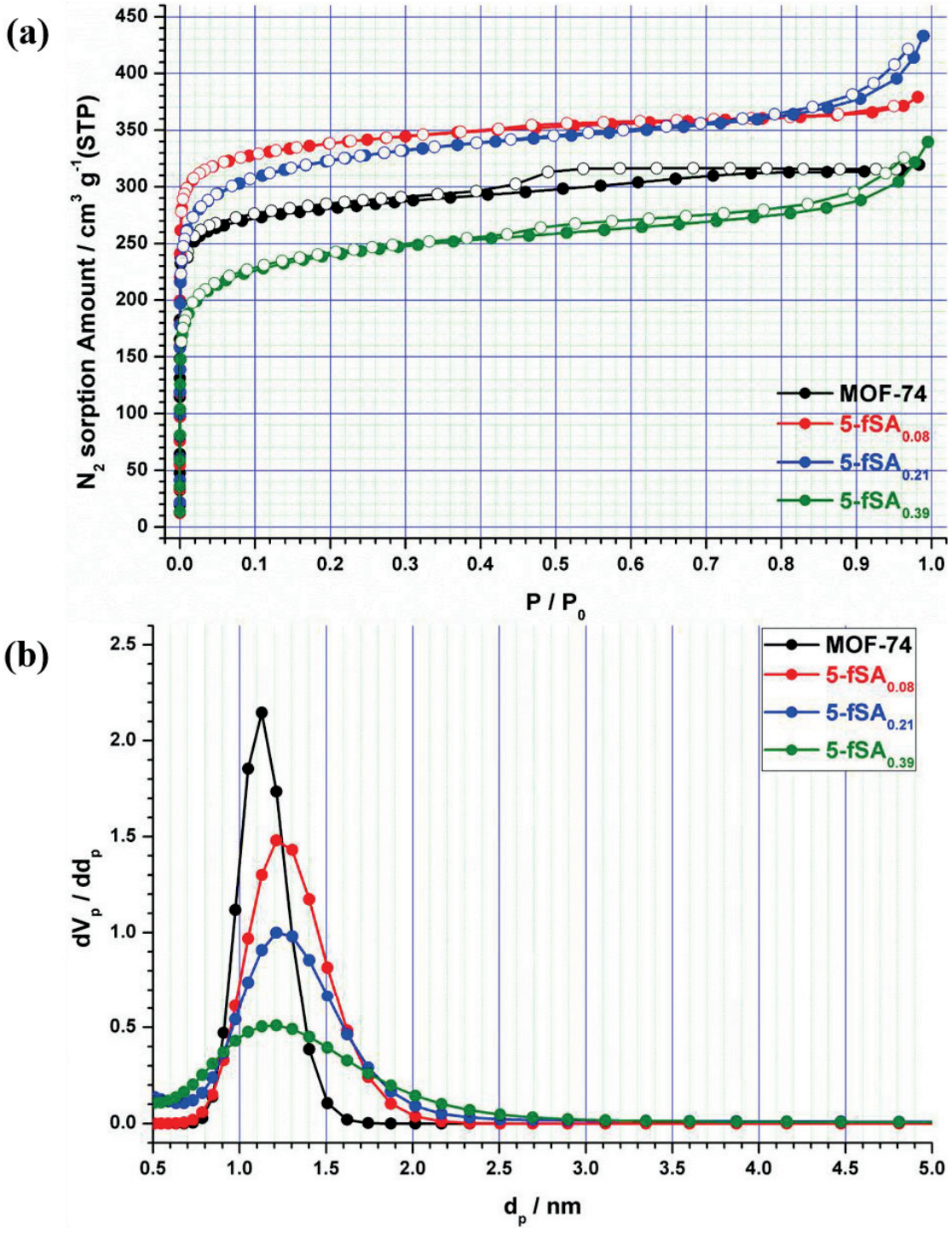

Figure 2.29. N_2 sorption isotherms of pristine MOF-74 and **5-fSA$_x$** at 77 K. and (b) NLDFT pore size distribution of the pristine MOF-74 and **5-fSA$_x$**.

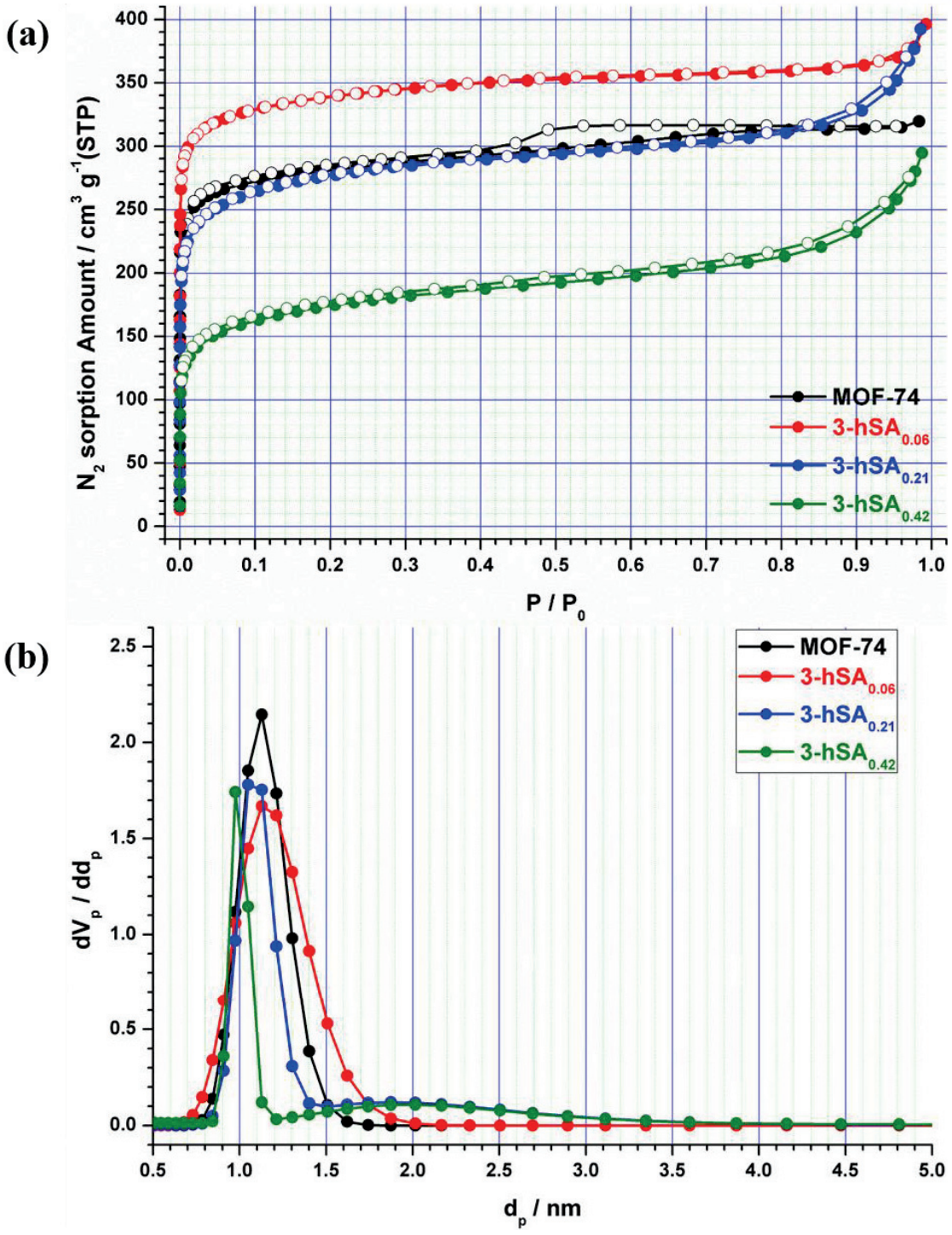

Figure 2.30. N_2 sorption isotherms of pristine MOF-74 and **3-hSA$_x$** at 77 K. and (b) NLDFT pore size distribution of the pristine MOF-74 and **3-hSA$_x$**.

Interestingly, although two fragmented linkers, 5-aSA^{2-} and 3-aSA^{2-}, have the same functional group, they exerted most significantly different effects on the porosities of resulting **5-aSA$_x$** and **3-aSA$_x$** (**Figures 2.31a** and **2.32a**). The doping of 5-aSA^{2-} led to an increase in the porosity of **5-aSA$_x$** compared to pristine Ni-MOF-74, even above a doping level of 30%. Thus, the adsorption amount of **5-aSA$_{0.20}$** reached the highest value of 420 cm^3 g^{-1} at P/P_0 = 0.9, and the adsorption amounts of **5-aSA$_{0.08}$** and **5-aSA$_{0.33}$** (ca. 370 cm^3 g^{-1} at P/P_0 = 0.9 for both) also surpassed that of the pristine Ni-MOF-74. In contrast, the amount of N_2 adsorbed in **3-aSA$_x$** increased slightly only at relatively low mole fractions (< 10%) of 3-aSA^{2-}. **3-aSA$_{0.18}$** exhibited lower N_2 uptake than the pristine Ni-MOF-74 and **3-aSA$_{0.46}$** showed almost no uptake of N_2. This observation is consistent with the results expected from PXRD analysis, where both MOFs showed poorer crystallinity than the pristine Ni-MOF-74. **3-aSA$_x$** and **5-aSA$_x$** showed almost the same mean pore diameters that peaked at 11 Å (**Figuews 2.31b** and **2.32b**). As the mole fraction of n-aSA increased, the pore size distribution became wider while the average pore dimension was the same as that of the pristine Ni-MOF-74, which is related to the increase in the number of defect sites.

Overall, it can be concluded that the enhanced porosities for defect-engineered Ni-MOF-74 derivatives were achieved by introducing the fragmented linkers up to 10 - 20% into the framework of defect-free Ni-MOF-74.

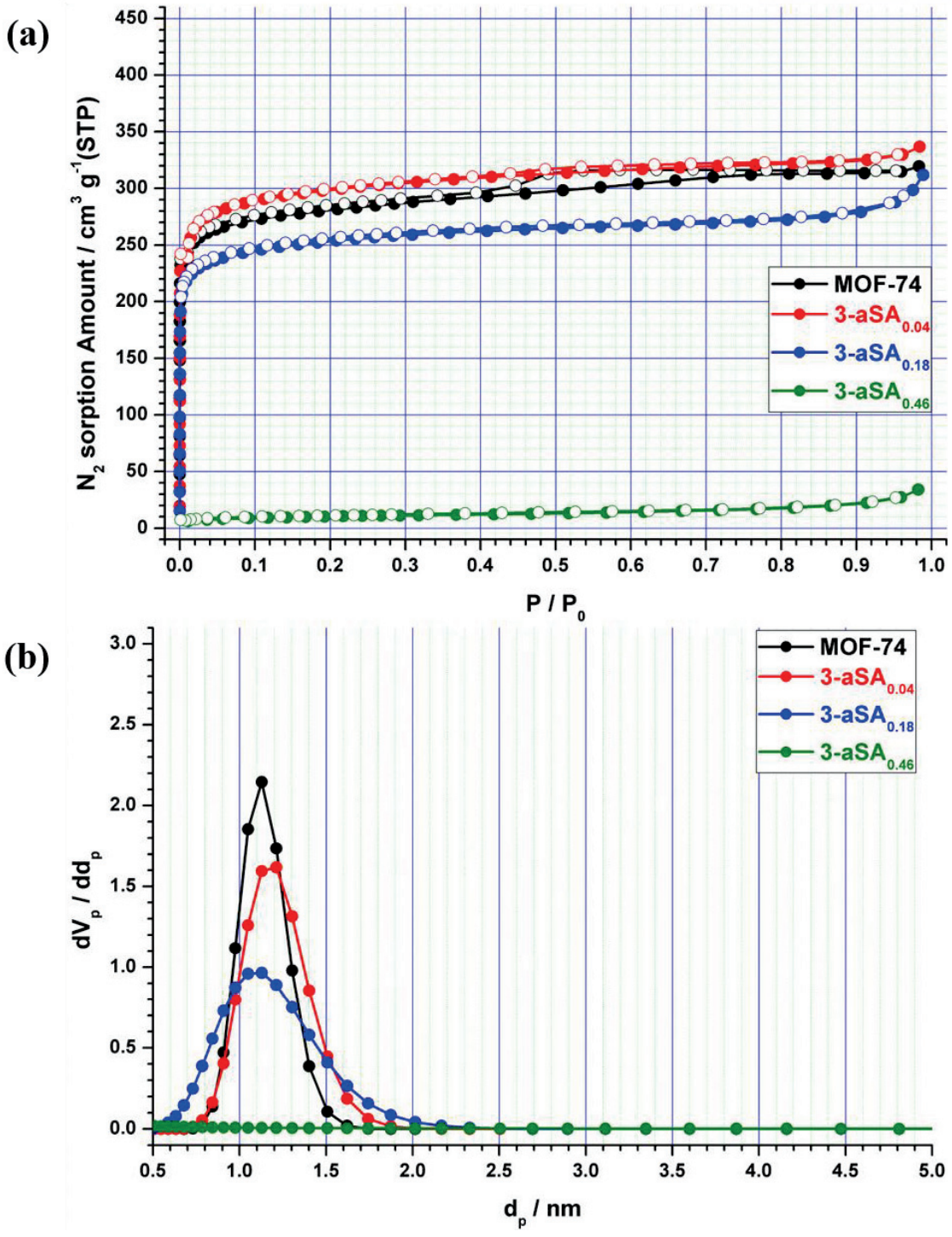

Figure 2.31. N_2 sorption isotherms of pristine MOF-74 and **3-aSA$_x$** at 77 K. and (b) NLDFT pore size distribution of the pristine MOF-74 and **3-aSA$_x$**.

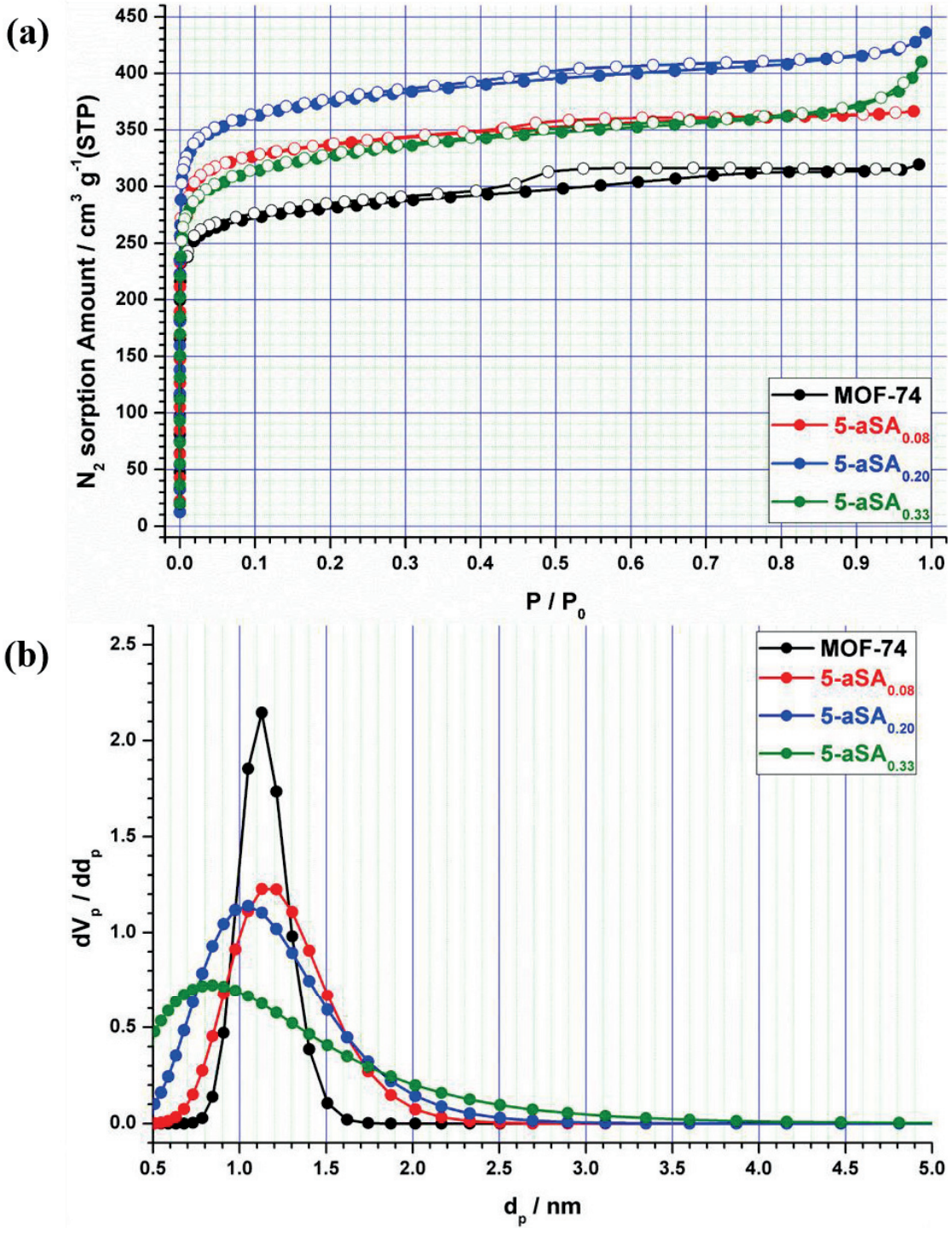

Figure 2.32. N_2 sorption isotherms of pristine MOF-74 and **5-aSA$_x$** at 77 K. and (b) NLDFT pore size distribution of the pristine MOF-74 and **5-aSA$_x$**.

Table 2.2. BET surface areas and pore volume of Ni-MOR-74, DEMOF-74.

Sample	BET / $m^2\ g^{-1}$	Pore volume / $cm^3\ g^{-1}$
Ni-MOF-74	1085	0.494
$SA_{0.02}$	1188	0.573
$SA_{0.09}$	1269	0.561
$SA_{0.22}$	1290	0.616
$SA_{0.36}$	627	0.366
2-$hNA_{0.06}$	1325	0.575
2-$hNA_{0.17}$	1156	0.550
2-$hNA_{0.29}$	934	0.570
3-$aSA_{0.04}$	1154	0.521
3-$aSA_{0.18}$	981	0.482
3-$aSA_{0.46}$	37	0.053
5-$aSA_{0.08}$	1295	0.572
5-$aSA_{0.20}$	1428	0.673
5-$aSA_{0.33}$	1247	0.635
5-$fSA_{0.08}$	1325	0.586
5-$fSA_{0.21}$	1209	0.670
5-$fSA_{0.39}$	894	0.517
3-$hSA_{0.06}$	1323	0.608
3-$hSA_{0.21}$	1042	0.607
3-$hSA_{0.42}$	640	0.456

CO_2 Adsorption Properties of Defect-engineered and Functionalized Ni-MOF-74 Derivatives.

The adsorption properties of CO_2 were also investigated at 273 and 298 K (**Figure 2.33**). In general, the introduction of an amine group is known to increase CO_2 uptake in many amine-functionalized MOFs. In this study, two kinds of amine-functionalized defect-engineered MOFs, **5-aSA$_x$** and **3-aSA$_x$**, were developed and they exhibited different CO_2 adsorption behaviors. In **5-aSA$_{0.08}$** and **5-aSA$_{0.20}$**, the enhanced CO_2 uptakes were observed at 273 and 298 K, compared to the uptake amounts of defect-free Ni-MOF-74 (150 cm^3 g^{-1} at 273 K and 1 bar, 115 cm^3 g^{-1} at 298 K and 1 bar). **5-aSA$_{0.33}$** did not show any noticeable enhancement of CO_2 uptakes at both temperatures. Meanwhile, among **3-aSA$_x$**, only **3-aSA$_{0.04}$** showed CO_2 uptakes comparable to those of defect-free Ni-MOF-74 at both temperatures, and **3-aSA$_{0.18}$** and **3-aSA$_{0.46}$** resulted in the decrease in the CO_2 uptake amounts. In particular, drastic decrease in CO_2 uptakes were observed in **3-aSA$_{0.46}$**, which is expected from the poor crystallinity of **3-aSA$_{0.46}$**.

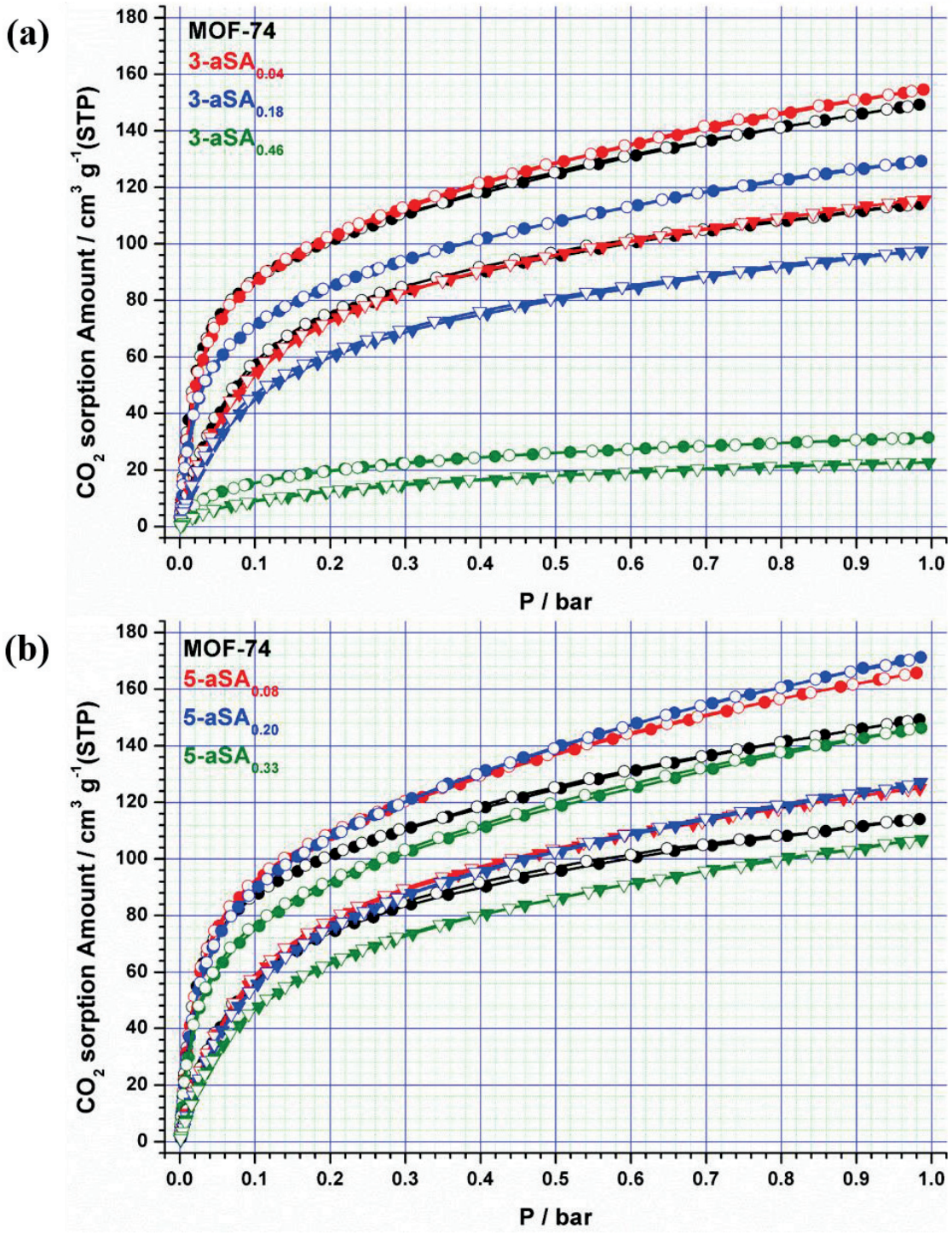

Figure 2.33. CO_2 sorption isotherms of (a) **3-aSA$_x$** and (b) **5-aSA$_x$** at 273 K (round circle) and 298 K (reverse triangle).

The CO_2 adsorption behaviors of $\mathbf{SA_x}$ derivatives were similar to those of $\mathbf{5\text{-}aSA_x}$ (**Figure 2.34**). The enhanced CO_2 uptakes were achieved by the incorporation of SA^{2-} up to ca. 20% and $\mathbf{SA_{0.09}}$ showed the maximum CO_2 uptake amounts. $\mathbf{2\text{-}hNA_x}$, $\mathbf{5\text{-}fSA_x}$ and $\mathbf{3\text{-}hSA_x}$ derivatives also behaved in a similar fashion for CO_2 adsorption. They showed the maximum CO_2 uptakes at ca. 10% incorporation of fragmented linkers, then the CO_2 uptake amounts were gradually decreased. Interestingly, the maximum CO_2 uptake amounts are almost the same regardless of the type of fragmented linkers except for H_2-3-aSA.

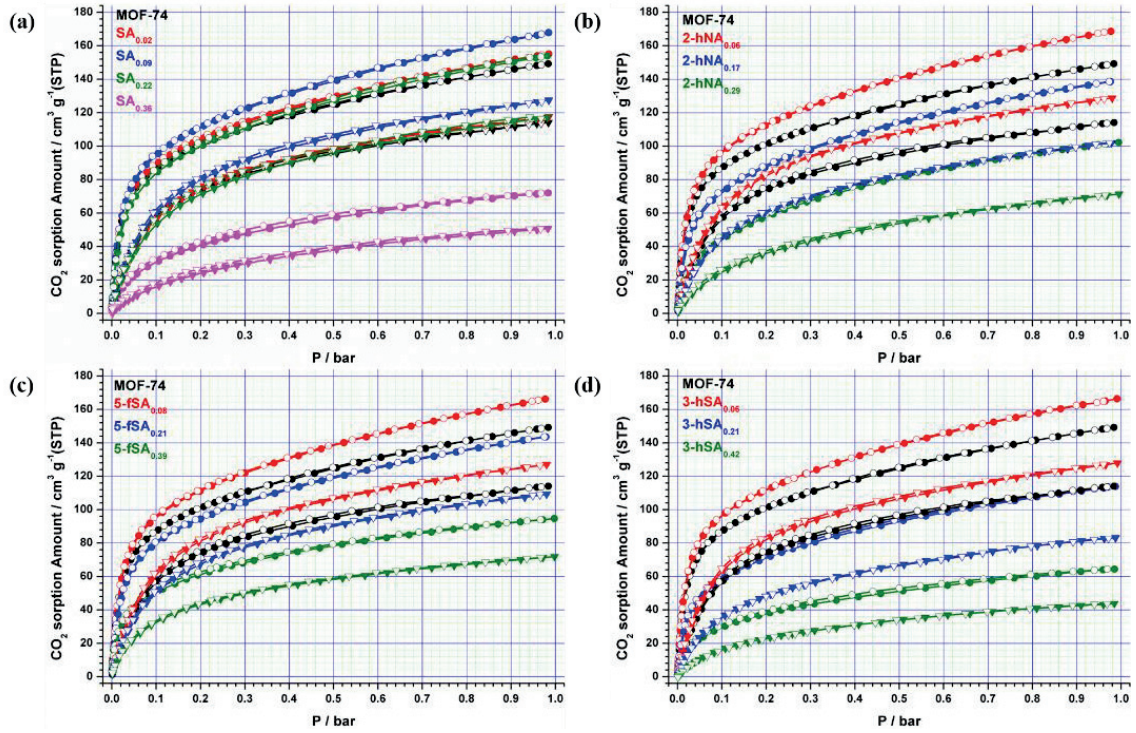

Figure 2.34. CO_2 sorption isotherms of (a) $\mathbf{SA_x}$, (b) $\mathbf{2\text{-}hNA_x}$, (c) $\mathbf{5\text{-}fSA_x}$ and (d) $\mathbf{3\text{-}hSA_x}$ at 273 K (round circle) and 298 K (reverse triangle).

Large isosteric heat of adsorption (Q_{st}) is useful for storage applications. To investigate the effects of the fragmented linker installation on adsorption enthalpy, the isosteric heats of adsorption were determined using CO_2 adsorption isotherms obtained at 273 and 298 K (**Figure 2.35**). All the heats of adsorption were calculated by fitting adsorption isotherms with a virial-type equation. For all defect-engineered MOFs, the Q_{st} values ranged between 35 and 38 kJ mol^{-1} at the low loadings of CO_2, and the Q_{st} values gradually decreased as the uptake amounts of CO_2 increased. Low energy would be needed to reduce the regeneration cost to release the CO_2. [30] Despite Up to 20% increase in CO_2 adsorption, Q_{st} was decreased by 10%. This can have the advantage of requiring less energy and cost to remove CO_2 from framework during the separation process.

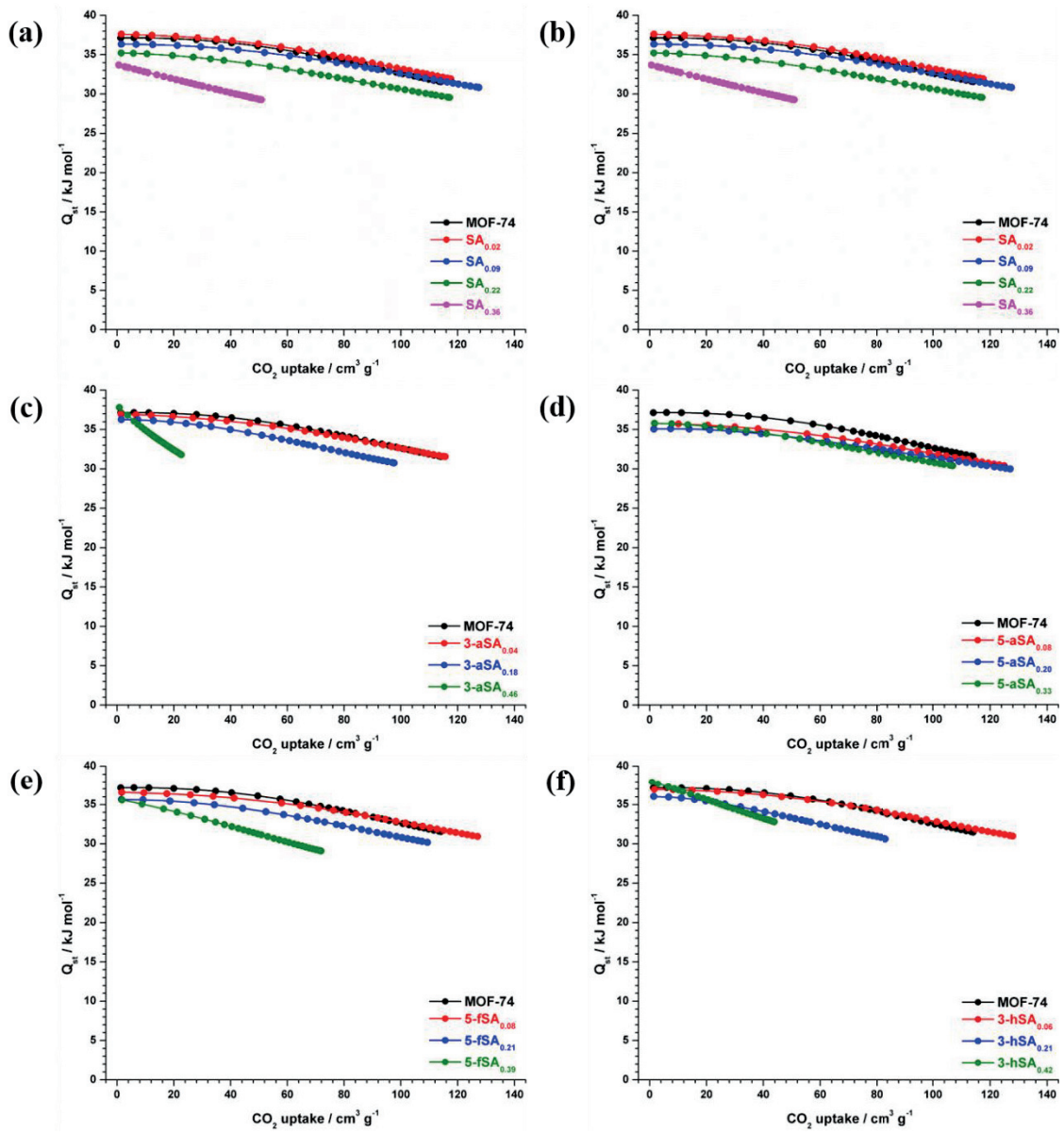

Figure 2.35. Isosteric heats of adsorption (Q_{st}) on CO_2 of (a) **SA_x** (b) **2-hNA_x**, (c) **3-aSA_x**, (d) **5-aSA_x**, (e) **5-fSA_x** and (f) **3-hSA_x**.

H_2 Adsorption Properties of Defect-engineered and Functionalized Ni-MOF-74 Derivatives.

H_2 adsorption isotherms were measured to investigate the effect of the fragmented linker installation on the adsorption capacity (**Figure 2.36**). All the activated defect-engineered MOFs showed the reversible H_2 adsorption behavior at 77 K except for **3-aSA$_{0.46}$**. It is found that the trend in H_2 adsorption behavior of defect-engineered MOFs is closely related to that of N_2 adsorption behavior. For example, **5-aSA$_{0.20}$** exhibited the highest H_2 adsorption amount (231 cm^3 g^{-1} at 1 bar and 77 K) among all the defect-engineered Ni-MOF-74 derivatives synthesized in this study. Even **5-aSA$_{0.20}$** and **5-aSA$_{0.33}$** showed the enhanced H_2 adsorption amount compared to that of the pristine Ni-MOF-74 that is known to have the highest H_2 adsorption capacities among M-MOF-74 (M = Zn, Co, Ni, Mn, and Mg).[31] In contrast, the incorporation of 3-aSA^{2-} and 3-hSA^{2-} led to somewhat unfavorable effects on the H_2 adsorption properties. Only **3-aSA$_{0.04}$** and **3-hSA$_{0.07}$** showed slightly enhanced H_2 adsorption amounts (186 cm^3 g^{-1} for **3-aSA$_{0.04}$**, 211 cm^3 g^{-1} for **3-hSA$_{0.07}$** at 1 bar and 77 K, respectively), and the others exhibited lower H_2 adsorption amounts than that of defect-free Ni-MOF-74. **3-aSA$_{0.46}$** showed an extremely low H_2 uptake amount (31.8 cm^3 g^{-1}) with hysteresis in a desorption branch, which is not surprising because it showed almost no N_2 uptake at 77 K. For **SA$_x$**, **2-hNA$_x$** and **5-fSA$_x$**, the enhanced H_2 uptakes can be obtained only below approximately 20% of the incorporation levels, and the higher incorporation levels (>20%) of the fragmented linkers resulted in lower H_2 uptake amounts.

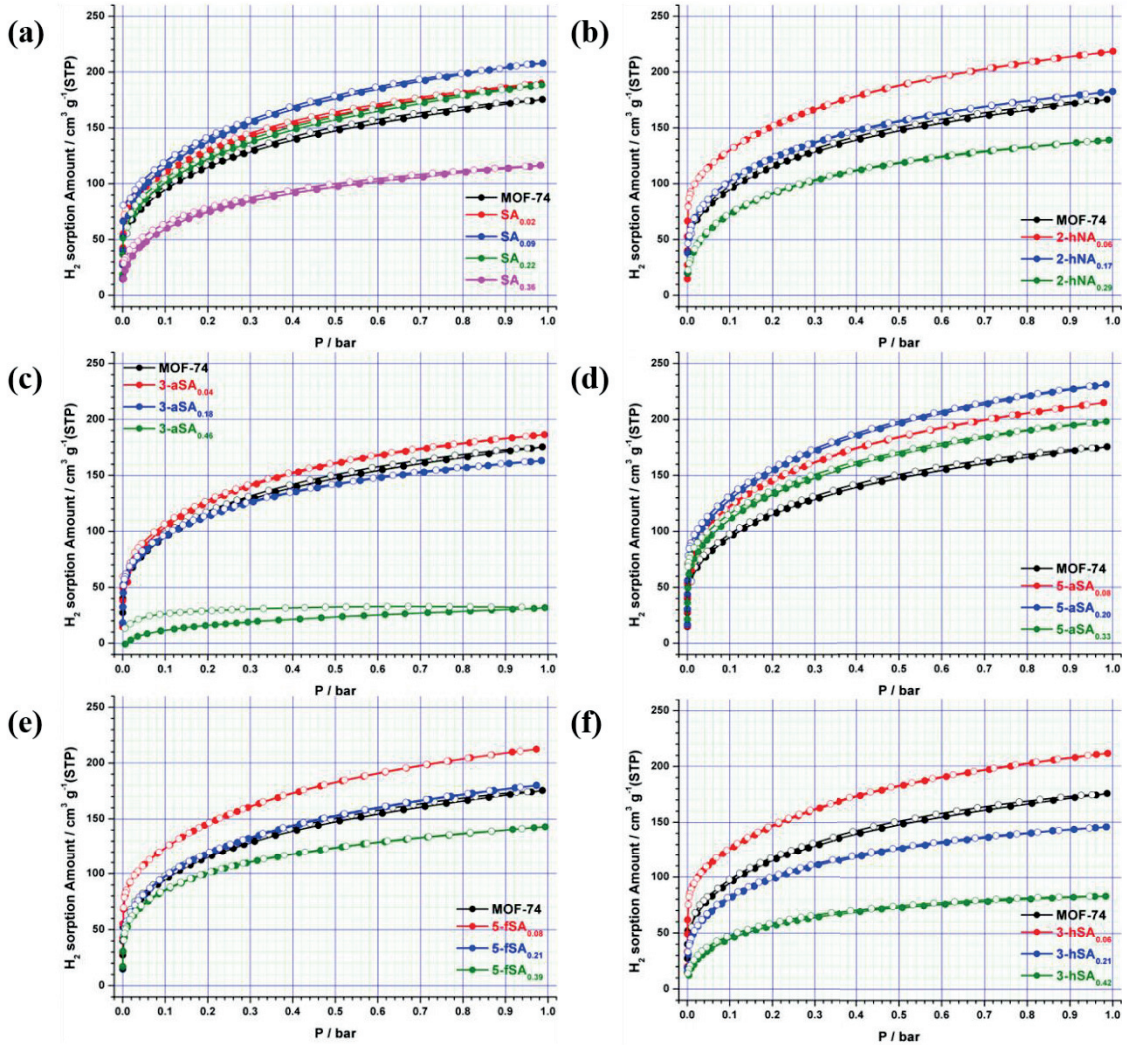

Figure 2.36. H_2 sorption isotherms of (a) **SA$_x$**, (b) **2-hNA$_x$**, (c) **3-aSA$_x$**, (d) **5-aSA$_x$**, (e) **5-fSA$_x$** and (f) **3-hSA$_x$** at 77 K.

2.4 Conclusions

In summary, we have systematically investigated the synthesis of functionalized defect-engineered Ni-MOF-74, which is achieved by using the fragmented linker installation approach. The functionalization of the framework was accomplished by partially mixing the original linker 2,5-dioxido-1,4-benzendicarboxylic acid (H_4DOBDC) with salicylate derivatives, including salicylic acid (H_2SA), 3-aminosalicylic acid (H_2-3-aSA), 5-aminosalicylic acid (H_2-5-aSA), 5-formylsalicylic acid (H_2-5-fSA), 3-hydroxysalicylic acid (H_2-3-hSA) and 2-hydroxynicotinic acid (H_2-2-hNA). Below the approximated 20% doping level of each fragmented linker, all resultant MOFs retained good crystallinity and permanent porosity even with defects in the framework. Furthermore, the functionalized MOFs containing the fragmented linkers up to ca. 20% doping levels showed enhanced surface areas compared to the pristine Ni-MOF-74. They also showed improved adsorption capacities for H_2 and CO_2 at lower loading (<10%) of fragmented linkers and lower isosteric heat of adsorption (Q_{st}) will be beneficial for gas separation. In addition, various functional groups are advantageous to covalent bond sites for post-synthetic modification.

2.5 References

1. Rosi, N. L.; Kim, J.; Eddaoudi, M.; Chen, B.; Keeffe, M. O.; Yaghi, O. M. Rod Packings and Metal-Organic Frameworks Constructed from Rod-Shaped Secondary Building Units. *J. Am. Chem. Soc.* **2005**, 127, 1504−1518.
2. Caskey, S. R.; Wong-Foy, A. G.; Matzger, A. J. Dramatic Tuning of Carbon Dioxide Uptake via Metal Substitution in a Coordination Polymer with Cylindrical Pores. *J. Am. Chem. Soc*. **2008**, *130*, 10870−10871.
3. Wang, L. J.; Deng, H.; Furukawa, H.; Gándara, F.; Cordova, K. E.; Peri, D.; Yaghi, O. M. Synthesis and Characterization of Metal−Organic Framework-74 Containing 2, 4, 6, 8, and 10 Different Metals. *Inorg. Chem*. **2014**, 53, 5881-5883.
4. Bloch, E. D.; Murray, L. J.; Queen, W. L.; Chavan, S.; Maximoff, S. N.; Bigi, J. P.; Krishna, R.; Peterson, V. K.; Grandjean, F.; Long, G. J.; Smit, B.; Bordiga, S.; Brown, C. M.; Long, J. R. Selective Binding of O_2 over N_2 in a Redox-Active Metal-Organic Framework with Open Iron(II) Coordination Sites. *J. Am. Chem. Soc*. **2011**, *133*, 14814−14822.
5. Tan, K.; Zuluaga, S.; Gong, Q.; Canepa, P.; Wang, H.; Li, J.; Chabal, Y. J.; Thonhauser, T. Water Reaction Mechanism in Metal Organic Frameworks with Coordinatively Unsaturated Metal Ions: MOF-74. *Chem. Mater.* **2014**, 26, 6886-6895.
6. Zurrer, T.; Wong, K.; Horlyck, J.; Lovell, E. C.; Wright, J.; Bedford, N. M.; Han, Z.; Liang, K.; Scott, J.; Amal, R. Mixed-Metal MOF-74 Templated Catalysts for Efficient Carbon Dioxide Capture and Methanation. *Adv. Funct. Mater*. **2020**, 31, 2007624.
7. McKinlay, A. C.; Xiao, B.; Wragg, D. S.; Wheatley, P. S.; Megson, I. L.; Morris, R. E. Exceptional Behavior over the Whole Adsorption-Storage-Delivery Cycle for NO in Porous Metal Organic Frameworks. *J. Am. Chem. Soc*. **2008**, *130*, 10440−10444.
8. Kim, J. Y.; Balderas-Xicohténcatl, R.; Zhang, L.; Kang, S. G.; Hirscher, M.; Oh, H.; Moon, H. R. Exploiting Diffusion Barrier and Chemical Affinity of Metal−Organic Frameworks for Efficient Hydrogen Isotope Separation. *J. Am. Chem. Soc*. **2017**, *139*, 15135−15141.
9. Yang, D-A.; Cho, H-Y.; Kim, J.; Yang, S-T.; Ahn, W-S. CO_2 capture and conversion using Mg-MOF-74 prepared by a sonochemical method. *Energy Environ. Sci*. **2012**, *5*, 6465−6473.
10. Wu, D.; Guo, Z.; Yin, X.; Pang, Q.; Tu, B.; Zhang, L.; Wang, Y-G.; Li, Q. Metal–Organic Frameworks as Cathode Materials for Li–O_2 Batteries. *Adv. Mater*. **2014**, *26*, 3258−3262.
11. Sarango-Ramírez, M. K.; Lim, D-W.; Kolokolov, D. I.; Khudozhitkov, Al. E.; Stepanov, A. G.; Kitagawa, H. Superprotonic Conductivity in Metal−Organic Framework via Solvent-Free Coordinative Urea Insertion. *J. Am. Chem. Soc*. **2020**, *142*, 6861−6865.
12. Deng, H.; Grunder, S.; Cordova, K. E.; Valente, C.; Furukawa, H.; Hmadeh, M.; Gándara, F.; Whalley, A. C.; Liu, Z.; Asahina, S.; Kazumori, H.; Keeffe, M. O, Terasaki, O.; Stoddart, F.; Yaghi, O. M. Large-Pore Apertures in a Series of Metal-Organic Frameworks. *Science*. **2012**, 336, 1018-

1023.

13. Wang. Z.; Cohen, S. M.; Tandem Modification of Metal-Organic Frameworks by a Postsynthetic Approach. *Angew. Chem. Int. Ed*. **2008**, 47, 4699-4702.
14. Lu, W.; Wei, Z.; Gu, Z.-Y.; Liu, T.-F.; Park, J.; Park, J.; Tian, J.; Zhang, M.; Zhang, Q.; Ill, T. G.; Bosch, M.; Zhou, H.-C. Tuning the structure and function of metal–organic frameworks via linker design. *Chem. Soc. Rev*. **2014**, 43, 5561-5593.
15. Cohen, S. M. Postsynthetic Methods for the Functionalization of Metal-Organic Frameworks. *Chem. Rev*. **2012**, 112, 970-1000.
16. Yin, Z.; Wan, S.; Yang, J.; Kurmoo, M.; Zeng, M.-H.; Recent advances in post-synthetic modification of metal–organic frameworks: New types and tandem reactions. *Coord. Chem. Rev*. **2019**, 378, 500-512.
17. McDonald, T. M.; Lee, W. R.; Mason, J. A.; Wiers, B. M.; Hong, C. S.; Long, J. R. Capture of Carbon Dioxide from Air and Flue Gas in the Alkylamine-Appended Metal−Organic Framework mmen-Mg_2(dobpdc). *J. Am. Chem. Soc*. **2012**, *134*, 7056−7065.
18. Lee, B.; Moon, D.; Park, J. Microscopic and Mesoscopic Dual Postsynthetic Modifications of Metal–Organic Frameworks. *Angew. Chem. Int. Ed*. **2020**, 59, 13793-13799.
19. Fracaroli, A. M.; Furukawa, H.; Suzuki, M.; Dodd, M.; Okajima, S.; Gándara, F.; Reimer, J. A.; Yaghi, O. M. Metal−Organic Frameworks with Precisely Designed Interior for Carbon Dioxide Capture in the Presence of Water. *J. Am. Chem. Soc*. **2014**, 136, 8863-8866.
20. Fracaroli, A. M.; Siman, P.; Nagib, D. A.; Suzuki, M.; Furukawa, H.; Toste, F. D.; Yaghi, O. M. Seven Post-synthetic Covalent Reactions in Tandem Leading to Enzyme-like Complexity within Metal−Organic Framework Crystals. *J. Am. Chem. Soc*. **2016**, 138, 8352-8355.
21. Fang, Z.; Dürholt, J. P.; Kauer, M.; Zhang, W.; Lochenie, C.; Jee, B.; Albada, B.; Metzler-Nolte, N.; Pöppl, A.; Weber, B.; Muhler, M.; Wang, Y.; Schmid, R.; Fischer, R. A. Structural Complexity in Metal−Organic Frameworks: Simultaneous Modification of Open Metal Sites and Hierarchical Porosity by Systematic Doping with Defective Linkers. *J. Am. Chem. Soc*. **2014**, *136*, 9627−9636.
22. Park, J.; Wang, Z. U.; Sun, L-B.; Chen, Y-P.; Zhou, H-C. Introduction of Functionalized Mesopores to Metal−Organic Frameworks via Metal−Ligand−Fragment Coassembly. *J. Am. Chem. Soc*. **2012**, *134*, 20110−20116.
23. Kozachuk, O.; Luz, I.; Xamena, F. X. L.; Noei, H.; Kauer, M.; Albada, H. B.; Bloch, E. D.; Marler, B.; Wang, Y.; Muhler, M.; Fischer, R. A. Multifunctional, Defect-Engineered Metal–Organic Frameworks with Ruthenium Centers: Sorption and Catalytic Properties. *Angew. Chem. Int. Ed*. **2014**, 53, 7058-7062.
24. Fang, Z.; Bueken, B.; De Vos, D. E.; Fischer, R. A. Defect-Engineered Metal-Organic Frameworks. *Angew. Chem. Int. Ed*. **2015**, 54, 7234-7254.

25. Dissegna, S.; Epp, K.; Heinz, W. R.; Kieslich, G.; Fischer, R. A. Defective Metal-Organic Frameworks. *Adv. Mater*. **2018**, 30, 1704501.
26. El-Gamel, N. E. A. Generation of Defect-Modulated Metal–Organic Frameworks by Fragmented-Linker Co-Assembly of CPO-27(M) Frameworks. *Eur. J. Inorg. Chem*. **2015**, *8*, 1351−1358.
27. Wu, D.; Yan, W.; Xu, H.; Zhang, E.; Li, Q. Defect engineering of Mn-based MOFs with rod-shaped building units by organic linker fragmentation. *Inorg. Chim. Acta*. **2017**, *460*, 93−98.
28. Villajos, J. A.; Jagorel, N.; Reinsch, S.; Emmerling, F. Increasing Exposed Metal Site Accessibility in a Co-MOF-74 Material With Induced Structure-Defects. *Front. Mater*. **2019**, *6*, 230.
29. Pachfule, P.; Shinde, D.; Majumder, M.; Xu, Q. Fabrication of carbon nanorods and graphene nanoribbons from a metal–organic framework. *Nat. Chem*, **2016**, *8*, 718−724.
30. Sumida, K.; Rogow, D. L.; Mason, J. A.; McDonald, T. M.; Bloch, E. D.; Herm, Z. R.; Bae, T.-H.; Long, J. R. Carbon Dioxide Capture in Metal-Organic Framework. *Chem. Rev*. **2012**, 112, 724-781.
31. Zhou, W.; Wu, H.; Yildirim, T. Enhanced H_2 Adsorption in Isostructural Metal-Organic Frameworks with Open Metal Sites: Strong Dependence of the Binding Strength on Metal Ions. *J. Am. Chem. Soc*. **2008**, 130, 15268-15269.

Chapter III

Amine-tagged Fragmented Ligand Installation for Covalent Modification of MOF-74

3.1 Introduction

MOF-74 is one of the most studied metal-organic frameworks (MOFs) because it is highly stable in various solvents and has a high density of potential open metal sites in the framework.[1–6] The dative post-synthetic modification (PSM) of the MOF-74 monodentate solvent site (i.e., the potential open metal site) has given it enhanced performance in various applications, such as gas storage,[7] selective separation,[8] and proton conductivity.[9] However, only a few applications in a solution have been reported[10–12] because the ligand bound to the open metal site is released in the solution,[13] nullifying the dative PSM. The covalent PSM of MOF-74 is expected to give MOF-74 new physical and chemical properties that have not been reported so far, which will open up new opportunities in unexplored fields. However, the covalent PSM of MOF-74 is challenging because the synthesis of functionalized 2,5-dioxido-1,4-benzenedicarboxylic acid (H_4DOBDC) is very difficult. Moreover, the introduction of functionalized DOBDC is likely to increase steric hindrance between adjacent functionalized DOBDCs, inhibiting the formation of the isoreticular framework. Therefore, no covalent PSM of MOF-74 has been reported so far.

Herein, we report, for the first time, the covalent modification of amine-tagged defect-engineered Ni-MOF-74 (DEMOF-I) and Ni_2(DOBPDC)[14] (DOBPDC^{4-} = 4,4'-dioxido-3,3'-biphenyldicarboxylate) (DEMOF-II) (**Figure 3.1**). The introduction of amino groups into the MOF was achieved by direct solvothermal synthesis using n-aminosalicylic acid (H_2n-aSA) as a fragmented organic ligand. The amine-tagged DEMOF-I retains its crystallinity and permanent porosity even with defect sites in the framework. Below the approximated 20% doping level of n-aminosalicylate (n-aSA), all MOFs showed improved adsorption capacity for N_2. By covalent PSM, the amino group of DEMOF-I was converted to an iminopyridine group by reacting with pyridine aldehyde. Subsequent post-synthetic metalation produced a Pd(II)-incorporated catalyst. The catalyst showed highly efficient, size-selective, and recyclable catalytic performance for the Suzuki–Miyaura cross-coupling reaction of phenylboronic acid and a series of aryl bromides.

A fragmented ligand is often used either as a modulator[15,16] or as a defect generating dopant[16–18] during the synthesis of MOFs. Since MOF-74 does not allow functionalized DOBDC in the framework, we used a functionalized DOBDC fragment as a dopant during the *de novo* synthesis of the amine-tagged defective MOF-74. Recently, several mixed-ligand M-MOF-74 (M= Mg, Mn, Co, and Ni) have been synthesized by doping 2-hydroxy-1,4-benzenedicarboxylate (BDC-OH).[19–21] Conversely, fragmented carboxylate ligands without hydroxyl groups can only be doped into the framework at very low concentrations. This suggests that the two functional groups of DOBDC, −OH and –COOH, are required to participate simultaneously in the assembly of the mixed-ligand M-MOF-74. However, the attempt to co-assemble salicylate (SA) in Mn-MOF-74 was not successful.[20] Meanwhile, in the reaction

of zinc and H_4DOBDC in the presence of salicylic acid (H_2SA), the H_2SA only acted as a modulator, and Zn-MOF-74 grew in the form of a nano-sized rod.[22] With this information, we attempted to find a proper doping condition, using H_2SA as a fragmented ligand because many salicylic acid derivatives with diverse functional groups are available. As functionalized fragments, we judiciously chose 5- and 3-aminosalicylic acid because an amino group is suitable for further covalent PSM with many organic functional groups.[23,24]

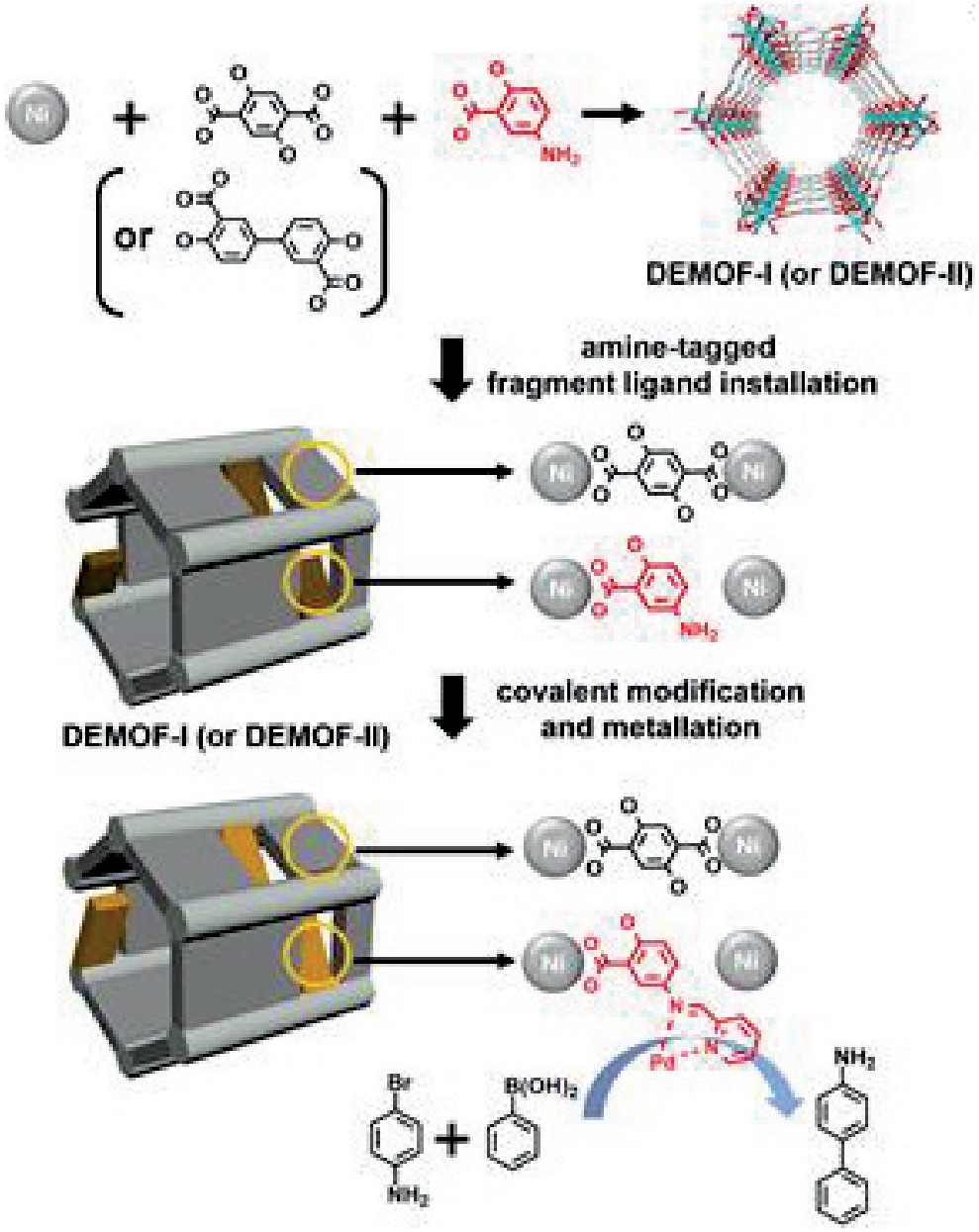

Figure 3.1. Covalent modification and metalation of DEMOF-I (or DEMOF-II) prepared by *de novo* solvothermal reaction, employing the mixed ligands, DOBDC (or DOBPDC), and an amine-tagged fragment, and the Suzuki–Miyaura cross-coupling reaction using Pd-incorporated DEMOF-I as a heterogeneous catalyst.

3.2 Experimental Section

General Procedures

All reagents were purchased from commercial sources and used without further purification. Powder X-ray diffraction (PXRD) data were recorded using a Bruker D2 Phaser automated diffractometer at 23 °C, with a step size of $2\theta = 0.02°$. ^{1}H nuclear magnetic resonance (NMR) spectra of digested samples using DMSO-d_6, DCl (35%), and D_2SO_4 were recorded using a 400 MHz Fourier-transform–NMR (FT–NMR) spectrophotometer analyzer at the UNIST Central Research Facilities. The Pd was quantitatively determined using inductively coupled plasma optical emission spectrometry (ICP-OES) analysis. Scanning electron microscopy (SEM) was performed using SU-8220 from Hitachi. High-resolution transmission electron microscopy (HR-TEM) and energy dispersive spectroscopy (EDS) elemental mapping were performed using a JEOL USA JEM-2100F (Cs corrector). X-ray photoelectron spectroscopy (XPS) was conducted using a Thermo Scientific instrument and K-alpha surface analysis. Gas sorption isotherms were measured using a BELSORP-max (BEL Japan, Inc.) adsorption system, employing a standard volumetric technique up to saturation pressure. N_2 (purity of 99.999%) sorption isotherms were monitored at 77 K.

Preparation of MOFs

Preparation of Ni-MOF-74

$[Ni_2(DOBDC)(H_2O)_2]$ (Ni-MOF-74). A mixture of $Ni(NO_3)_2 \cdot 6H_2O$ (198 mg, 0.680 mmol) and 2,5-dihydoxy-1,4-benzenedicarboxylic acid (H_4DOBDC) (95 mg, 0.48 mmol) were dissolved in 10 mL of a mixed solvent (15:1:1, *N*,*N*-dimethylformamide (DMF)/ethanol (EtOH)/H_2O, v/v). The solution was transferred to a 20 mL vial, tightly sealed, and heated at 100°C for 1 d to form a crystalline powder precipitate. The precipitate was harvested and washed several times using DMF and methanol (MeOH) for several days. The activated sample was prepared by vacuum-drying the as-synthesized sample overnight at 150 °C for 1 d.

Preparation of defect-engineered Ni-MOF-74 (DEMOF-I)

$[Ni_2(DOBDC)_{1-x}(n\text{-}aSA)_x(OH)_{2x}(H_2O)_{2+x}]$ (I-n-aSA$_x$). I-n-aSA$_x$ (n= 3 or 5) was also synthesized using a mixed ligand with H_4DOBDC and n-aminosalicylic acid (H_2n-aSA) at 7:3 mole ratios instead of pure H_4DOBDC. I-3-aSA$_{0.18}$ was synthesized using the mole ratios of H_4DOBDC:$H_2$3-aSA at 7:3 and I-5-aSA$_{0.20}$ was synthesized similarly using the mole ratios of H_4DOBDC:$H_2$5-aSA at 7:3.

Post-synthetic ligand modifications of the defect-engineered MOFs

Preparation of $[Ni_2(DOBDC)_{1-x}(n\text{-}pSA)_x(OH)_{2x}(H_2O)_{2+x}]$ (I-n-pSA$_x$), where n-pSA is an n-((pyridin-2-ylmethylene)amino)salicylate. To 10 mL of DMF, 100 mg of I-n-aSA$_x$ and ~5 equivalent amounts of 2-pyridine aldehyde (pa) were added 10 mL DMF and kept at 100 °C for 1 d. The Schiff-base condensation product, I-n-pSA$_x$, containing n-((pyridin-2-ylmethylene)amino) group was afforded, harvested, and washed using DMF and MeOH for several days. The activated samples were prepared by vacuum-drying the as-synthesized products overnight at 150 °C for 1 d.

Post-synthetic metalation of the post-synthetic ligand-modified MOFs

Preparation of $[Ni_2(DOBDC)_{1-x}(n\text{-}pSA)_x \cdot (PdCl_2)_y(OH)_{2x}(H_2O)_{2+x}]$ (I-n-pSA$_x$-Pd$_y$). To 50 mL of acetonitrile (ACN), 100 mg of I-n-pSA$_x$ and $PdCl_2$ (corresponding to approximately 5–10 equivalent amounts of H_2n-pSA in I-n-aSA$_x$) were added and kept at 23 °C for 1 d. The product, I-n-pSA$_x$-Pd$_y$, was harvested and washed for several days using ACN and MeOH. $[Ni_2(DOBDC)_{0.82}(3\text{-}pSA)_{0.18}(PdCl_2)_{0.07}(OH)_{0.36}(H_2O)_{2.18}]$ (I-3-pSA$_{0.18}$-Pd$_{0.07}$) was prepared using 100 mg of I-3-pSA$_{0.18}$ and 89 mg of $PdCl_2$. $[Ni_2(DOBDC)_{0.80}(5\text{-}pSA)_{0.20}(PdCl_2)_{0.05}(OH)_{0.40}(H_2O)_{2.20}]$ (I-5-pSA$_{0.20}$-Pd$_{0.05}$) was prepared using 100 mg of I-5-pSA$_{0.20}$ and 89 mg (0.50 mmol) of $PdCl_2$. The activated samples were prepared by vacuum-drying the as-synthesized products overnight at 150 °C for 1 d.

Preparation of Ni_2(DOBPDC)

[Ni_2(DOBPDC)(H_2O)$_2$]. Ni_2(DOBPDC) was synthesized according to the procedure used in Ni-MOF-74, but 4,4'-dihydroxy-3,3'-biphenyldicarboxyllic acid (H_4DOBPDC) was used instead of H_4DOBDC.

Preparation of defect-engineered Ni_2DOBPDC (DEMOF-II)

[Ni_2(DOBPDC)$_{1-x}$(SA)$_x$(OH)$_{2x}$(H_2O)$_{2+x}$] (II-SA$_x$). The defect-engineered Ni_2(DOBPDC), II-SA$_x$, was synthesized according to the procedure used in the pristine Ni_2(DOBPDC), but instead of pure H_4DOBPDC, H_4DOBPDC and H_2SA were used in a mixture of various mole ratios. II-SA$_{0.10}$ was synthesized using the mole ratio of H_4DOBPDC:H_2SA at 7:3.

[Ni_2(DOBPDC)$_{1-x}$(5-aSA)$_x$(OH)$_{2x}$(H_2O)$_{2+x}$] (II-5-aSA$_x$). The defect-engineered Ni_2(DOBPDC), II-5-aSA$_x$, was also synthesized using a mixed ligand with H_4DOBPDC and $H_2$5-aSA at various mole ratios instead of pure H_4DOBPDC. II-5-aSA$_{0.05}$ and II-5-aSA$_{0.17}$ were synthesized using the mole ratio of H_4DOBPDC:$H_2$5-aSA at 7:3 and 5:5, respectively.

Post-synthetic ligand modifications of the defect-engineered MOFs (DEMOFs)

Preparation of [Ni_2(DOBPDC)$_{0.83}$(5-pSA)$_{0.17}$(OH)$_{0.34}$(H_2O)$_{2.17}$] (II-5-pSA$_{0.17}$). II-5-pSA$_{0.17}$ was synthesized according to the procedure used for I-5-pSA$_x$, but II-5-aSA$_{0.17}$ was used instead of I-5-aSA$_x$. To 10 mL of DMF, 150 mg of II-5-aSA$_{0.17}$ and ~5 equivalent amounts of pa (corresponding to ~5 equivalent amounts of 5-aSA in II-5-aSA$_{0.17}$) were added and kept at 100 °C for 1 d. The Schiff-base condensation product, II-5-pSA$_{0.17}$, containing a 5-((pyridin-2-ylmethylene)amino) group was afforded, harvested, and washed for several days using DMF and MeOH. The activated samples were prepared by vacuum-drying the as-synthesized products overnight at 150 °C.

Post-synthetic metalation of covalently modified DEMOFs

Preparation of [Ni_2(DOBPDC)$_{0.83}$(5-pSA)$_{0.17}$($PdCl_2$)$_{0.06}$(OH)$_{0.34}$(H_2O)$_{2.17}$] (II-5-pSA$_{0.17}$-Pd$_{0.06}$). To 50 mL of ACN, 100 mg of II-5-pSA$_{0.17}$ and 89 mg (0.5 mmol) of $PdCl_2$ were added and kept at 23 °C for 1 d. The product, II-5-pSA$_{0.17}$-Pd$_{0.06}$, was harvested and washed for several days using ACN and MeOH. The activated samples were prepared by vacuum-drying the as-synthesized products overnight at 150 °C.

Preparation of Pd complex, Pd-5-pSA

Pd-5-pSA. $H_2$5-pSA was synthesized according to a previously reported procedure.[25] A mixture of 5-aminosalicylic acid (1.53g, 10.0 mmol), 2-pyridinecarboxaldehyde (1.0 mL, 10 mmol), and triethylamine (1.0 mL, 10 mmol) was added to 50 mL of ethanol (EtOH) in a vial. The mixture was stirred at 50 °C for 4 h to give a yellow precipitate, which was filtered and washed with EtOH, and 5-((pyridine-2-yl)methyleneamino)-2-hydroxybenzoic acid ($H_2$5-pSA) was obtained. A mixture of $H_2$5-pSA (36 mg, 0.15 mmol) and $PdCl_2$ (89 mg, 0.50 mmol) was added to 50 mL of acetonitrile and kept at 23 °C for 1 d. The product Pd-5-pSA was filtered, washed with acetonitrile, and vacuum-dried at 80 °C for 1 d.

Preparation of 9,9'-(5-bromo-1,3-phenylene)bis(3,6-di-*tert*-butyl-9H-carbazole)

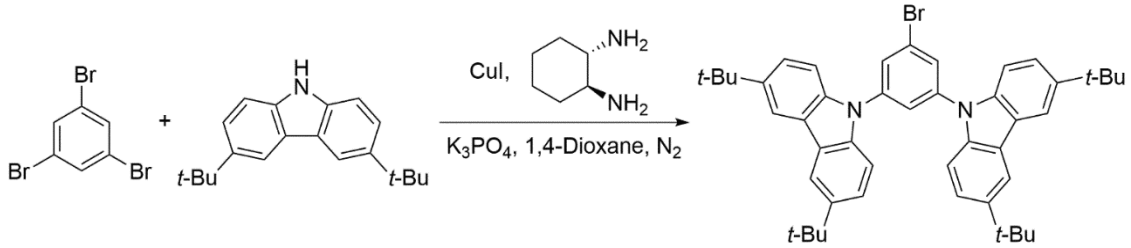

A two-neck flask was charged with 1,3,5-tribromobenzene (628 mg, 2 mmol), 3,6-di-*tert*-butyl-9H-carbazole (1.23 g, 2.2 equiv.), copper(I) iodide (38 mg, 10 mol%), and K_3PO_4 (1.72 g, 4 equiv.). The flask was purged with N_2; (±)-*trans*-1,2-diaminocyclohexane (480 μL, 2 equiv.) and 1,4-dioxane (24 mL) were added to the mixture. The mixture was stirred at 110 °C for 19 h under an N_2 atmosphere. After 19 h, the organic solvent was evaporated under reduced pressure. The residue was dissolved with EtOAc (20 mL); the organic solution was washed with water (20 mL) and brine (20 mL) and dried using $MgSO_4$. The organic layer was filtered and evaporated. The mixture was separated by silica gel column chromatography (EtOAc: n-Hexane = 1: 30), and the crude product was collected and separated by silica gel column chromatography (DCM: n-Hexane = 1: 10). The desired colorless solid, 9,9'-(5-bromo-1,3-phenylene)bis(3,6-di-*tert*-butyl-9H-carbazole) (231 mg, 16%), was obtained. The $_1$H NMR spectrum sufficiently corresponded with the reference data.[26] 9,9'-(5-bromo-1,3-phenylene)bis(3,6-di-*tert*-butyl-9H-carbazole): ^{1}H NMR ($CDCl_3$, 500MHz, ppm.): δ 8.15 (4H, d, J=1.2 Hz), 7.81 (2H, d, J=1.75 Hz), 7.78 (1H, t, J=1.75 Hz), 7.5 (8H, m), 1.48 (36H, s); ^{13}C NMR ($CDCl_3$, 125 MHz, ppm): δ 143.7, 140.8, 138.6, 127.6, 124.0, 123.9, 123.8, 122.9, 116.5, 109.1, 34.8, 32.0.

Suzuki–Miyaura cross-coupling reactions

Catalysis. A mixture of 0.20 mmol of aryl bromide (aryl bromide used: bromobenzene (31 mg), 2-bromoaniline (34 mg), 3-bromoaniline (34 mg), 4-bromoaniline (34 mg), 4-bromotoluene (34 mg), 1-bromonaphthalene (41 mg), or 9-bromoanthracene (51 mg)), two equivalent amounts of phenylboric acid (49 mg), and three equivalent amounts of K_2CO_3 (83 mg) was added in 1 mL of toluene-d_8 in a 5 mL vial. Afterward, the catalyst (catalyst used: **I-3-pSA$_{0.18}$-Pd$_{0.07}$** (30 mg, 2.0 mol% of Pd), **I-5-pSA$_{0.20}$-Pd$_{0.05}$** (30 mg, 1.3 mol% of Pd), **II-5-pSA$_{0.17}$-Pd$_{0.06}$** (45 mg, 2.3 mol% of Pd), Pd-5-pSA (1.1 mg, 1.3 mol % of Pd), and $PdCl_2$ (0.5 mg, 1.3 mol% of Pd) was added into the solution. The vial was incubated at 100 °C for 1 d, followed by centrifugation to separate the solids from the solution. The supernatant was analyzed by ^{1}H NMR spectroscopy.

Recycling test. The catalyst, **I-5-pSA$_{0.20}$-Pd$_{0.05}$**, was isolated from the solution by centrifugation. The collected catalyst was washed using toluene, H_2O, and MeOH through vacuum filtration. The catalyst was vacuum-dried at 150 °C for 1 d and reused for the recycling experiment.

Leaching test. The catalyst**, I-5-pSA$_{0.20}$-Pd$_{0.05}$**, was separated by centrifugation from the hot solution after the reaction was run for 1 h. The filtrate was transferred to a new vial in the absence of a solid catalyst, and the reaction was continued for an additional 23 h under the same reaction conditions. No further increase in the conversion of bromaniline was observed, which indicates that the catalytic active sites for the Suzuki-Miyaura cross-coupling reaction are contained within the solid catalyst.

3.3 Results and Discussions

Post-synthetic modification of DEMOF-1

The amino group on **I-5-aSA$_{0.20}$** can be covalently modified through a Schiff-base condensation reaction. The reaction of **I-5-aSA$_{0.20}$** with 2-formyl-pyridine produced **I-5-pSA$_{0.20}$** containing a 5-((pyridin-2-ylmethylene)amino) group (**Figure 3.2a**). The Pd-incorporated DEMOF-I, **I-5-pSA$_{0.20}$-Pd$_{0.05}$**, can be obtained through post-synthetic metalation.[27] The Pd-incorporated MOFs preserved their crystallinity after the entire PSM procedure (**Figure 3.3**). TEM and EDS showed that the Pd atoms were considerably dispersed in **I-5-pSA$_{0.20}$-Pd$_{0.05}$** (**Figures 3.4a–c**). **I-3-pSA$_{0.18}$** and **I-3-pSA$_{0.18}$-Pd$_{0.07}$** can also be obtained by the same procedure using **I-3-aSA$_{0.18}$** (**Figures 3.2b**, **3.5**, and **3.6**). XPS data support the presence of Pd(II) ions in **I-3-pSA$_{0.18}$-Pd$_{0.07}$** (**Figure 3.7**).

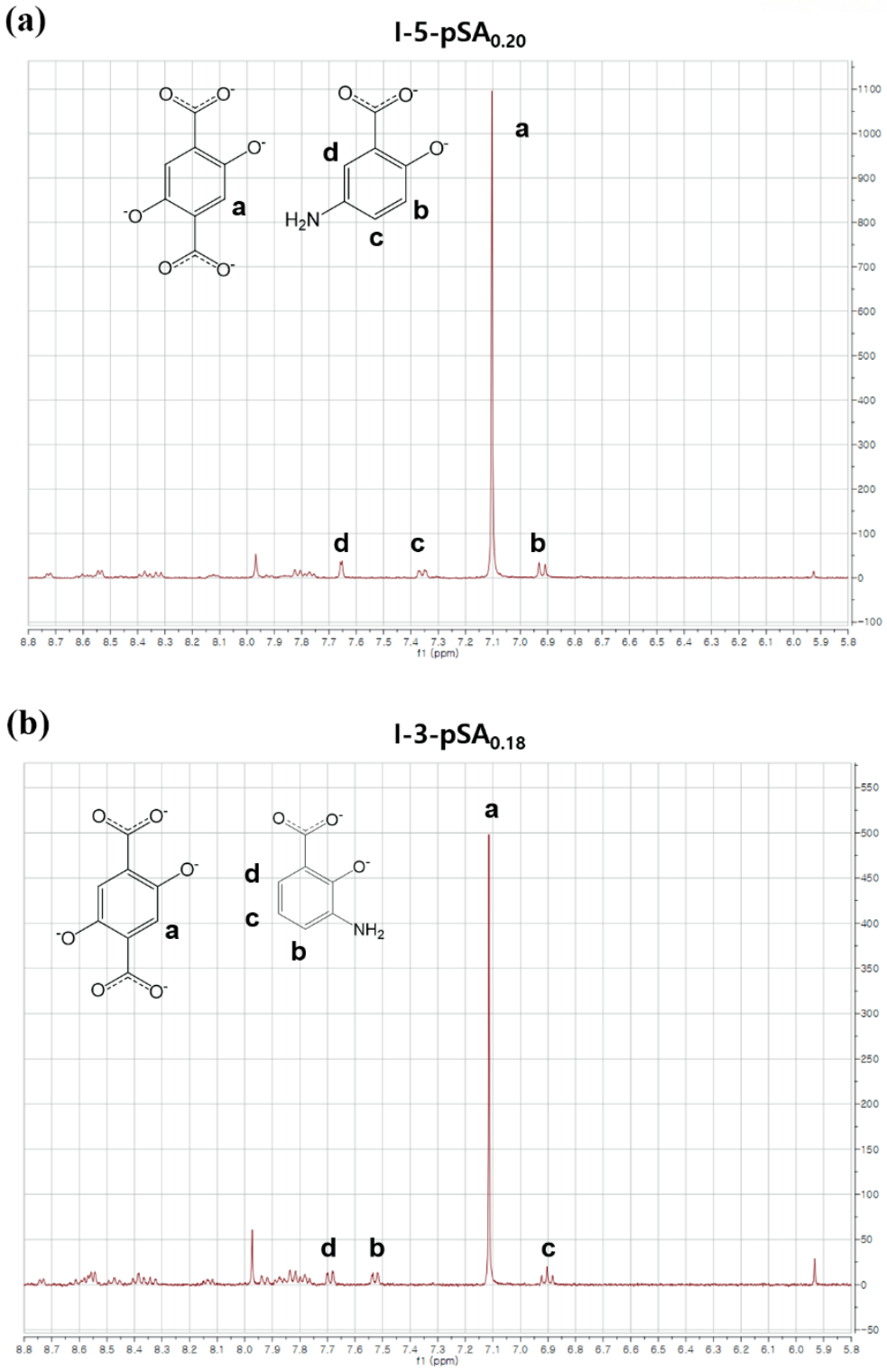

Figure 3.2. ^{1}H NMR spectra of (a) **I-5-pSA$_{0.20}$** and (b) **I-3-pSA$_{0.18}$**. The amount of covalently modified aminosalicylate by pyridine aldehyde in the DEMOF-I cannot be quantitatively analyzed because the Schiff-base condensation product is decomposed to several unidentified compounds by sulphuric acid in DCl/D_2SO_4/DMSO mixed solvent used for the digestion of DEMOF-I and as an NMR solvent.

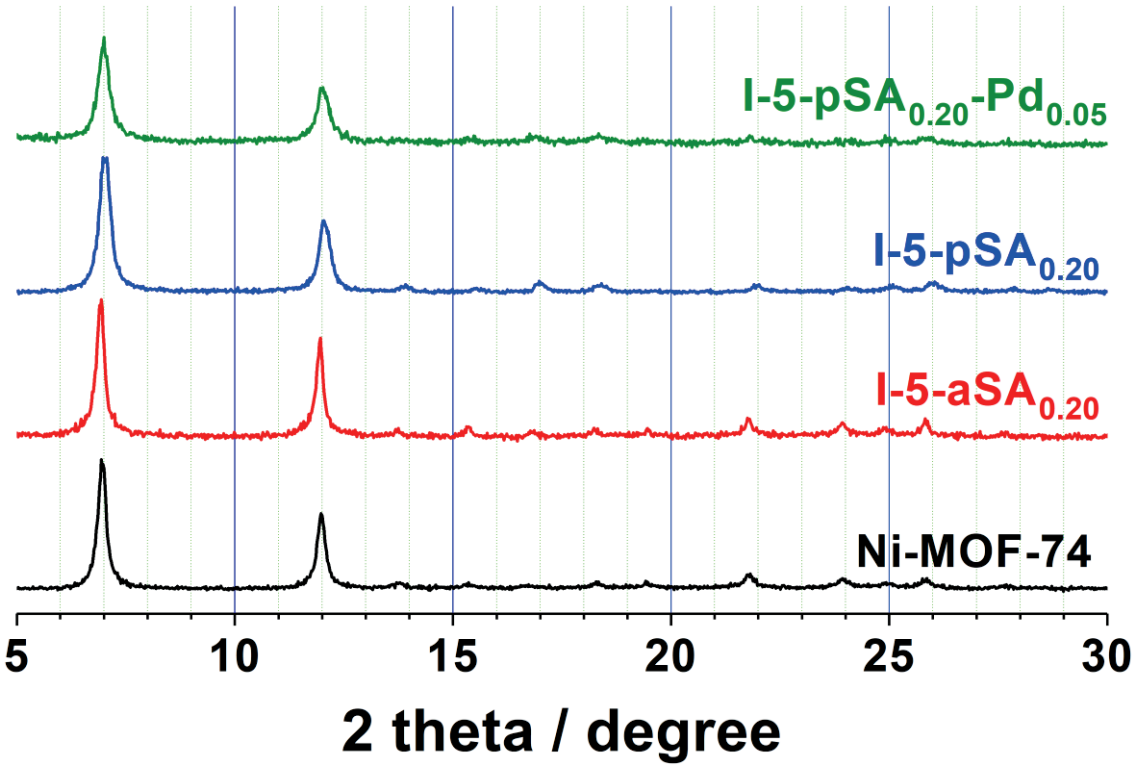

Figure 3.3. PXRD patterns of **I-5-aSA$_{0.20}$**, **I-5-pSA$_{0.20}$** and **I-5-pSA$_{0.20}$-Pd$_{0.05}$**.

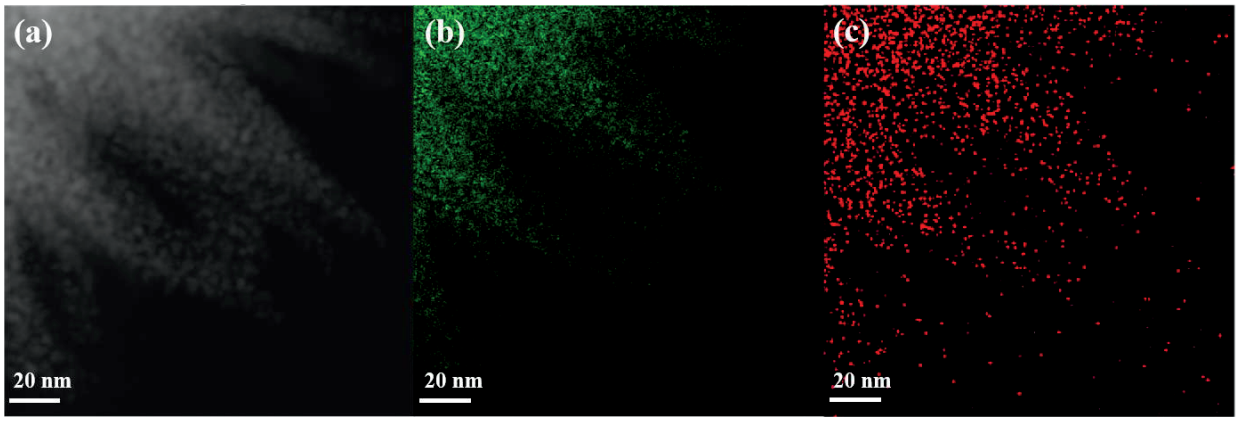

Figure 3.4. TEM image of **I-5-pSA$_{0.20}$-Pd$_{0.05}$**. EDS mappings of (d) Ni (green) and (e) Pd (red) overlaid on the TEM image of **I-5-pSA$_{0.20}$-Pd$_{0.05}$**.

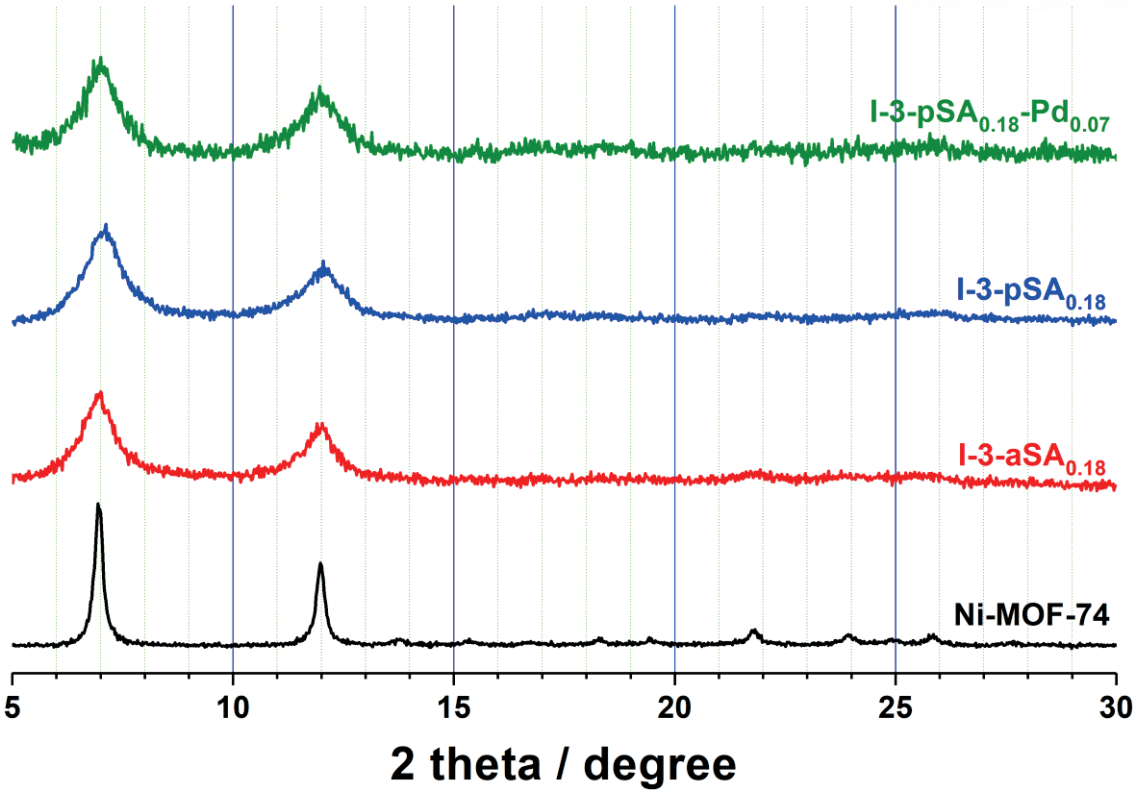

Figure 3.5. PXRD patterns of **I-3-aSA$_{0.18}$**, **I-3-pSA$_{0.18}$** and **I-3-pSA$_{0.18}$-Pd$_{0.07}$**.

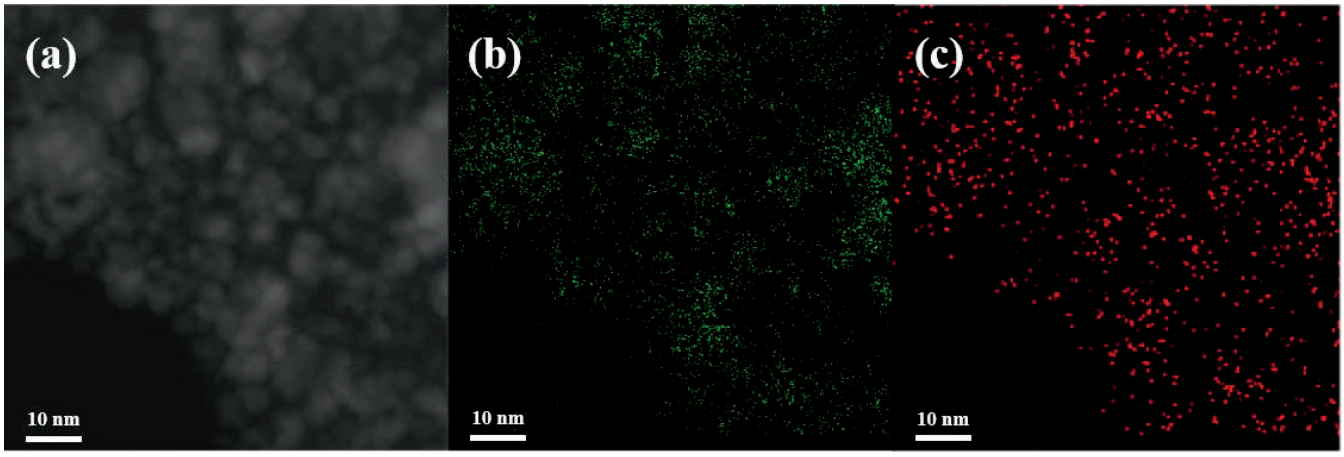

Figure 3.6. TEM image of **I-3-pSA$_{0.18}$-Pd$_{0.07}$**. EDS mappings of (d) Ni (green) and (e) Pd (red) overlaid on the TEM image of **I-3-pSA$_{0.18}$-Pd$_{0.07}$**.

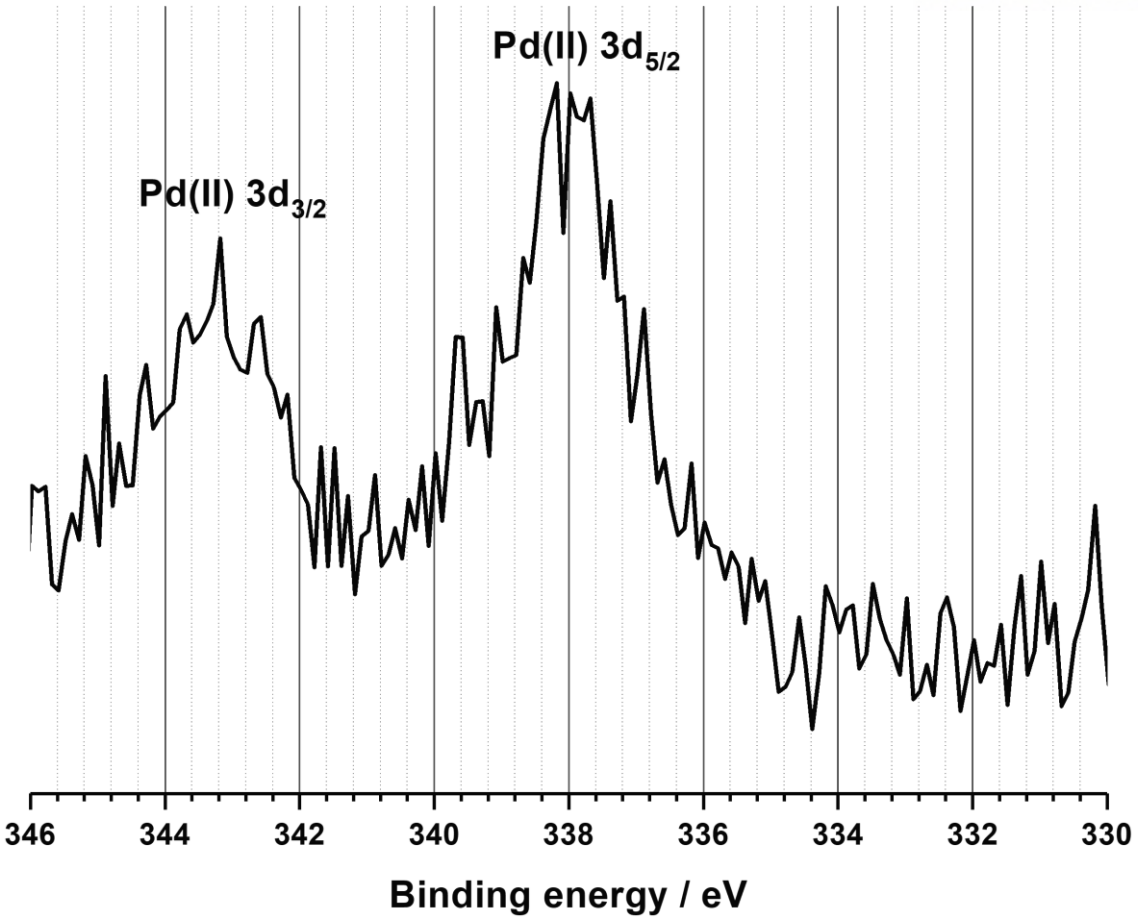

Figure 3.7. XPS spectrum of **I-3-pSA$_{0.18}$-Pd$_{0.07}$** showing Pd^{II} 3d region.

Porosity of modified DEMOFs

The covalent PSM of the amine-tagged DEMOF-I and subsequent metalation of the framework slightly reduced the pore volume of the corresponding MOF (**Figures 3.8a, 3.9a** and **Table 3.1**). The doping of n-aSA led to the significant broadening of the pore size distribution of the MOFs (**Figures 3.8b and 3.9b**), suggesting that the enlargement and reduction of the local pore dimension occurred simultaneously around the defect sites. More interestingly, the covalent PSM had a different effect on the pore size distributions of the modified DEMOFs. The functionalization of both amine-substituted SAs afforded a narrow pore size distribution of the MOFs. Conversely, while the functionalization of the 3-aSA residue mainly reduced the size of the relatively large pore dimension, the functionalization of the 5-aSA residue predominantly reduced the size of the relatively small pore dimension. Thus, MOFs with different average pore dimensions were produced. The average pore dimension of **I-3-pSA$_{0.18}$-Pd$_{0.07}$** (~10 Å) and **I-5-pSA$_{0.20}$-Pd$_{0.05}$** (~12 Å) is slightly smaller and larger than that of the pristine Ni-MOF-74 (~11 Å), respectively.

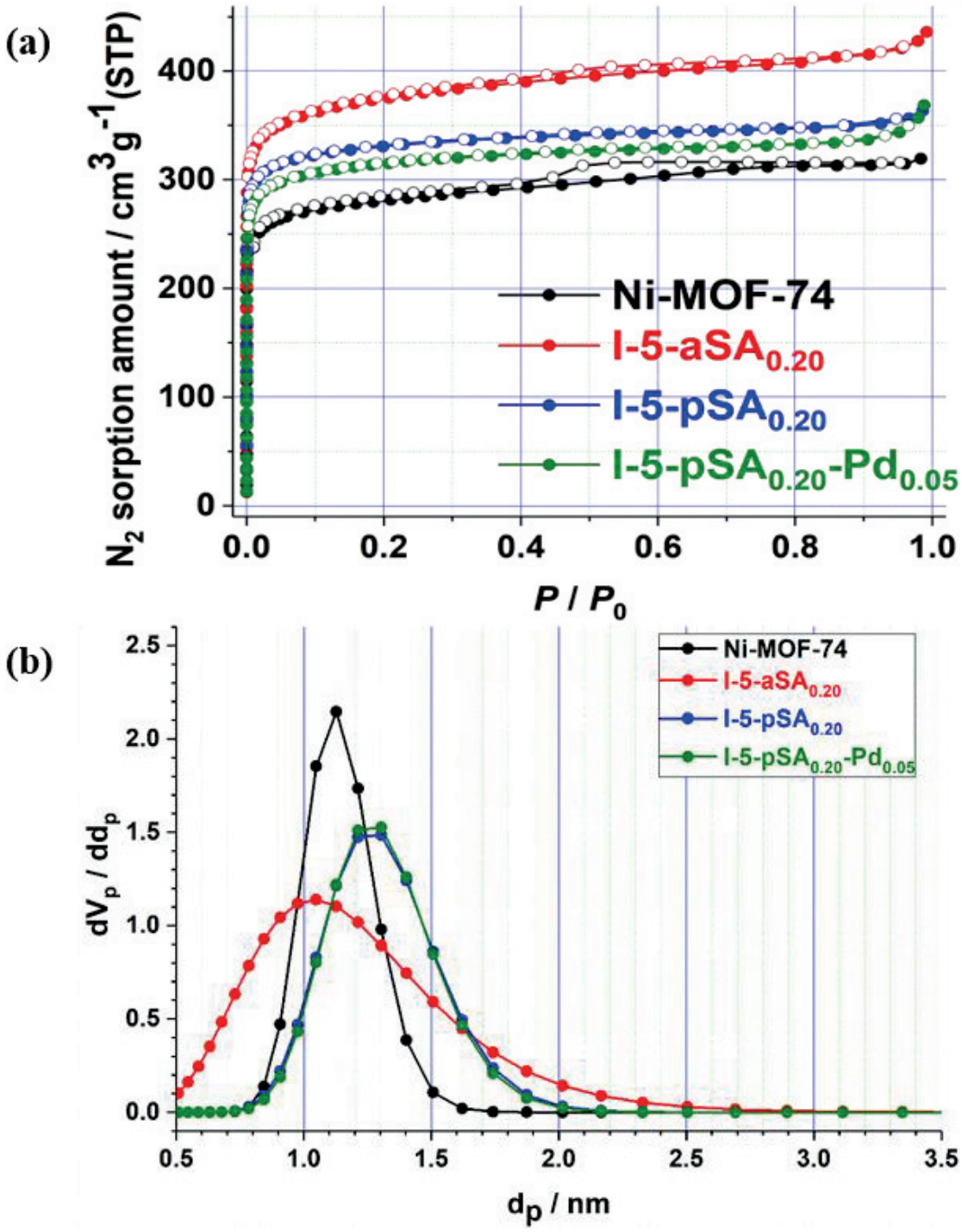

Figure 3.8. (a) N_2 sorption isotherms of **I-5-aSA$_{0.20}$**, **I-5-pSA$_{0.20}$** and **I-5-pSA$_{0.20}$-Pd$_{0.05}$**. (b) NLDFT pore size distributions of **I-5-aSA$_{0.20}$**, **I-5-pSA$_{0.20}$,** and **I-5-pSA$_{0.20}$-Pd$_{0.05}$.**

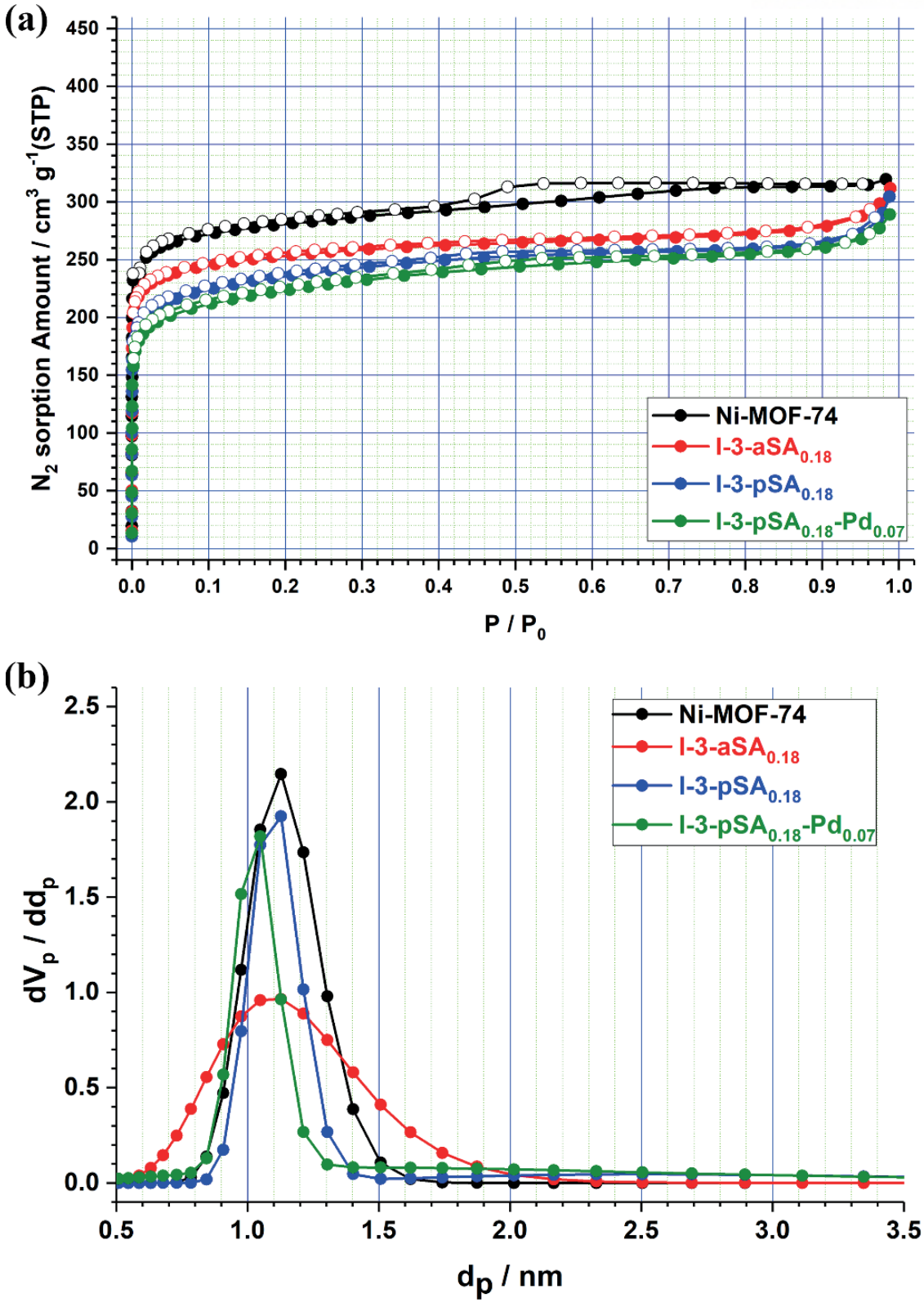

Figure 3.9. (a) N_2 sorption isotherms of **I-3-aSA$_{0.18}$**, **I-3-pSA$_{0.18}$** and **I-3-pSA$_{0.18}$-Pd$_{0.07}$** at 77 K. (b) NLDFT pore size distributions of **I-3-aSA$_{0.18}$**, **I-3-pSA$_{0.18}$**, and **I-3-pSA$_{0.18}$-Pd$_{0.07}$**.

DEMOF-II

There are no reports of the covalent modifications of DOBPDC in Ni_2(DOBPDC), an extended analog of MOF-74, which contains larger pore dimensions than MOF-74, can provide a more efficient diffusion of a substrate or diffuse a larger substrate into the framework than MOF-74.[14, 28–30] The same synthetic protocol was applied to the synthesis of DEMOF-II to determine whether the synthetic strategy was valid for the MOF-74 analog. Following the same procedure used for the preparations of **I-n-aSA$_x$** (**Figures 3.10** and **3.11**), the amine-tagged DEMOF-II, denoted as **II-SA$_{0.10}$**, **II-5-aSA$_{0.05}$**, and **II-5-aSA$_{0.17}$**, depending on the incorporated fragments, were successfully synthesized using H_4DOBPDC. Additionally, the covalently modified DEMOF-II, **II-5-pSA$_{0.17}$** and **II-5-pSA$_{0.17}$-Pd$_{0.06}$**, were prepared according to the same covalent PSM procedure used for the preparation of **I-5-pSA$_{20}$** and **I-5-pSA$_{0.20}$-Pd$_{0.05}$**. The pore volume of **II-5-aSA$_{0.17}$** was significantly reduced compared to that of pristine Ni_2(DOBPDC) (**Figure 3.12a** and **Table 3.1**). The reduced porosity of the amine-tagged DEMOF-II might be related to the reduced crystallinity due to the increased number of defect sites in the crystals. The presence of n-aSA in the framework altered the average pore dimension and pore size distribution of the MOFs. The amine-tagged DEMOF-II had an average pore dimension of 17 Å, which is approximately 4 Å smaller than that of the pristine Ni_2(DOBPDC) (**Figure 3.12b**). The pore size distribution of the amine-tagged DEMOF-II became wider and shifted to the direction of a relatively small dimension. This indicates that the doping of n-aSA reduces pore dimensions around defect sites. Subsequent functionalization and Pd metalation slightly reduced the pore volume and pore dimensions of the functionalized and Pd-incorporated DEMOF-II, **II-5-pSA$_{0.17}$** and **II-5-pSA$_{0.17}$-Pd$_{0.06}$**.

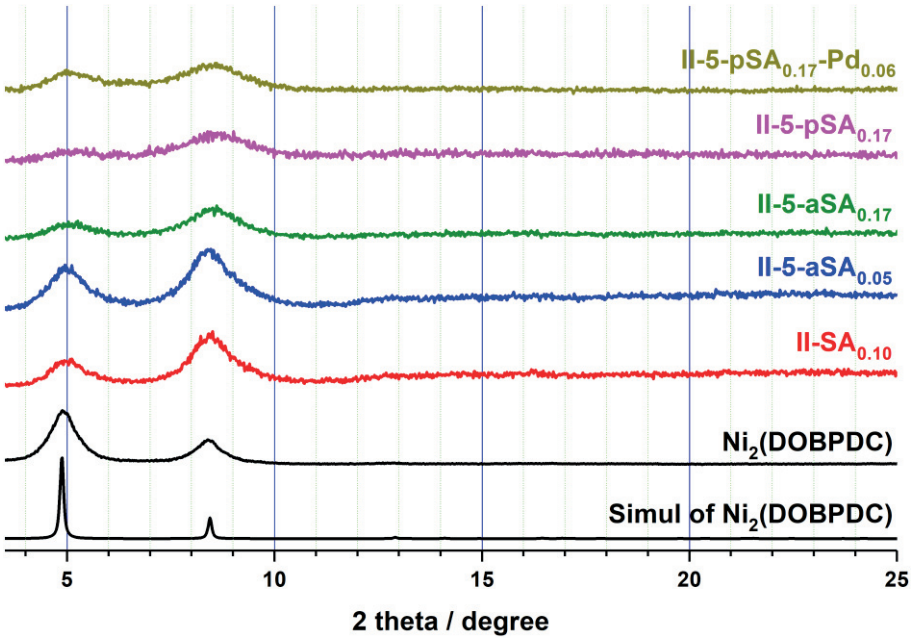

Figure 3.10. PXRD patterns of the pristine Ni_2(DOBPDC), **II-SA$_{0.10}$**, **II-5-aSA$_{0.05}$**, **II-5-aSA$_{0.17}$**, **II-5-pSA$_{0.17}$**, and **II-5-pSA$_{0.17}$-Pd$_{0.06}$**.

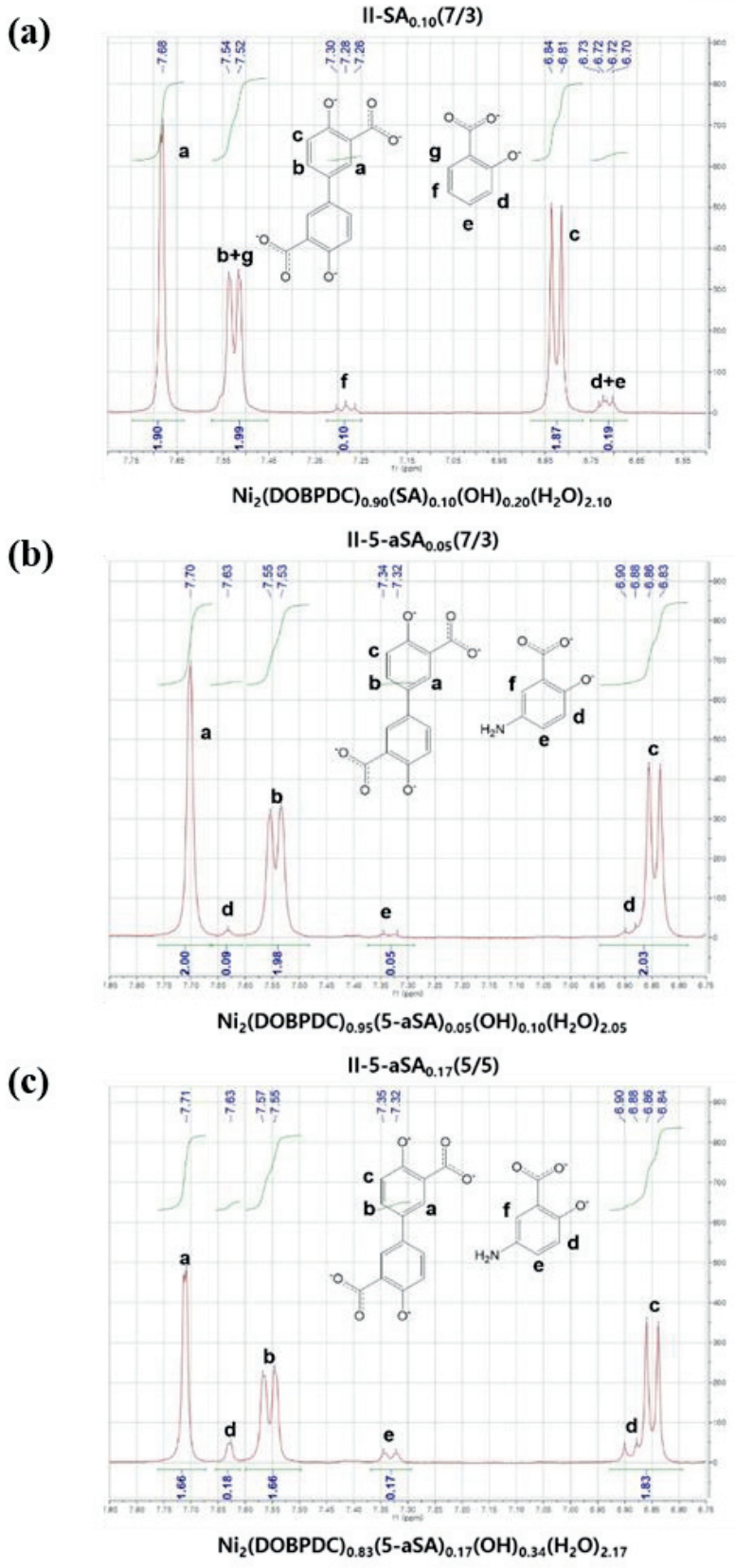

Figure 3.11. ^{1}H NMR spectrum of (a) **II-SA$_{0.10}$(7/3)**, (b) **II-5-aSA$_{0.05}$(7/3),** and (c) **II-5-aSA$_{0.17}$(5/5)**.

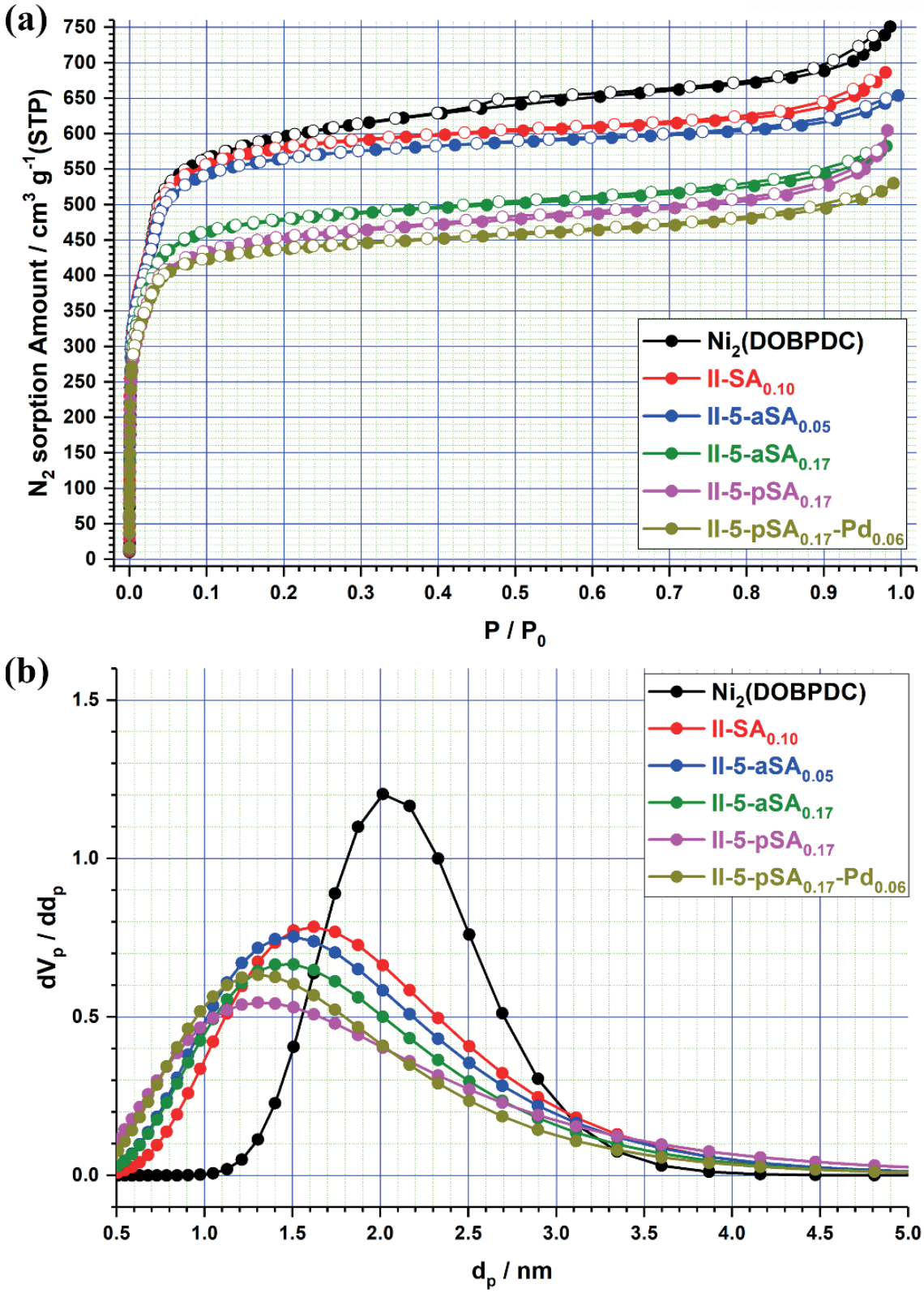

Figure 3.12. (a) N_2 sorption isotherms of the pristine Ni_2(DOBPDC), **II-SA$_{0.10}$, II-5-aSA$_{0.05}$, II-5-aSA$_{0.17}$, II-5-pSA$_{0.17}$,** and **II-5-pSA$_{0.17}$-Pd$_{0.06}$.** (b) NLDFT pore size distributions of the pristine Ni_2(DOBPDC), **II-SA$_{0.10}$, II-5-aSA$_{0.05}$, II-5-aSA$_{0.17}$, II-5-pSA$_{0.17}$,** and **II-5-pSA$_{0.17}$-Pd$_{0.06}$.**

Table 3.1. BET surface areas and pore volumes of Ni-MOF-74, DEMOF-I, Ni_2(DOBPDC), and DEMOF-II.

Sample	BET / $m^2\ g^{-1}$	Pore volume / $cm^3\ g^{-1}$
Ni-MOF-74	1085	0.494
I-3-aSA$_{0.18}$	981	0.482
I-3-pSA$_{0.18}$	874	0.471
I-3-pSA$_{0.46}$-Pd$_{0.07}$	824	0.447
I-5-aSA$_{0.20}$	1428	0.673
I-5-pSA$_{0.20}$	1280	0.563
I-5-pSA$_{0.20}$-Pd$_{0.05}$	1282	0.556
Ni_2(DOBPDC)	2265	1.161
II-SA$_{0.10}$	2135	1.061
II-5-aSA$_{0.05}$	2115	1.004
II-5-aSA$_{0.17}$	1815	0.901
II-5-pSA$_{0.17}$	1749	0.935
II-5-pSA$_{0.17}$-Pd$_{0.06}$	1656	0.819

Suzuki-Miyaura reaction

Since the Pd(II)-incorporated DEMOFs have a catalytic center in the framework, we performed the Suzuki–Miyaura cross-coupling reaction, one of the representative Pd-catalyzed reactions between aryl halides and aryl boronic acids,[31–33] to evaluate the catalytic activities of the Pd(II)-incorporated DEMOFs. As a model reaction, 4-bromoaniline (substrate 1) and phenylboronic acid were selected as the substrates to form 4-aminobiphenyl (**Table 3.2**). While the pristine Ni-MOF-74, **I-5-aSA$_{0.20}$ and I-5-pSA$_{0.20}$**, showed no catalytic activity (entry 1), **I-5-pSA$_{0.20}$-Pd$_{0.05}$** afforded a 99% yield of the cross-coupled product, 4-aminobiphenyl (entry 2). Interestingly, **I-5-pSA$_{0.20}$-Pd$_{0.05}$** exhibited superior catalytic activity compared to $PdCl_2$, a commercially available homogeneous catalyst, under the same reaction conditions. Additionally, the catalytic activity of **I-5-pSA$_{0.20}$-Pd$_{0.05}$** was equivalent to that of **Pd-5-pSA** (entry 5), a homogeneous model catalyst, whose structure imitates the catalytic site **of I-5-pSA$_{0.20}$-Pd$_{0.05}$**. The catalytic activities of **I-5-pSA$_{0.20}$-Pd$_{0.05}$** and **I-3-pSA$_{0.18}$-Pd$_{0.07}$** were also examined for the C–C coupling reaction of phenylboronic acid with various aryl bromides (**Table 3.3**). Both catalysts were highly efficient for the reactions. The yields ranged from 72% to 99%, depending on the substrate.

It is well known that the heterogeneous catalysts derived from MOFs can utilize the catalytic sites located at the outer and inner pore surface of the MOFs.[34,35] To elucidate the locations of active catalytic sites in the DEMOF-74 catalysts, we performed Suzuki–Miyaura coupling reactions of phenylboronic acid with aryl bromides in variable molecular dimensions. The C–C coupling reactions of the smallest substrate 4-bromoaniline were quantitative (entries 2 and 3), except for **II-5-pSA$_{0.17}$-Pd$_{0.06}$** (entry 4), which contained the largest pore dimension. The relatively low yield can be attributed to the low density of active catalytic centers in **II-5-pSA$_{0.17}$-Pd$_{0.06}$** compared to the other catalysts investigated. For 1-bromo-3,5-diphenylbenzene (substrate 2), where the second-largest minimum dimension (MIN-2, 10.8 Å) is similar to the pore dimension of **I-3-pSA$_{0.18}$-Pd$_{0.07}$**, the yields ranged from 80% to 88% for the same heterogeneous catalysts (entries 7, 9, and 11). These yields contrast with the completion of the reaction under the homogenous catalyst, **Pd-5-pSA** (entry 13).

The size selectivity of the catalysts is sufficiently demonstrated in the reaction of 9,9'-(5-bromo-1,3-phenylene)bis(3,6-di-*tert*-butyl-9H-carbazole (substrate 3). The molecular dimension of substrate 3 (MIN-2, 13.5 Å) is comparable to the pore dimension of **I-5-pSA$_{0.20}$-Pd$_{0.05}$** and slightly larger than that of **I-3-pSA$_{0.18}$-Pd$_{0.07}$**. Additionally, the MIN-2 of the C–C coupled product was estimated to be 17.4 Å, which is considerably larger than the pore dimensions of both catalysts. As expected, we observed drastically reduced catalytic activities, 30% yield for **I-5-pSA$_{0.20}$-Pd$_{0.05}$** (entry 8) and 19% yield for **I-3-pSA$_{0.18}$-Pd$_{0.07}$** (entry 10). The C–C coupling reactions were expected to occur mainly at the catalytic sites located on the outer surface of the MOFs. Meanwhile, the yield of the same reaction with **II-5-pSA$_{0.17}$-Pd$_{0.06}$**, 53%, was significantly enhanced (entry 12) because the catalytic sites at the outer surface and inner pore surface of **II-5-pSA$_{0.17}$-Pd$_{0.06}$** with an average pore dimension of 17 Å were more accessible to the substrate.

Table 3.2. Pd-Catalyzed Suruki-Miyaura cross-coupling reactions.

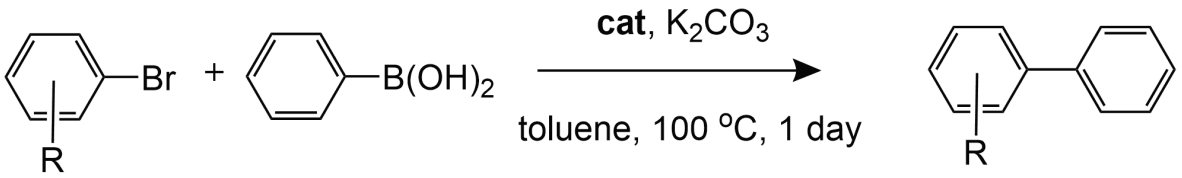

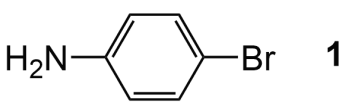

1

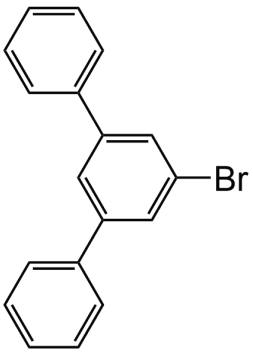

2

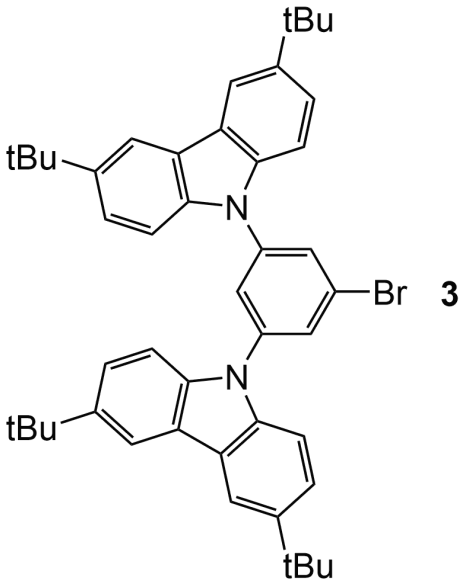

3

Entry	Catalyst[a]	Substrate	% Yield[b]
1	**I-5-pSA$_{0.20}$**	**1**	0
2	**I-5-pSA$_{0.20}$-Pd$_{0.05}$**		99
3	**I-3-pSA$_{0.18}$-Pd$_{0.07}$**[a]		99
4	**II-5-pSA$_{0.17}$-Pd$_{0.06}$**[a]		71
5	**Pd-5-pSA**		99
6	$PdCl_2$		60
7	**I-5-pSA$_{0.20}$-Pd$_{0.05}$**	**2**	80
8		**3**	30
9	**I-3-pSA$_{0.18}$-Pd$_{0.07}$**[a]	**2**	88
10		**3**	19
11	**II-5-pSA$_{0.17}$-Pd$_{0.06}$**[a]	**2**	80
12		**3**	53
13	**Pd-5-pSA**	**2**	99
14		**3**	99

[a] 1.3 mol% of Pd for **I-5-pSA$_{0.20}$-Pd$_{0.05}$**; 2.0 mol% of Pd for **I-3-pSA$_{0.18}$-Pd$_{0.07}$**; 2.3 mol% of Pd for **II-5-pSA$_{0.17}$-Pd$_{0.06}$**; 1.3 mol% of Pd for the other Pd-containing catalysts. [b] Yields were determined using ^{1}H NMR spectroscopy.

Table 3.3. Various substrates used for the Suzuki–Miyaura cross-coupling reaction under the catalysts, **I-3-pSA$_{0.18}$-Pd$_{0.07}$** and **I-5-pSA$_{0.20}$-Pd$_{0.05}$**.

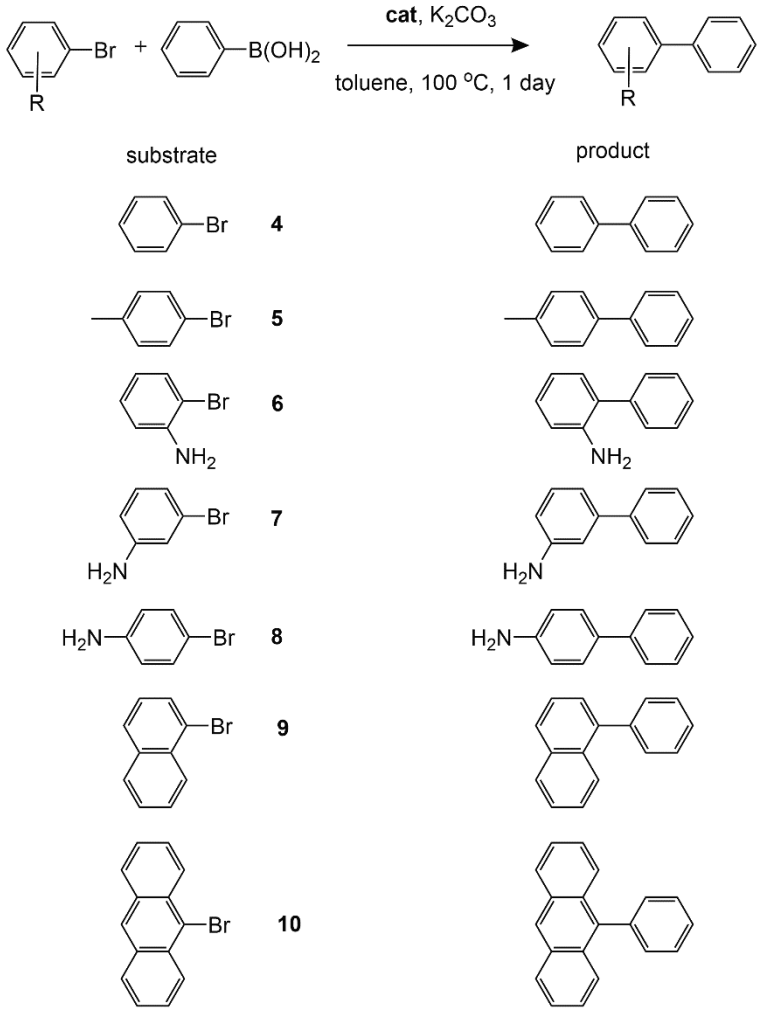

Entry	Substrate	Yield for **I-3-pSA$_{0.18}$-Pd$_{0.07}$**	Yield for **I-5-pSA$_{0.20}$-Pd$_{0.05}$**
15	**4**	81	88
16	**5**	89	83
17	**6**	73	79
18	**7**	99	99
19	**8**	99	99
20	**9**	78	72
21	**10**	99	96

The leaching of metal ions from the active sites during catalysis is a critical issue for metal-incorporated heterogeneous catalysts.[31,36] Therefore, a hot-filtration test was performed using the reaction of **I-5-pSA$_{0.20}$-Pd$_{0.05}$** to determine whether Pd ions were leached during the reaction. After one h of reaction, the catalyst **I-5-pSA$_{0.20}$-Pd$_{0.05}$** was removed from the reaction mixture by hot filtration, and the filtrate was allowed to react for an additional 23 h. The undisturbed C–C coupling reaction was almost complete after 24 h. In contrast, once the catalyst was removed by filtration, the reaction stopped, indicating the absence of Pd ions in the filtrate (**Figure 3.13a**). Inductively coupled plasma optical emission spectrometry (ICP-OES) for Pd content also supported the absence of Pd in the filtrate, where the detected Pd content was below the detection limit of the instrument. The stability and recyclability of heterogeneous catalysts are very important for practical applications. To evaluate the recyclability of the catalyst, **I-5-pSA$_{0.20}$-Pd$_{0.05}$** was recovered from the reaction mixture by centrifugation, and the recovered catalyst was used in the successive run of the Suzuki–Miyaura cross-coupling reaction. No decrease in catalytic activity (> 99% yield) was observed even after the fifth reaction, indicating relatively high stability of the catalyst under the reaction conditions (**Figure 3.13b**). The PXRD characterization of **I-5-pSA$_{0.20}$-Pd$_{0.05}$** after catalysis further demonstrated that the Pd(II)-incorporated DEMOF, **I-5-pSA$_{0.20}$-Pd$_{0.05}$**, retained high crystallinity (**Figure 3.14**).

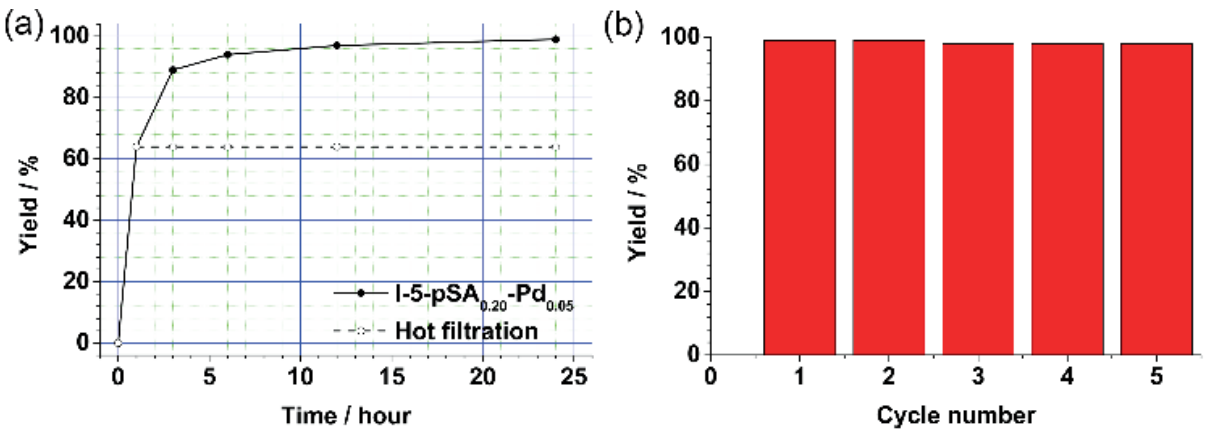

Figure 3.13. (a) Hot filtration and (b) recycling test of **I-5-pSA$_{0.20}$-Pd$_{0.05}$** in the Suzuki–Miyaura cross-coupling reaction.

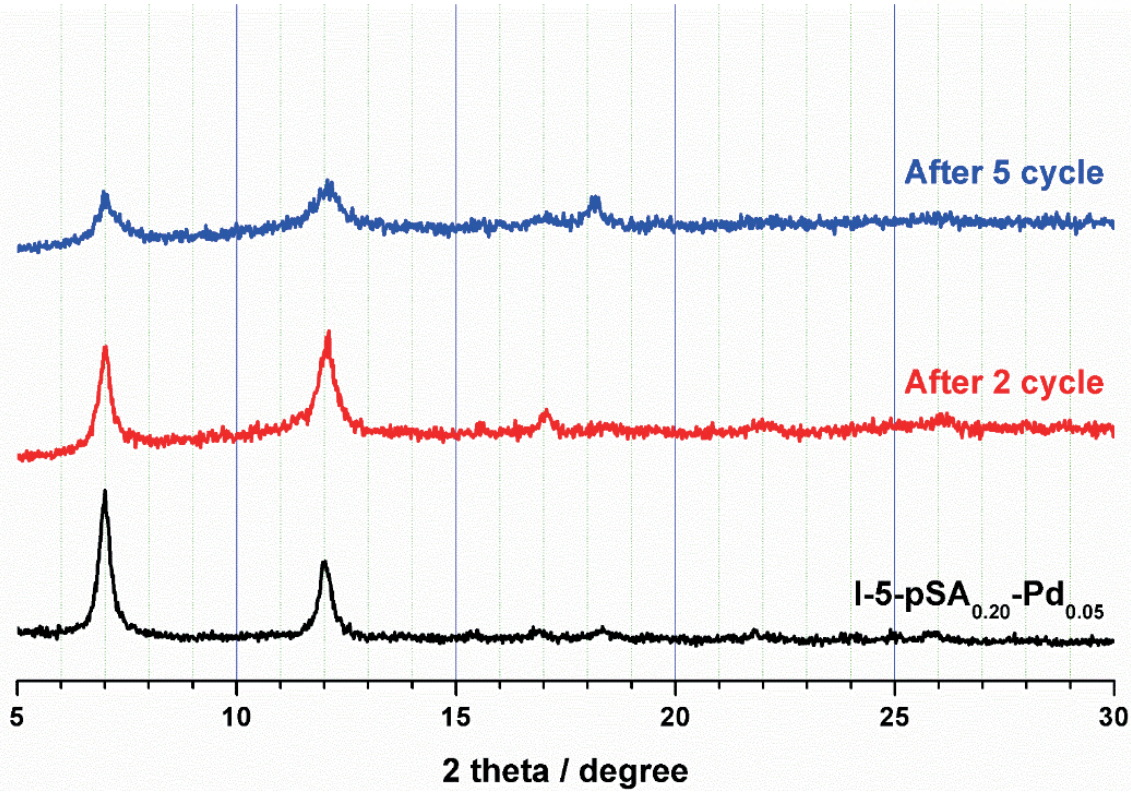

Figure 3.14. PXRD patterns of **I-5-pSA$_{0.20}$-Pd$_{0.05}$** after 2 and 5 cycels of Suzuki–Miyaura cross-coupling reactions.

3.4 Conclusion

In summary, we successfully demonstrated that the synthesis of functionalized DEMOF-I and DEMOF-II derivatives can be achieved by amine-tagged fragment installation. The installation of the fragment into the framework resulted in defective but highly stable porous MOFs. Amine-tagged DEMOFs can be covalently modified with an aldehyde functional group, leading to an iminopyridine functionality, which can be further modified by post-synthetic metalation. The Pd-incorporated DEMOFs showed highly efficient, size-selective, and recyclable heterogeneous catalytic activities for the Suzuki–Miyaura cross-coupling reaction. These results suggest that a combination of fragment installation and subsequent covalent PSM will become an efficient protocol to introduce desired functionality into MOFs, and this approach will provide great opportunities to explore many MOFs in diverse applications.

3.5 References

1. Rosi, N. L.; Kim, J.; Eddaoudi, M.; Chen, B.; Keeffe, M. O.; Yaghi, O. M. Rod Packings and Metal-Organic Frameworks Constructed from Rod-Shaped Secondary Building Units. *J. Am. Chem. Soc*. **2005**, 127, 1504−1518.
2. Caskey, S. R.; Wong-Foy, A. G.; Matzger, A. J. Dramatic Tuning of Carbon Dioxide Uptake via Metal Substitution in a Coordination Polymer with Cylindrical Pores. *J. Am. Chem. Soc*. **2008**, *130*, 10870−10871.
3. Bloch, E. D.; Murray, L. J.; Queen, W. L.; Chavan, S.; Maximoff, S. N.; Bigi, J. P.; Krishna, R.; Peterson, V. K.; Grandjean, F.; Long, G. J.; Smit, B.; Bordiga, S.; Brown, C. M.; Long, J. R. Selective Binding of O_2 over N_2 in a Redox-Active Metal-Organic Framework with Open Iron(II) Coordination Sites. *J. Am. Chem. Soc*. **2011**, *133*, 14814−14822.
4. He, Y.; Krishna, R.; Chen, B. Metal–organic frameworks with potential for energy-efficient adsorptive separation of light hydrocarbons. *Energy Environ Sci*. **2012**, *5*, 9107-9120.
5. Kökçam-Demir, Ü.; Goldman, A.; Esrafili, L.; Gharib, M.; Morsali, A.; Weingart, O.; Janiak, C. Coordinatively unsaturated metal sites (open metal sites) in metal–organic frameworks: design and applications. *Chem. Soc. Rev*. **2020**, *49*, 2751−2798.
6. Xiao, T.; Liu, D. The most advanced synthesis and a wide range of applications of MOF-74 and its derivatives. *Microporous and Mesoporous Mater*. **2019**, 283, 88−103.
7. McKinlay, A. C.; Xiao, B.; Wragg, D. S.; Wheatley, P. S.; Megson, I. L.; Morris, R. E. Exceptional Behavior over the Whole Adsorption-Storage-Delivery Cycle for NO in Porous Metal Organic Frameworks. *J. Am. Chem. Soc*. **2008**, *130*, 10440−10444.
8. Kim, J. Y.; Balderas-Xicohténcatl, R.; Zhang, L.; Kang, S. G.; Hirscher, M.; Oh, H.; Moon, H. R. Exploiting Diffusion Barrier and Chemical Affinity of Metal−Organic Frameworks for Efficient Hydrogen Isotope Separation. *J. Am. Chem. Soc*. **2017**, *139*, 15135−15141.
9. Sarango-Ramírez, M. K.; Lim, D-W.; Kolokolov, D. I.; Khudozhitkov, Al. E.; Stepanov, A. G.; Kitagawa, H. Superprotonic Conductivity in Metal−Organic Framework via Solvent-Free Coordinative Urea Insertion. *J. Am. Chem. Soc*. **2020**, *142*, 6861−6865.
10. Yang, D-A.; Cho, H-Y.; Kim, J.; Yang, S-T.; Ahn, W-S. CO_2 capture and conversion using Mg-MOF-74 prepared by a sonochemical method. *Energy Environ. Sci*. **2012**, *5*, 6465−6473.
11. Wu, D.; Guo, Z.; Yin, X.; Pang, Q.; Tu, B.; Zhang, L.; Wang, Y-G.; Li, Q. Metal–Organic Frameworks as Cathode Materials for Li–O_2 Batteries. *Adv. Mater*. **2014**, *26*, 3258−3262.
12. Valvekens, P.; Vandichel, M.; Waroquier, M.; Speybroeck, V. V.; Vos, D. D. Metal-dioxidoterephthalate MOFs of the MOF-74 type: Microporous basic catalysts with well-defined active sites. *J. Catal*. **2014**, *317*, 1−10.

13. Kim, H.; Sohail, M.; Yim, K.; Park, Y. C.; Chun, D. H.; Kim, H. J.; Han, S. O.; Moon, J-H. Effective CO_2 and CO Separation Using [M_2(DOBDC)] (M = Mg, Co, Ni) with Unsaturated Metal Sites and Excavation of Their Adsorption Sites. *ACS Appl. Mater. Interfaces* **2019**, *11*, 7014−7021.
14. McDonald, T. M.; Lee, W. R.; Mason, J. A.; Wiers, B. M.; Hong, C. S.; Long, J. R. Capture of Carbon Dioxide from Air and Flue Gas in the Alkylamine-Appended Metal−Organic Framework mmen-Mg_2(dobpdc). *J. Am. Chem. Soc*. **2012**, *134*, 7056−7065.
15. Park, J.; Jiang, Q.; Feng, D.; Mao, L.; Zhou, H-C. Size-Controlled Synthesis of Porphyrinic Metal−Organic Framework and Functionalization for Targeted Photodynamic Therapy. *J. Am. Chem. Soc*. **2016**, *138*, 3518−3525.
16. Shearer, G. C.; Chavan, S.; Bordiga, S.; Svelle, S.; Olsbye, U.; Lillerud, K. P. Defect Engineering: Tuning the Porosity and Composition of the Metal−Organic Framework UiO-66 via Modulated Synthesis. *Chem. Mater*. **2016**, *28*, 3749−3761.
17. Park, J.; Wang, Z. U.; Sun, L-B.; Chen, Y-P.; Zhou, H-C. Introduction of Functionalized Mesopores to Metal−Organic Frameworks via Metal−Ligand−Fragment Coassembly. *J. Am. Chem. Soc*. **2012**, *134*, 20110−20116.
18. Fang, Z.; Dürholt, J. P.; Kauer, M.; Zhang, W.; Lochenie, C.; Jee, B.; Albada, B.; Metzler-Nolte, N.; Pöppl, A.; Weber, B.; Muhler, M.; Wang, Y.; Schmid, R.; Fischer, R. A. Structural Complexity in Metal−Organic Frameworks: Simultaneous Modification of Open Metal Sites and Hierarchical Porosity by Systematic Doping with Defective Linkers. *J. Am. Chem. Soc*. **2014**, *136*, 9627−9636.
19. El-Gamel, N. E. A. Generation of Defect-Modulated Metal–Organic Frameworks by Fragmented-Linker Co-Assembly of CPO-27(M) Frameworks. *Eur. J. Inorg. Chem*. **2015**, *8*, 1351−1358.
20. Wu, D.; Yan, W.; Xu, H.; Zhang, E.; Li, Q. Defect engineering of Mn-based MOFs with rod-shaped building units by organic linker fragmentation. *Inorg. Chim. Acta*. **2017**, *460*, 93−98.
21. Villajos, J. A.; Jagorel, N.; Reinsch, S.; Emmerling, F. Increasing Exposed Metal Site Accessibility in a Co-MOF-74 Material With Induced Structure-Defects. *Front. Mater*. **2019**, *6*, 230.
22. Pachfule, P.; Shinde, D.; Majumder, M.; Xu, Q. Fabrication of carbon nanorods and graphene nanoribbons from a metal–organic framework. *Nat. Chem*, **2016**, *8*, 718−724.
23. Wang, Z.; Cohen, S. M. Tandem Modification of Metal–Organic Frameworks by a Postsynthetic Approach. *Angew. Chem.* **2008**, *120*, 4777−4780; *Angew. Chem. Int. Ed*. **2008**, 47, 4699−4702.
24. Yin, Z.; Wan, S.; Yang, J.; Kurmoo, M.; Zeng, M-H. Recent advances in post-synthetic modification of metal–organic frameworks: New types and tandem reactions. *Coord. Chem. Rev*. **2019**, *378*, 500−512.
25. Zhao, Y.-Y.; Zhao, X.-H.; Bing, Y.; Pan, J.-G.; Li, X. Syntheses, Crystal Structures and Electrochemical Activities of Co(II) and Cu(II)-Complexes with 5-Aminosalicylate Derivatives. *J.*

Chem. Crystallogr. **2013**, 43, 568−575.

26. Okamura, N.; Egawa, K.; Maeda, T.; Yagi, S. Control of excimer phosphorescence by steric effects in cyclometalated platinum(II) diketonate complexes bearing peripheral carbazole moieties towards application in non-doped white OLEDs. *New J. Chem*. **2018**, 42, 11583−11592.
27. Doonan, C. J.; Morris, W.; Furukawa, H.; Yaghi, O. M. Isoreticular Metalation of Metal-Organic Frameworks. *J. Am. Chem. Soc*. **2009**, 131, 9492−9493.
28. McDonald, T. M.; Mason, J. A.; Kong, X.; Bloch, E. D.; Gygi, D.; Dani, A.; Crocellà, V.; Giordanino, F.; Odoh, S. O.; Drisdell, W. S.; Vlaisavljevich, B.; Dzubak, A. L.; Poloni, R.; Schnell, S. K.; Planas, N.; Lee, K.; Pascal, T.; Wan, L. F.; Prendergast, D.; Neaton, J. B.; Smit, B.; Kortright, J. B.; Gagliardi, L.; Bordiga, S.; Reimer, J. A.; Long, J. R. Cooperative insertion of CO_2 in diamine appended metal-organic frameworks. *Nature*. **2015**, 519, 303−308.
29. Aubrey, M. L.; Ameloot, R.; Wiers, B. M.; Long, J. R. Metal–organic frameworks as solid magnesium Electrolytes. *Energy Environ. Sci*. **2014**, 7, 667−671.
30. Tay, H. M.; Rawal, A.; Hua, C. S-Mg_2(dobpdc): a metal–organic framework for determining chirality in amino acids. *Chem. Commun*. **2020**, 56, 14829−14832.
31. Li, X.; Zeeland, R. V.; Maligal-Ganesh, R. V.; Pei, Y.; Power, G.; Stanley, L.; Huang, W. Impact of Linker Engineering on the Catalytic Activity of Metal−Organic Frameworks Containing Pd(II)−Bipyridine Complexes. *ACS. Catal*. **2016**, 6, 6324−6328.
32. Fei, H.; Cohen, S. M. A robust, catalytic metal–organic framework with open 2,2'-bipyridine sites. *Chem. Commum*. **2014**, 50, 4810−4812.
33. Xiong, G.; Chen, X-L.; You, L-X.; Ren, B-Y.; Ding, F.; Dragutan, I.; Dragutan, V.; Sun, Y-G. La-Metal-Organic Framework incorporating Fe_3O_4 nanoparticles, post-synthetically modified with Schiff base and Pd. A highly active, magnetically recoverable, recyclable catalyst for C-C cross-couplings at low Pd loadings. *J. Catal*. **2018**, 361, 116−125.
34. Kim, S.; Lee, J.; Jeoung, S.; Moon, H. R.; Kim, M. Surface-Deactivated Core–Shell Metal–Organic Framework by Simple Ligand Exchange for Enhanced Size Discrimination in Aerobic Oxidation of Alcohols. *Chem. Eur. J*. **2020**, 26, 7568−7572.
35. Yang, D.; Gates, B. C. Catalysis by Metal Organic Frameworks: Perspective and Suggestions for Future Research. *ACS Catal*. **2019**, 9, 1779−1798.
36. Hussain, I.; Capricho, J.; Yawer, M. A. Synthesis of Biaryls via Ligand-Free Suzuki–Miyaura Cross-Coupling Reactions: A Review of Homogeneous and Heterogeneous Catalytic Developments. *Adv. Synth. Catal*. **2016**, 358, 3320−3349.

Chapter IV

Fluorescence Sensing of H_2O in D_2O using $H_2BDC\text{-}(OH)_2$@MIL-53(In)-$(OH)_2$

4.1 Introduction

Flexible metal-organic frameworks (MOFs) are extended network structures composed of inorganic nodes and organic linkers with feasible reversible structure transformations when exposed to internal guests (encapsulated solvent and reactants or gas molecules) or external stimuli (temperature, pressure, or light).[1-5] Depending on the functional residues of organic linkers such as amine and hydroxyl groups, MOFs can exhibit different flexibilities and various chemical properties. However, to be utilized in a variety of applications, flexible MOF must withstand significant structural transformation by stimulus.[6,7] To increase framework stability, guests such as polymer and supramolecules were incorporated into the pore to prevent the collapse of framework structure.[8,9]

MIL-53(M) ($[M(BDC)(\mu_2\text{-}OH)]_n$, BDC^{2-} = benzene-1,4-dicarboxylate and M = Al, Fe, Cr, In) consisting of an infinite 1D metal node and an organic linker is one of the most famous flexible MOFs with impressive framework stability. MIL-53 exhibits breathing behaviour by altering the dihedral angle between the inorganic SBU and the linker.[10-16] Linker functionalization (H_2BDC-X, X = NH_2, OH, Br, COOH and $(OH)_2$) not only provides new active sites but also adjusts the flexibility of the framework.[17-21] The encapsulation of additional organic ligands inside the solvent pores is often determined by the choice of solvent used during MOF synthesis. Reactions under polar solvents such as water lead to encapsulation of free ligands inside the solvent pores,[10-12,17-19,22] whereas reactions under less polar solvents such as DMF and DEF do not. [13,17,18,22] To achieve the breathing of MIL-53-X, it is necessary to remove the encapsulated guest molecules in the solvent pores. The encapsulated free ligand can be removed either heating the MOF at high temperature or soaking the MOF in polar solvents such as water and methanol. MIL-53 is well known for its inherent structural stability in a variety of environments and is widely used in applications such as gas adsorption, separation, catalysis, and sensors.[20,21,23,24] In contrast, as-synthesized MIL-53-X prepared in water containing free ligands in solvent pores has not yet been explored.

High purity heavy water (D_2O), an isotopic species of water (H_2O), is used as a neutron moderator and coolant in nuclear reactors,[25] as a solvent during synthesis of deuterated organic compounds[26] and in nuclear magnetic resonance (NMR) spectroscopy.[27] Due to the similar chemical and physical properties of D_2O and H_2O, methods for detecting H_2O impurities in D_2O have been limited to atomic absorption spectroscopy,[28] infrared laser spectroscopy[29] and NMR spectroscopy.[30] However, these methods are expensive, time consuming and inconvenient to measure. Therefore, fluorescence-based sensors that can detect H_2O impurities in D_2O easily and inexpensively are of great interest.[31-35] H_2O impurities in D_2O can be detected through fluorescence of organic chromophores with proton-exchangeable sites such as free hydroxyl residues. When the pKa value of the proton-exchangeable site

properly matches the values of H_2O (pH = 6.4-7.0) and D_2O (pD = 7.5) at 25 °C, the chromophore can show different fluorescence behaviour according to the ratio of H_2O and D_2O.[32,35]

MIL-53(In)-$(OH)_2$ (**MIL-53-H/DMF**) was prepared according to the reported procedure using In^{3+} and 2,5-dihydroxy-1,4-benzenedicarboxylaic acid (H_2BDC-$(OH)_2$) under a mixed solvent of H_2O and DMF.[36] It is reported that **MIL-53-H/DMF** containing a free hydroxyl moiety in its ligand has functional moieties for hydrogen bonding and π-π stacking interactions and is advantageous for detecting nitroaromatics utilizing both interactions. Herein, we report the discovery of the instability of **MIL-53-H/DMF** crystals during the breathing process in water and the fluorescence detection of H_2O impurities in D_2O using a stable MIL-53(In)-$(OH)_2$ (**MIL-53-H**) containing 0.6 equivalent of free ligand (H_2BDC-$(OH)_2$) in the solvent pores. We observed that **MIL-53-H/DMF** crystals do not withstand water-induced breathing. When 40-50 μm-sized crystals are soaked in water, the crystals are split into micron-sized particles, while simultaneously producing nanometer-sized particles dispersed in solution. The two different sized particles show two different fluorescence bands in both H_2O and D_2O, which hinders the ratiometric detection of H_2O impurity in D_2O. To obtain highly stable MIL-53(In)-$(OH)_2$ in water, **MIL-53-H** containing 0.6 equivalents of free ligand in the solvent pores was synthesized using pure water as the synthesis solvent. **MIL-53-H** can detect H_2O impurity in D_2O very efficiently because the fluorescence intensity of **MIL-53-H** varies according to the ratio of H_2O and D_2O. The detection limit is less than 1% H_2O in D_2O, which is much lower than the reported detection limits (**Figure 4.1**).[31]

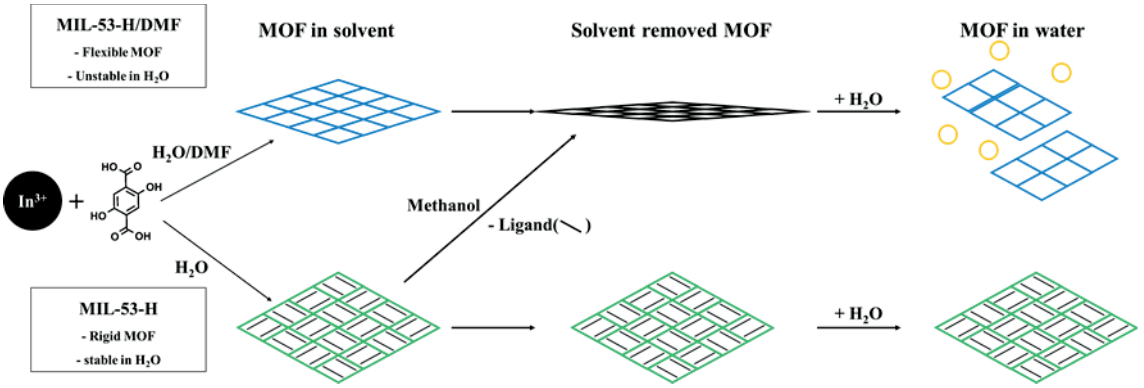

Figure 4.1. The intermediated structure (**MIL-53-H**) including free ligands as water stable MOFs, whereas the thermodynamic structure (**MIL-53-H/DMF**) as an unstable flexible MOF in water.

4.2 Experimental Section

General Procedures

All reagents were purchased from commercial sources and used without further purification. Powder X-ray diffraction (PXRD) data were recorded using a Bruker D2 Phaser automated diffractometer at room temperature, with a step size of $2\theta = 0.02°$. Fourier transform–infrared (FT–IR) spectra were recorded using a NICOLET iS 10 FT–IR spectrophotometer (4000–400 cm^{-1}). Elemental analyses (EA) were conducted using a Flash 2000 elemental analyzer. ^1H nuclear magnetic resonance (NMR) spectra of samples using CD_3OD were recorded using a 400 MHz Fourier-transform–NMR (FT–NMR) spectrophotometer analyzer at the UNIST Central Research Facilities. Thermogravimetric analyses (TGA) were performed using a Q-600 series instrument from TA Instruments at heating rate of 5 ºC min^{-1} under flowing air gas. Scanning electron microscopy (SEM) was performed using SU-8220 from Hitachi. High-resolution transmission electron microscopy (HR-TEM) and energy dispersive spectroscopy (EDS) elemental mapping were performed using a JEOL USA JEM-2100F (Cs corrector). Gas sorption isotherms were measured using a BELSORP-max (BEL Japan, Inc.) adsorption system, employing a standard volumetric technique up to saturation pressure. N_2 (purity of 99.999%) sorption isotherms were monitored at 77 K, CO_2 (purity of 99.999%) sorption isotherms were. All UV-Vis spectra were collected using a Cary 5000 (Agilent) UV-Vis-NIR (200–3300 nm) spectrophotometer. Fluorescence spectra were collected with a Cary Eclipse fluorometer (Varian) with 5 nm slit width. Quantum yields of MOFs were collected using a FP-8500ST spectrofluorometer (Jasco International).

Preparation of MOFs

Preparation of MIL-53-H/DMF

$[In(OH)(BDC\text{-}(OH)_2)]_x$. MIL-53-H/DMF was prepared using slightly modified published procedure. [36] A mixture of $In(NO_3)_3 \cdot xH_2O$ (0.150 g, 0.50 mmol) was dissolved in 5 ml of H_2O, $H_2BDC\text{-}(OH)_2$ (0.099 g, 0.50 mmol) was dissolved in 5 mL DMF and mixed the solutions. The mixed solution in a tightly sealed 20 mL vial was heated at 85 °C for 1 day to form colorless crystals. The crystals harvested were washed using fresh DMF (10 ml for 4 times) first and then acetone (10 ml 4 times) then vacuum dried at 120 °C for a day. EA of $[In(OH)(BDC\text{-}(OH)_2)]$, $C_8H_5O_7In$, fw = 327.8 g/mol. Calculated: C, 29.3; H, 1.5; O, 34.1%. Found: C, 28.7; H, 1.9; O, 33.8%.

Preparation of MIL-53-H

$[In(OH)(BDC\text{-}(OH)_2)](H_2BDC\text{-}(OH)_2)_{0.6}(H_2O)$. A mixture of $In(NO_3)_3 \cdot xH_2O$ (0.225 g, 0.75 mmol) was dissolved in 10 ml of H_2O and $H_2BDC\text{-}(OH)_2$ (0.099 g, 0.50 mmol) was added into the solution. The solution in a tightly sealed 20 mL vial was heated at 100 °C for 1 day to form yellow crystals. The crystals harvested were washed using fresh hot water (10 ml for 5 times) and then vacuum-dried at room temperature for a day. EA of $[In(OH)(BDC\text{-}(OH)_2)](H_2BDC\text{-}(OH)_2)_{0.6}(H_2O)$, $C_{12.8}H_{10.6}O_{11.6}In$, fw = 464.8 g/mol. Calculated: C, 33.0; H, 2.3; O, 39.9%. Found: C, 33.0; H, 2.0; O, 39.3%.

Preparation of MIL-53-D

$[In(OH)(BDC\text{-}(OH)_2)]$. MIL-53-D was synthesized according to the procedure used in MIL-53-H, but instead of H_2O, D_2O was used in synthesis and washing solvent.

Hammett indicator tests

This protocol was used in the same manner as published procedures. [37] A set of stock Hammett indicator solutions (2 mM) was prepared by dissolving each Hammett indicator in anhydrous benzene under ambient conditions. Approximately 5 mg of each activated MOF sample was placed in a 2 mL indicator solution under ambient conditions, and the color of the MOF was monitored after 1 h.

Measurement of UV–Vis spectra. In a typical UV–Vis experiment, 0.4 mg of MOFs was immersed in a cuvette with 2.5 mL of solvent, respectively. The mixture was sonicated for 10 min to make a fine suspension. UV–Vis spectra were recorded in the range 200–800 nm.

Steady-state fluorescence measurements. In a typical steady-state fluorescence experiment, 1.2 mg of MOFs was immersed in a cuvette with 2.5 mL of solvent, respectively. The suspension was excited at 350 nm and the fluorescence emission was measured in the range 370-700 nm.

Single-crystal structure analyses of the MOFs

The diffraction data of single crystals of **MIL-53-H** coated with Paratone oil were measured at either 298 K with synchrotron radiation (λ = 0. 800 Å) on an ADSC Quantum-210 detector at 2D SMC with a silicon (111) double crystal monochromator at the Pohang Accelerator Laboratory, Korea. The ADSC Q210 ADX software[38] was used for data collection (detector distance 63 mm, omega scan; Δω = 1°, exposure time 1 s per frame) and HKL3000sm (ver. 703r)[39] was used for cell refinement, reduction, and absorption correction. All crystal structures were solved by a direct method using the XS program and refined by full-matrix least-squares calculations using the XL program of the SHELX program package.[40]

[In(OH)(BDC-(OH)$_2$], **MIL-53-H.** A yellow block-shaped crystal, 0.018 × 0.015 × 0.015 mm^3, $C_8H_4O_7In$, fw = 326.93 g·mol^{-1}, monoclinic, space group *C2/m*, a = 13.894(3) Å, b = 18.365(4) Å, c = 7.1843(14) Å, β = 119.93(3), V = 1588.7(7) Å^3, Z = 4, T = 298 K, μ (synchrotron, λ = 0.800 Å) = 2.034 mm^{-1}, 4,757 reflections were collected, 1,354 were unique [R_{int} = 0.1087]. All non-hydrogen atoms were refined anisotropically; the hydrogen atoms were assigned isotropic displacement coefficients U(H) = 1.2U (C and μ-O) or 1.5U (O), and their coordinates were allowed to ride on their respective atoms. Least-squares refinement of the structural model was performed under geometry restraints such as DELU and SIMU. Final refinement was performed with modification of the structure factors for the electron densities of the disordered solvents (744.7 Å^3, 46.9% of the total unit cell volume; 358 electrons correspond to ~36 water molecules per unit cell) using the SQUEEZE option of PLATON. The hydrogen atoms of the water molecules are not included in the least-squares refinement. Refinement of the structure converged at $R1$ = 0.0561 and $wR2$ = 0.1442 for 1,058 reflections with $I > 2\sigma(I)$; $R1$ = 0.0640 and $wR2$ = 0.1506 for all 1,354 reflections. The largest difference peak and hole were 2.042 and –0.916 e·Å^{-3}, respectively.

Table 4.1. Crystal data and structure refinement of **MIL-53-H**.

Empirical formula	$C_8H_4O_7In$	
Formula weight	326.93	
Temperature	298(2) K	
Wavelength	0.800 Å	
Crystal system	Monoclinic	
Space group	*C2/m*	
Unit cell dimensions	a = 13.894(3) Å	α = 90°
	b = 18.365(4) Å	β = 119.93(3)°
	c = 7.1843(14) Å	γ = 90°
Volume	1588.7(7) $Å^3$	
Z	4	
Density (calculated)	1.367 Mg/m^3	
Absorption coefficient	2.034 mm^{-1}	
F(000)	628	
Crystal size	0.018 × 0.015 × 0.015 mm^3	
Theta range for data collection	2.497 to 27.996°	
Index ranges	–16<=h<=16, –21<=k<=21, –8<=l<=8	
Reflections collected	4757	
Independent reflections	1354 [R(int) = 0.1087]	
Completeness to theta = 27.996°	96.6 %	
Absorption correction	Empirical	
Max. and min. transmission	1.000 and 0.964	
Refinement method	Full-matrix least-squares on F^2	
Data / restraints / parameters	1354 / 54 / 79	
Goodness-of-fit on F^2	1.132	
Final R indices [I>2sigma(I)]	R1 = 0.0561, wR2 = 0.1442	
R indices (all data)	R1 = 0.0640, wR2 = 0.1506	
Extinction coefficient	n/a	
Largest diff. peak and hole	2.04 and –0.916 e·$Å^{-3}$	

4.2 Results and Discussion

Reported MIL-53(In)-$(OH)_2$ which was synthesized with $In(NO_3)_2 \cdot 6H_2O$ and 2,5-dihydroxy1,4-benzenedicarboxylic acid (H_2BDC-$(OH)_2$) using mixed solvent system of H_2O and DMF (**MIL-53-H/DMF**). The structure is a MIL-53 analogue containing dihydroxyl groups in linker, with hydrogen bonding and π-π interaction sites feasible for fluorescence detection of nitroaromatic compounds in water (**Figure 4.2**).[36] As the result of reported studies revealing plausible interactions using free hydroxyl group, **MIL-53-H/DMF** can be assumed to be utilized for fluorescence sensing H_2O in D_2O via hydrogen bonding. The fluorescence spectrum of **MIL-53-H/DMF** in H_2O showed the one major emission peak at 450 nm and a shoulder emission peak at 535 nm. On the other hand, in D_2O, **MIL-53-H/DMF** indicated clear two emission peaks at 450 and 550 nm (**Figure 4.3**). The fluorescence photographs of **MIL-53-H/DMF** in H_2O or D_2O solution appear opaque. In order to determine where the two emission peaks came from, the solid and the solution was separated. The fluorescence spectra of the filtrate in H_2O (535 nm) and D_2O (550 nm) revealed a single peak consistent with one of the peaks of **MIL-53-H/DMF** in H_2O or D_2O, respectively. These emission peaks were different from the ligand's seen in H_2O or D_2O. Another fluorescence peak at 450 nm originates from the bulk framework, the solid. Fluorescence photographs of **MIL-53-H/DMF** soaked in H_2O (blue) or D_2O (white) indicated different colours of the filtrate, which were green (535 nm) in H_2O and yellow (550 nm) in D_2O (**Figure 4.4**). The white emission from D_2O in UV can be assigned to bulk structure (blue at 450 nm of emission) and the decomposed structure (yellow at 550 nm), whereas the blue emission from H_2O was the predominant light for the bulk structure (450 nm) and the decomposed structure appeared weakly in full light.[41] Absorbance spectra of bulk and filtrate showed similar absorbance peaks (**Figure 4.5**).

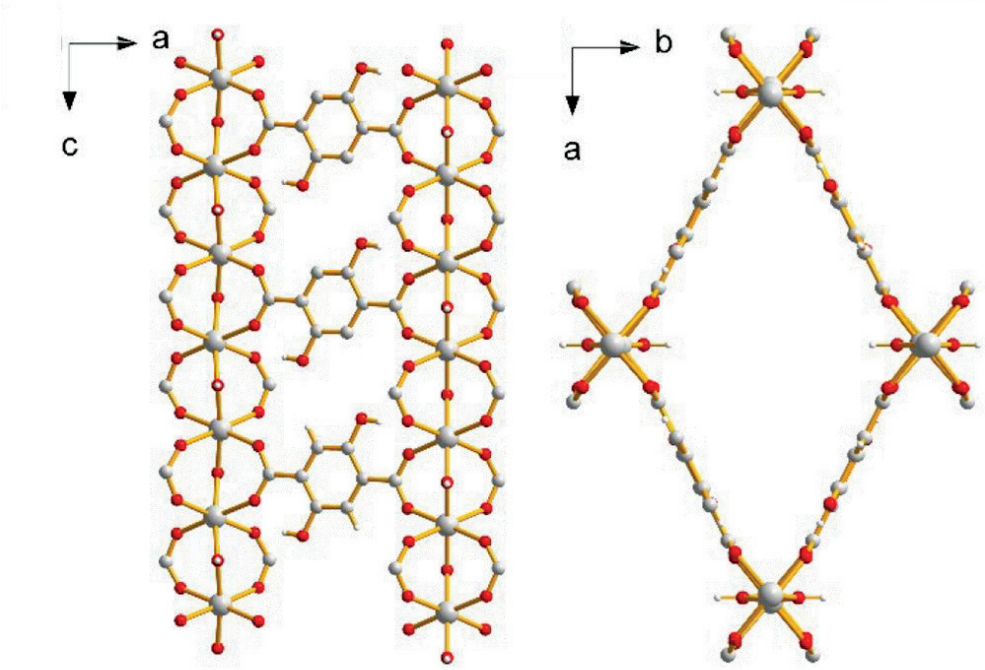

Figure 4.2. The reported structure of **MIL-53-H/DMF**.[36]

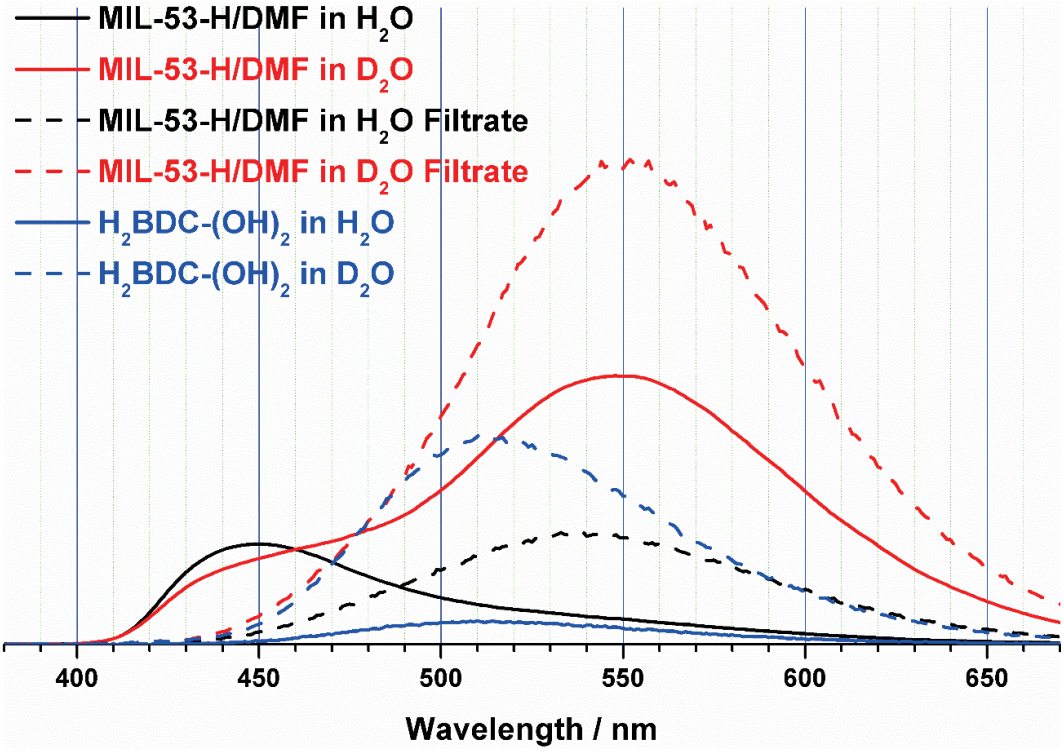

Figure 4.3. Fluorescence spectra of **MIL-53-H/DMF** and filtrates in H_2O and D_2O. Those were emission peaks different from the ligands.

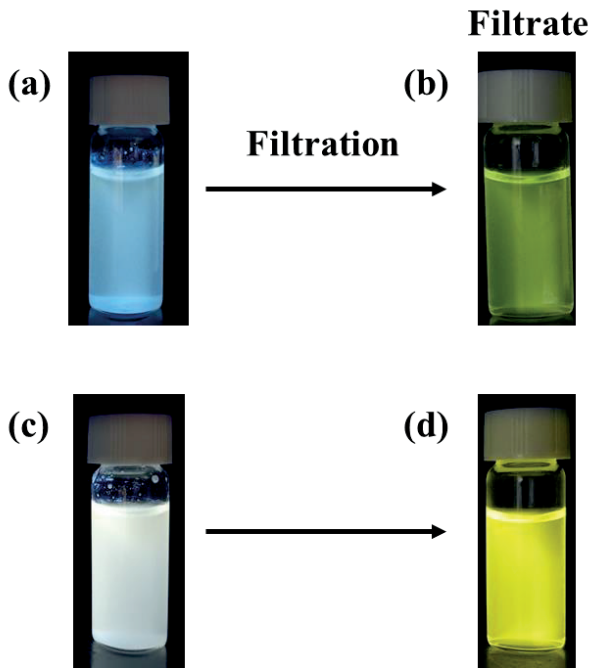

Figure 4.4. The fluorescence photographs of **MIL-53-H/DMF** in (a) H_2O and (b) filtrate after filtration, in (c) D_2O and (d) filtrate after filtration under 352 nm of UV light.

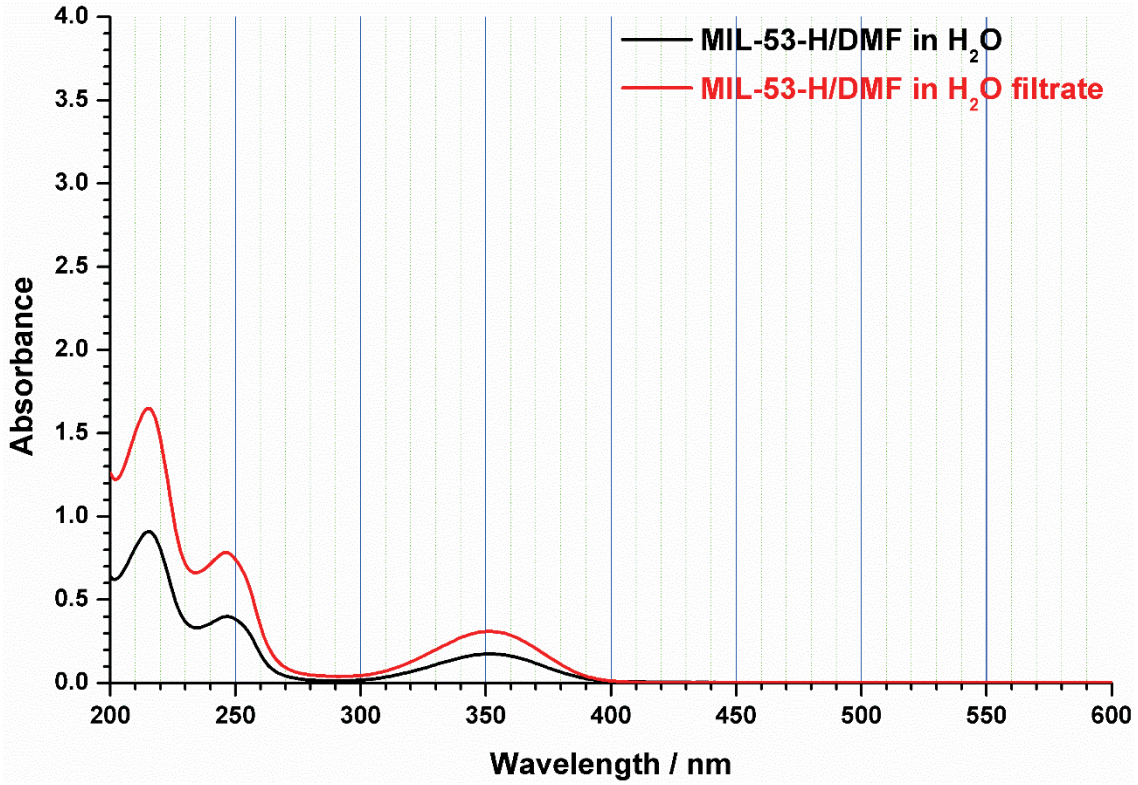

Figure 4.5. Absorbance spectrum of **MIL-53-H/DMF** in H_2O and filtrate removed solid MOF.

To discover the properties of the filtrate, small amounts of nanoparticles were obtained by evaporating H_2O from the filtrate. The nanoparticles were so small in particle size (10-20 nm) that PXRD patterns was not shown (**Figures 4.6** and **4.7**).[42] Surprisingly, the nanoparticles had different binding modes compared to **MIL-53-H/DMF** and ligand**,** resulting in different fluorescent emission (**Figure 4.8**). Free carboxylate bands are seen in the nanoparticle. A deliberate soaking of **MIL-53-H/DMF** in H_2O, leads to the dissociation of crystals to less than 10 μm particle size from 40-50 μm (**Figures 4.9a** and **b**). From the high resolution SEM image of the surface, it can be confirmed that MOF consists of nano-crystals with a size of 10 to 20 nm (**Figures 4.9c** and **d**).[43,44] After immersion in water, the crystallites were less dense compared to the pre-soaked sample and cracks were introduced between crystallites (**Figures 4.9c** and **d**). Nano-crystal dissociated and dispersed in water displayed different binding modes and exhibited different fluorescence properties.

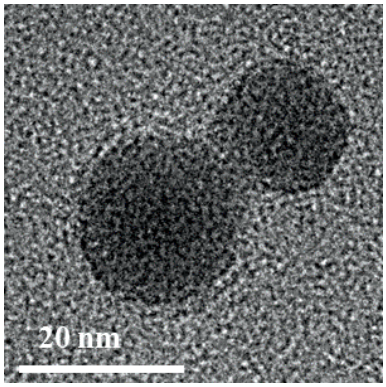

Figure 4.6. TEM image of dried particle from filtrate **MIL-53-H/DMF** in H_2O.

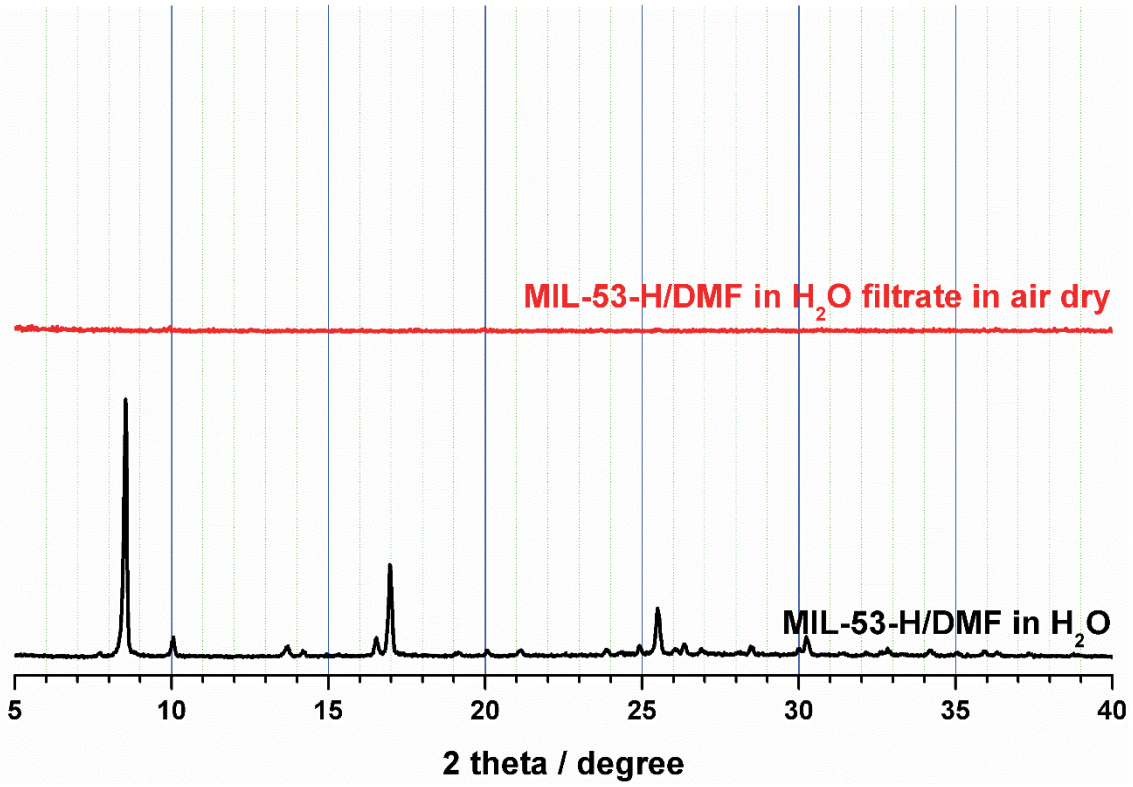

Figure 4.7. PXRD patterns of dried particle from filtrate **MIL-53-H/DMF** in H_2O.

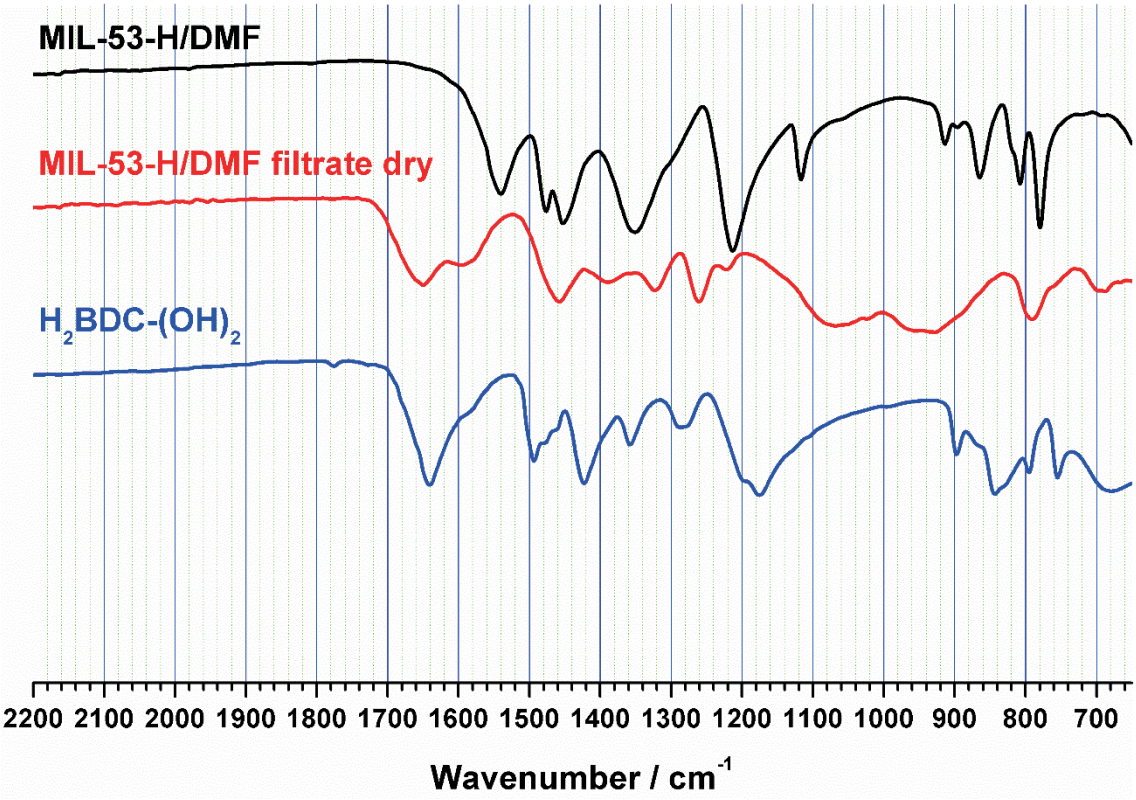

Figure 4.8. FT-IR spectra for comparison of dried particle from filtrate **MIL-53-H/DMF** in H_2O.

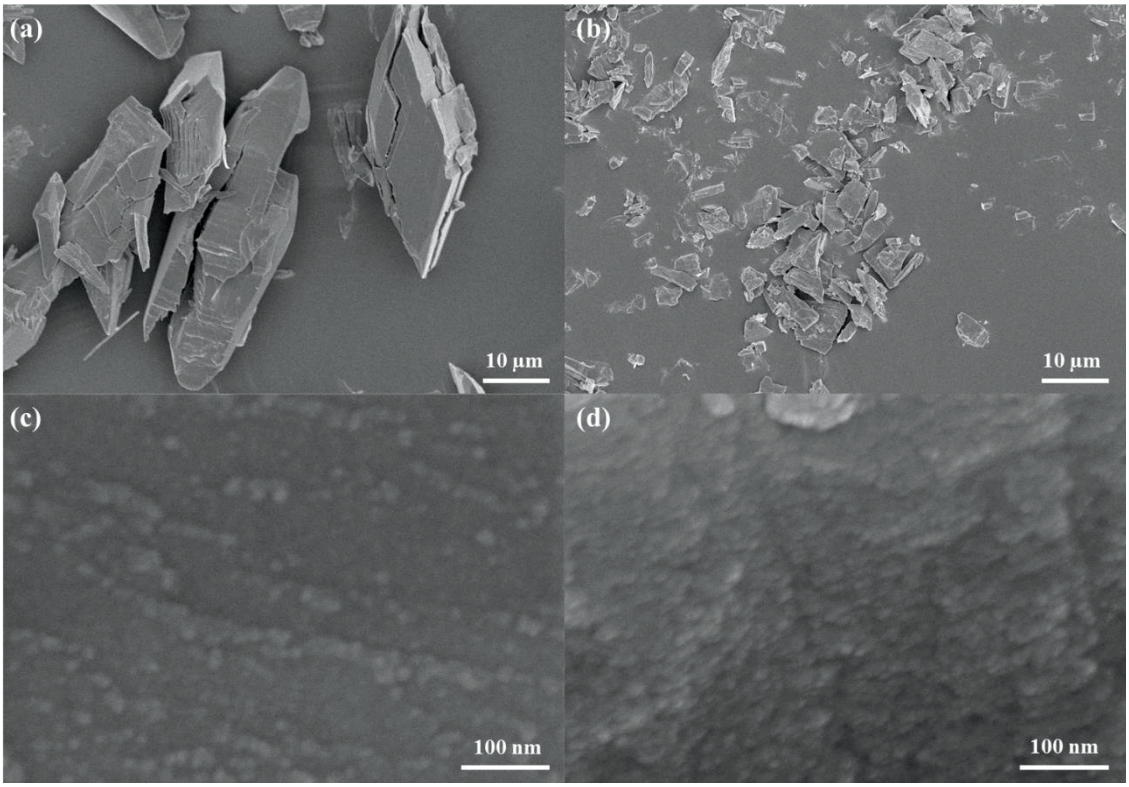

Figure 4.9. SEM Image of **MIL-53-H/DMF** (a), (c) before added H_2O and (b), (d) after added H_2O. (c) and (d) are the surface of the crystal.

In order to check whether the crystals of **MIL-53-H/DMF** were repeatedly split by either H_2O or D_2O, crystals were first immersed in water and then filtrated and then immersed again for 3 cycles. The two types of fluorescence emission peaks were still present because framework was repeatedly broken in water, but the tendency for the degree of repeated cracking was not confirmed (**Figure 4.10**). In addition, **MIL-53-H/DMF** could not be used as the proper ratiometric fluorescence sensor for H_2O in D_2O because bulk micro-sized sample did not show the linear correlation with H_2O contents in D_2O. Although we could not clarify what is the decomposed nano-sized particle, it revealed the linear correlation of increased H_2O contents in D_2O with decreased fluorescence intensity (**Figure 4.11**).

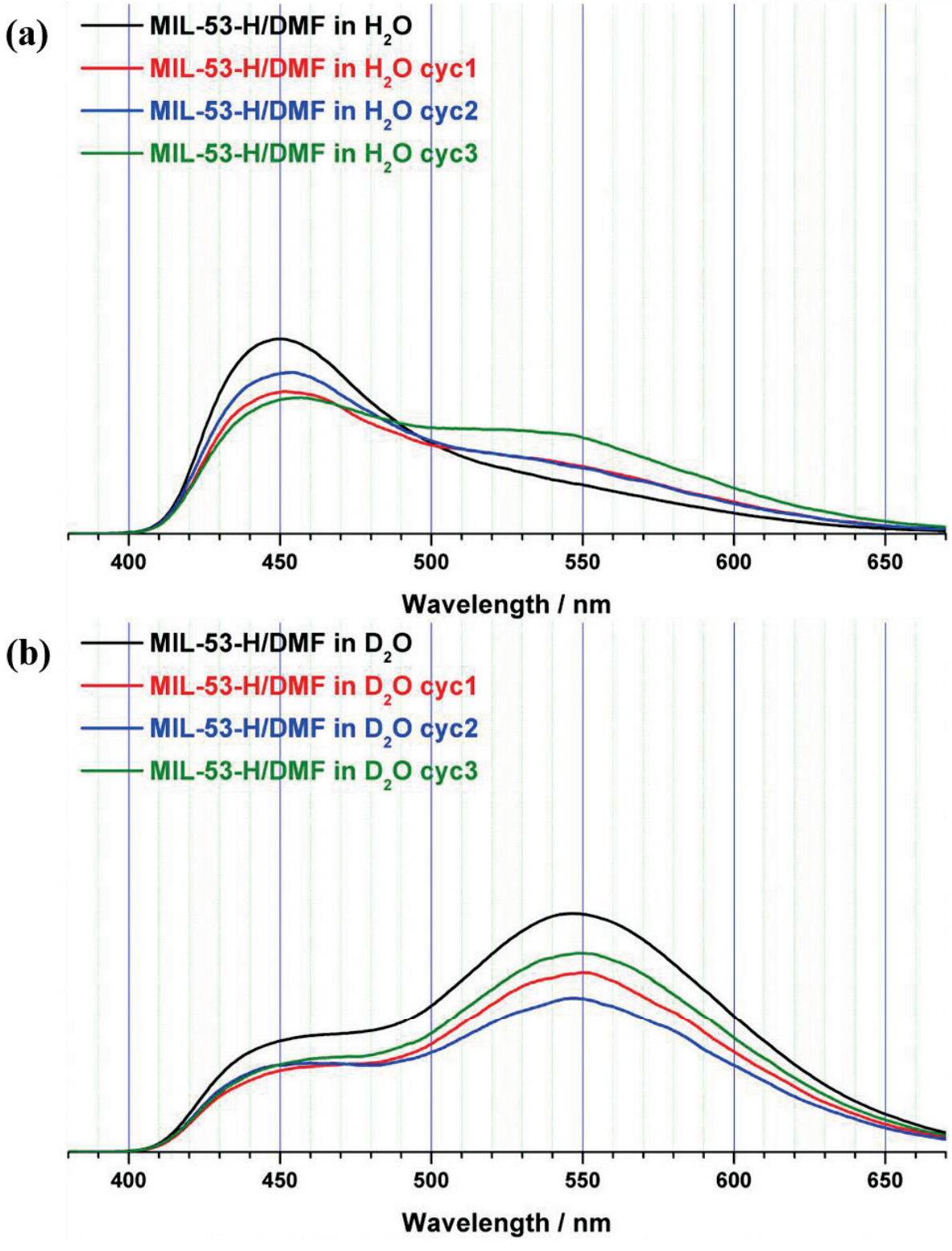

Figure 4.10. Recycling test for **MIL-53-H/DMF** soaked in either (a) H_2O or (b) D_2O.

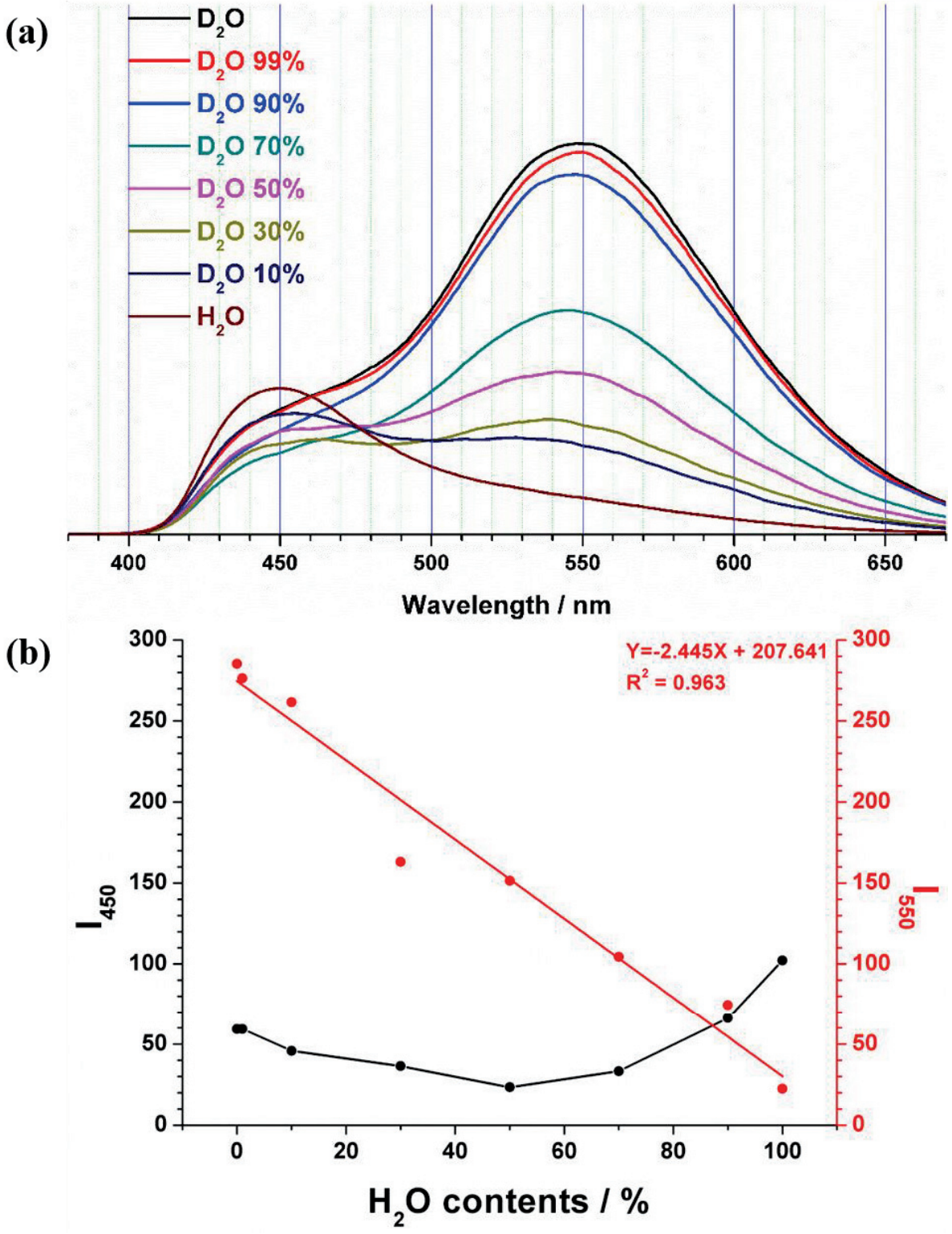

Figure 4.11. MIL-53-H/DMF for ratiometric fluorescence sensing for H_2O in D_2O. (b) Peak intensity from deconvolution of two emission peaks in each ratio of H_2O contents in D_2O.

In N_2 adsorption isotherm above P/P_0 = 0.8, the pore volume is slightly increased by the defect site (**Figure 4.12a**). **MIL-53-H/DMF** was changed to a more rigid structure after treatment with water, which shifted the gate opening pressure to a higher value in CO_2 adsorption at 195 K (**Figure 4.12b**). Besides, water vapour sorption also shows a difference in gate opening pressure (**Figure 4.13**). Surprisingly, while the amount of CO_2 adsorption decreased, the amount of H_2O adsorption increased by 50%, which is thought to be increased due to the exposed hydroxyl group on downsizing surface. The small size frameworks including less defect sites showed the rigid structures [45,46].

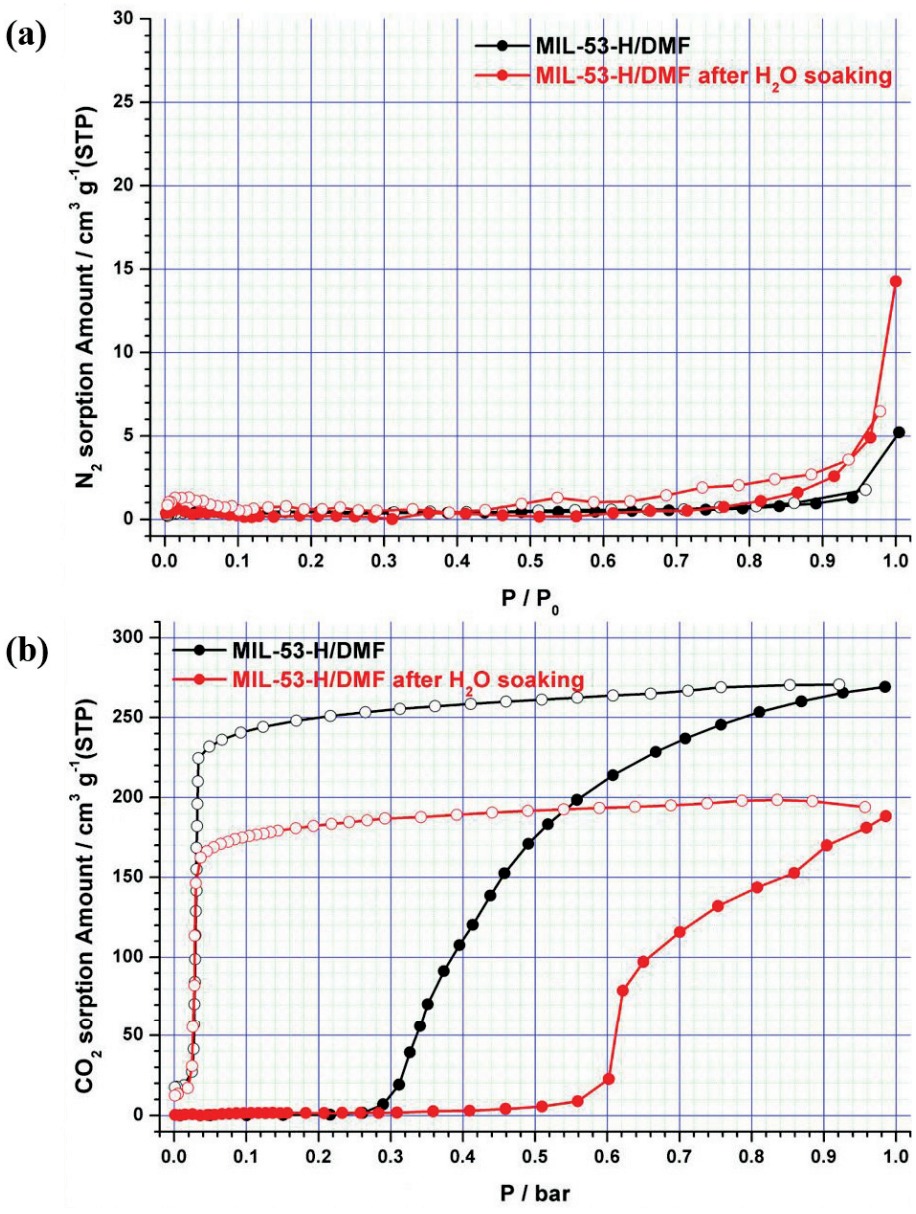

Figure 4.12. (a)N_2 at 77 K and (b) CO_2 at 195 K adsorption of **MIL-53-H/DMF** before and after soaking in H_2O.

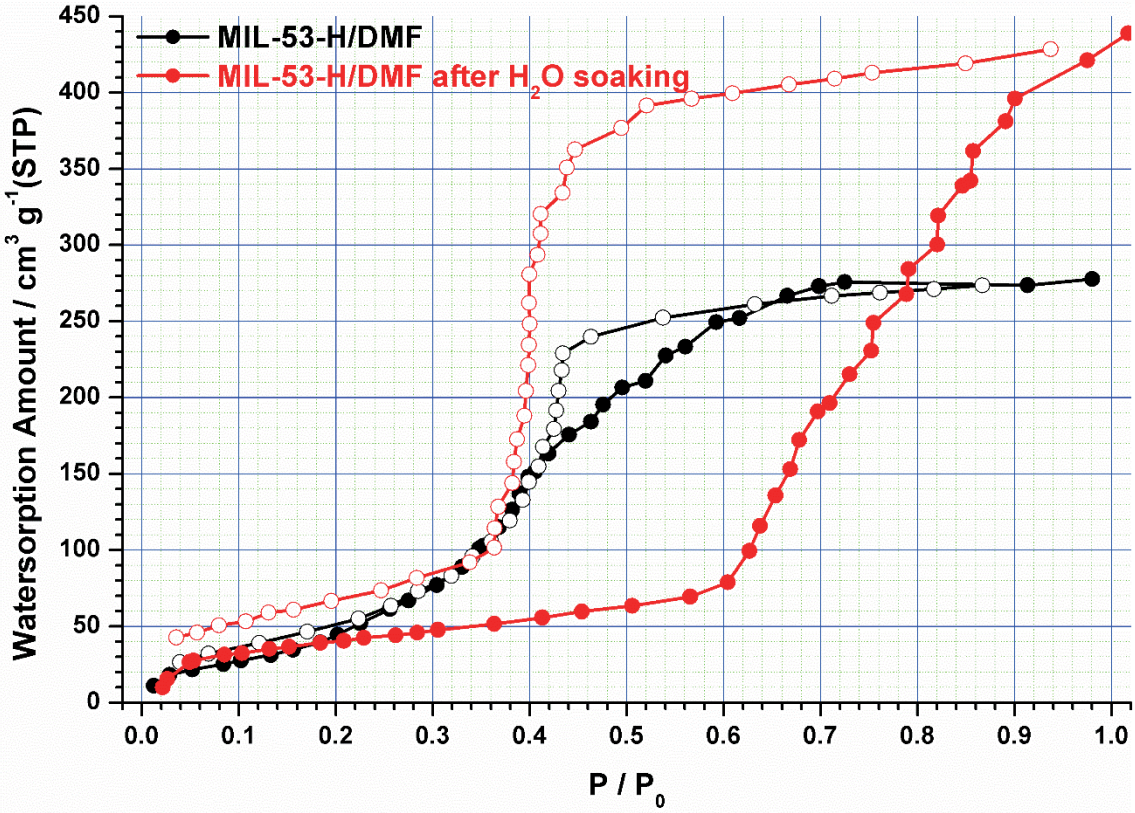

Figure 4.13. H_2O adsorption of pristine **MIL-53-H/DMF** and after H_2O treatment of **MIL-53-H/DMF**.

MIL-53 that was synthesized using water as the synthesis solvent includes free ligand in the as-synthesized material. MIL-53(M)-$(OH)_2$ was previously reported using solvent such as DMF or DEF which does not contain free ligands in the pore.[17,18,36] However, **MIL-53-H** was synthesized using $In(NO_3)_2{\cdot}6H_2O$ and H_2BDC-$(OH)_2$ in H_2O and washed only with hot H_2O. The overall crystal structure of **MIL-53-H** was similar to the reported **MIL-53-H/DMF** structure **(Figure 4.2** and **Table 4.1**). The PXRD patterns of as-synthesized **MIL-53-H** was consistent with simulation of **MIL-53-H.** However, it has different PXRD patterns and the crystal system as that of **MIL-53-H/DMF** soaked in water structure. (**Figure 4.14** and **Table 4.2**) The crystalline structure of **MIL-53-H** was maintained even in activated form (through a vacuum at room temperature) and was similar to the as synthesized **MIL-53-H** which is different from **MIL-53-H/DMF**. When RT activated sample was soaked in H_2O, the structure remained the same as the as-synthesized **MIL-53-H**, whereas the structure of **MIL-53-H/DMF** was still different from any state of **MIL-53-H** (**Figure 4.15**). It was confirmed through optical image that **MIL-53-H** crystal was maintained without dissociating into the smaller crystals in water **(Figure 4.16).**

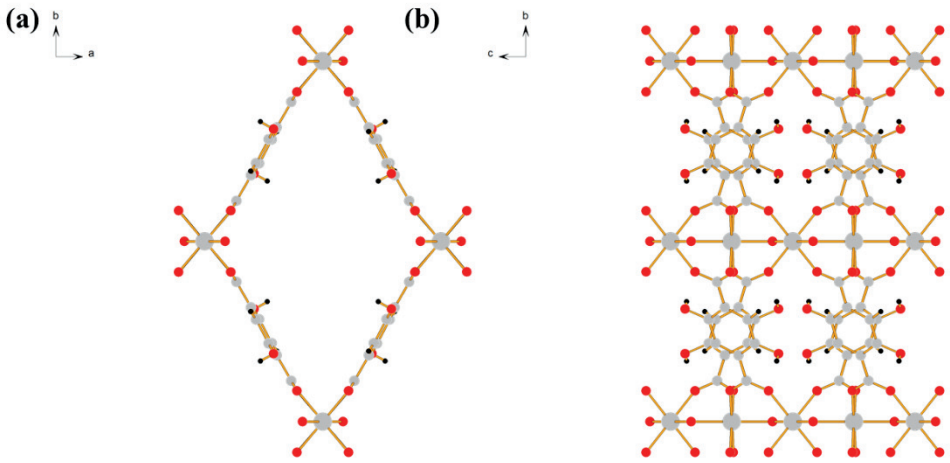

Figure 4.14. Ball and stick diagrams of the single-crystal structure of **MIL-53-H** (a) Framework showing a 1D rhomboidal channel in c-axis view (b) A wall generated by ligands of the BDC-$(OH)_2$ units between 1D rods.

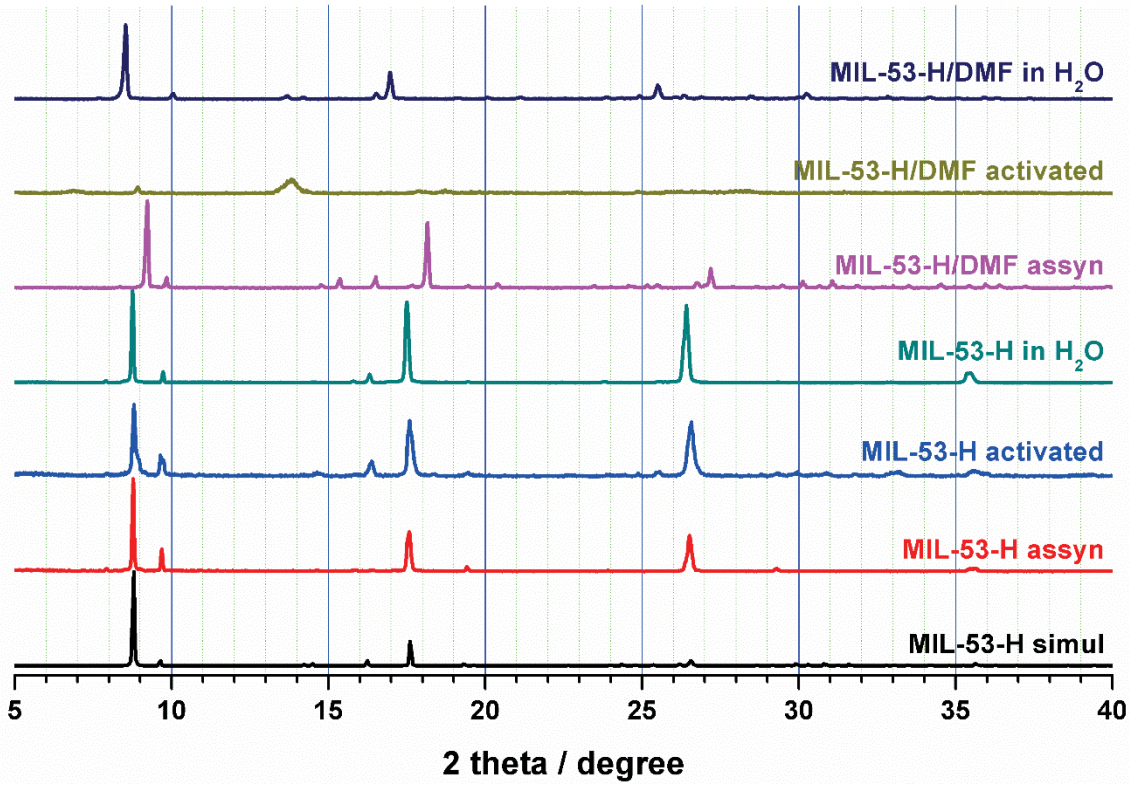

Figure 4.15. PXRD patterns of **MIL-53-H** and **MIL-53-H/DMF** as-synthesized (assyn), upon activation and in H_2O.

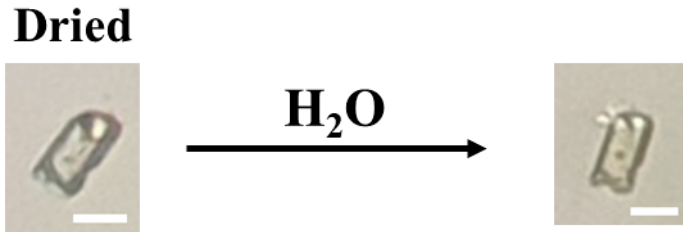

Figure 4.16. Optical image of before and after **MIL-53-H** soaked in H_2O. scale bar is 10 μm.

Table 4.2. Crystal structure of **MIL-53-H**, **MIL-53-H/DMF** upon assyn and in H_2O.

	MIL-53-H	**MIL-53-H/DMF** assyn	**MIL-53-H/DMF** in H_2O
Crystal system	Monoclinic	Orthorhombic	Orthorhombic
Space group	C2/m	Cmca	Cmca
a / Å	13.8940	37.417	35.639
b / Å	18.3650	22.907	25.816
c / Å	7.1843	7.1370	7.1500
β / °	119.932		
Volume / $Å^3$	1589	6117	6578

The binding mode of **MIL-53-H** investigated by FT-IR. In addition, **MIL-53-D** synthesized in D_2O instead of H_2O was compared with **MIL-53-H**. Most of the band signal of **MIL-53-H/DMF** were also present in **MIL-53-H** and **MIL-53-D** and additional bands were seen in **MIL-53-H** and **MIL-53-D** at 1688 and 1505 cm^{-1}, which can be assigned to the carboxylate of free ligand (**Figure 4.17**).[19,47] The carboxylate band of **MIL-53-H** was different that of $H_2BDC\text{-}(OH)_2$ and was similar to the blue shift of free H_2BDC in MIL-53.[47] On the other hand, **MIL-53-H/DMF** showed no carboxylate band of free ligands suggesting that free ligands were not included in the pore. **MIL-53-D** included interacted D_2O in the frameworks appeared with additional bands for D_2O at 2450, 1210 and 1000 cm^{-1}. In the case of MIL-53-X, the role of the solvent used in synthesis solvent has not been clearly reported. Here we interpret that DMF, less polar than water, play the role of disrupting hydrogen bond with free ligands and frameworks during crystal growths.

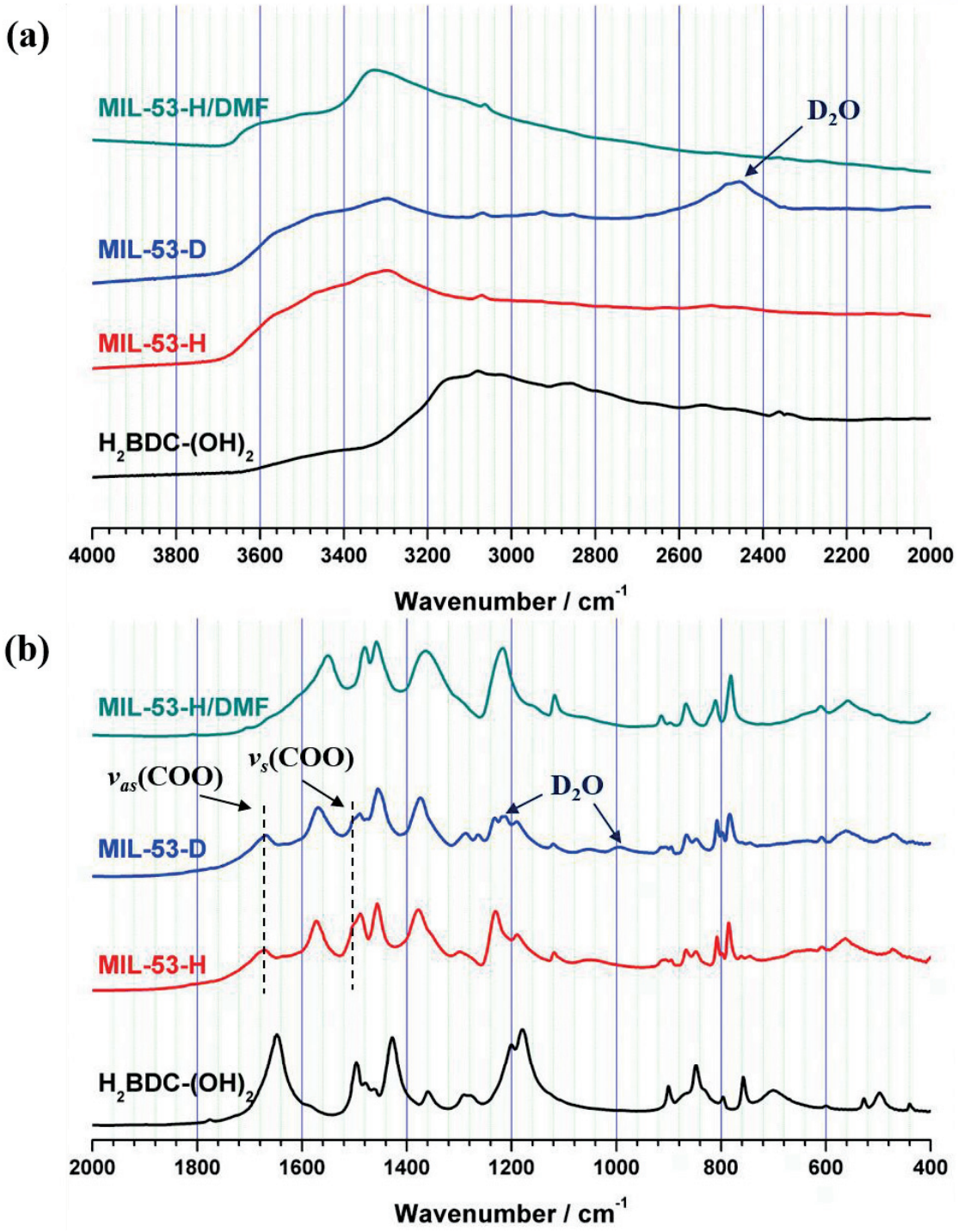

Figure 4.17. FT-IR of $H_2BDC\text{-}(OH)_2$, **MIL-53-H**, **MIL-53-H/DMF** and **MIL-53-D**.

The amount of $H_2BDC\text{-}OH_2$ by TGA

Free ligands and linkers were removed by thermal energy at different temperature to calculate the guest molecules and linker of frameworks.[10,11] **MIL-53-H** showed two major weight loss between room temperature and 800 ℃, with the first weight loss (obsd: 3.4%; calcd 3.5%) corresponding to 1 equivalents of H_2O up to 120 ℃ and the next step, above 250 ℃, removed 1.6 equivalents of $H_2BDC\text{-}(OH)_2$ (obsd 67.5%; calcd 66.2%) from the frameworks. 1 equivalent of $BDC\text{-}(OH)_2$ was due to the linkers of the MOFs and the left of 0.6 equivalent of $H_2BDC\text{-}(OH)_2$ was from the free organic molecule inside the pore. Moreover, elemental analysis (EA) also indicated the 1.6 equivalent of $H_2BDC\text{-}(OH)_2$ in **MIL-53-H**. The thermal stability of intermediate structure (**MIL-53-H**) was slightly better than that of the thermodynamic structure (**MIL-53-H/DMF**), which exhibited a higher decomposition temperature (above 250 ℃) **(Figure 4.18)**.

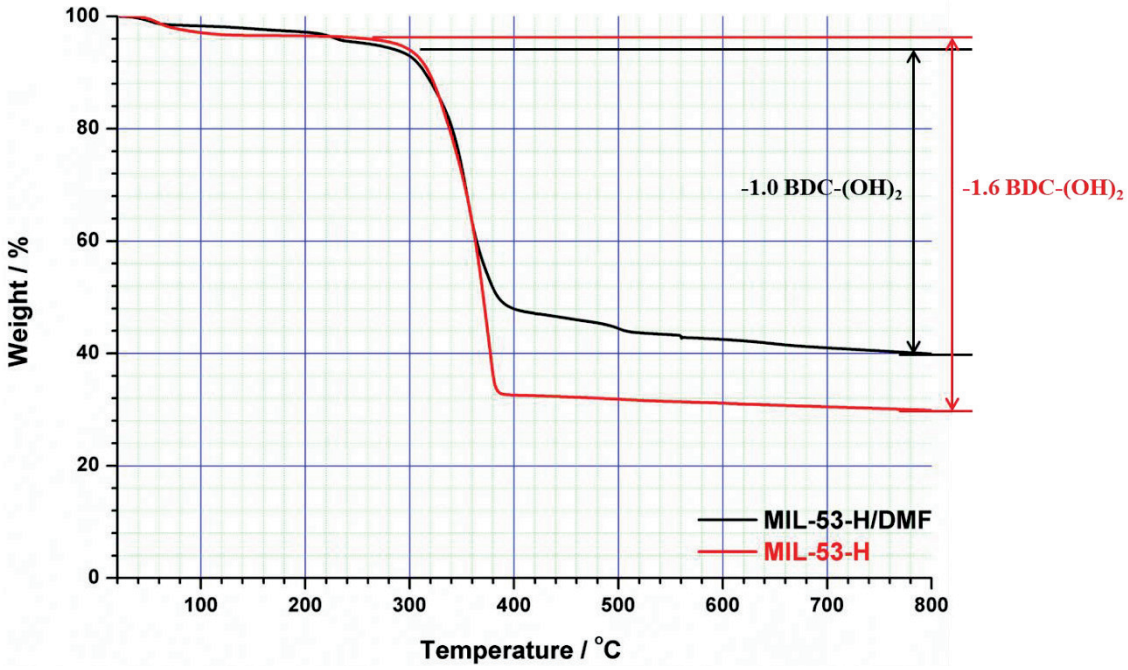

Figure 4.18. TGA of **MIL-53-H** and **MIL-53-H/DMF** in air.

In order to remove the interacted free ligand from the pore, **MIL-53-H** was immersed in methanol, which has sufficient solubility for $H_2BDC\text{-}(OH)_2$. As a result, the overall crystal structure of **MIL-53-H** was easily converted to **MIL-53-H/DMF** in methanol for 1 day (**Figure 4.19a**). The freely interacting $H_2BDC\text{-}(OH)_2$ of **MIL-53-H** can be dissolved in CD_3OD and separated easily from the framework, which was confirmed by FT-NMR spectrum (**Figure 4.20**). After removal of the trapped $H_2BDC\text{-}(OH)_2$ in **MIL-53-H**, the free ligand bands in FT-IR disappeared and changed to the binding mode of **MIL-53-H/DMF** (**Figure 4.19**). $H_2BDC\text{-}(OH)_2$ trapped inside the pore can be removed by using polar solvents (methanol, acetone) (**Figure 4.21**).

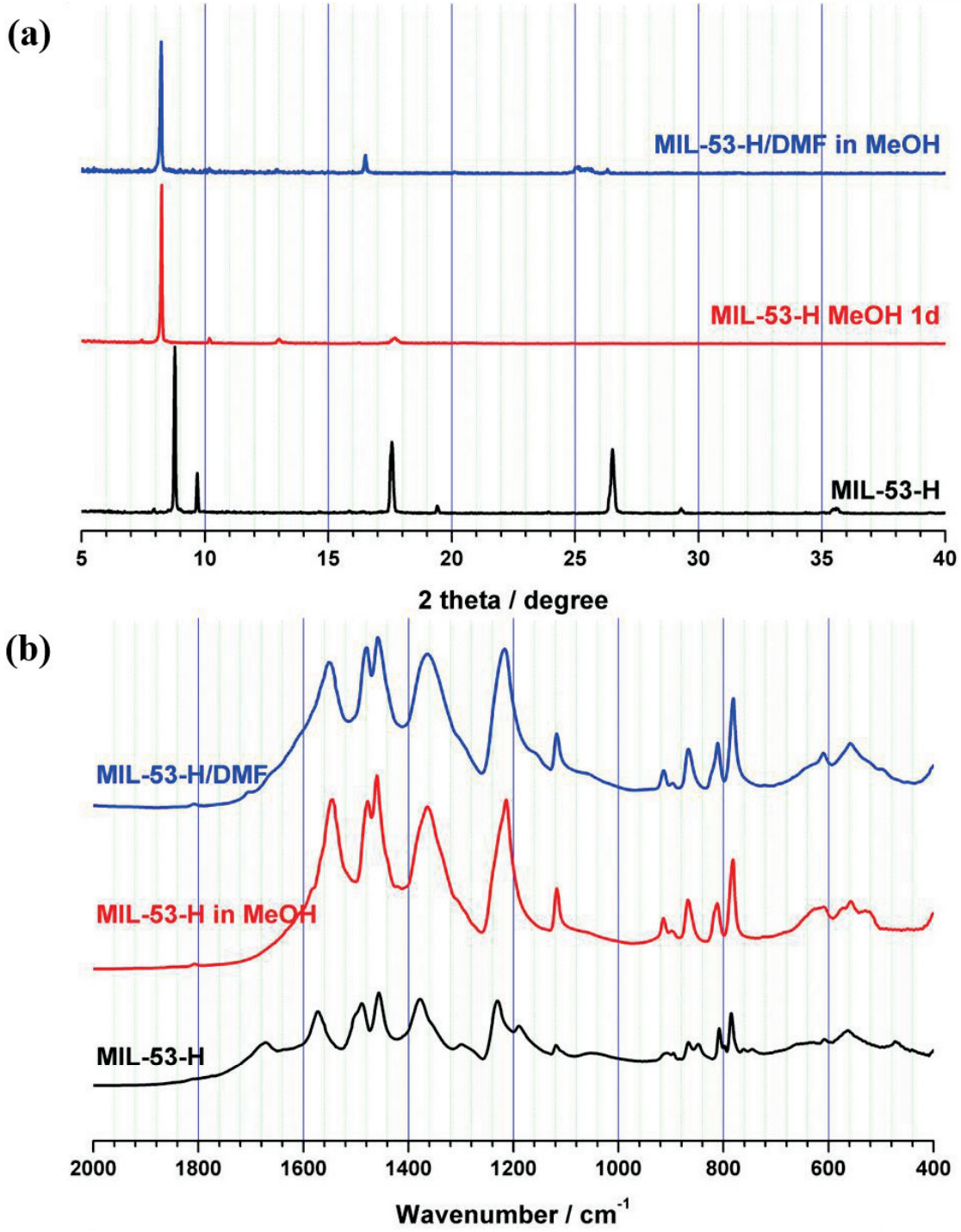

Figure 4.19. (a) PXRD and (b) FT-IR of **MIL-53-H** in methanol.

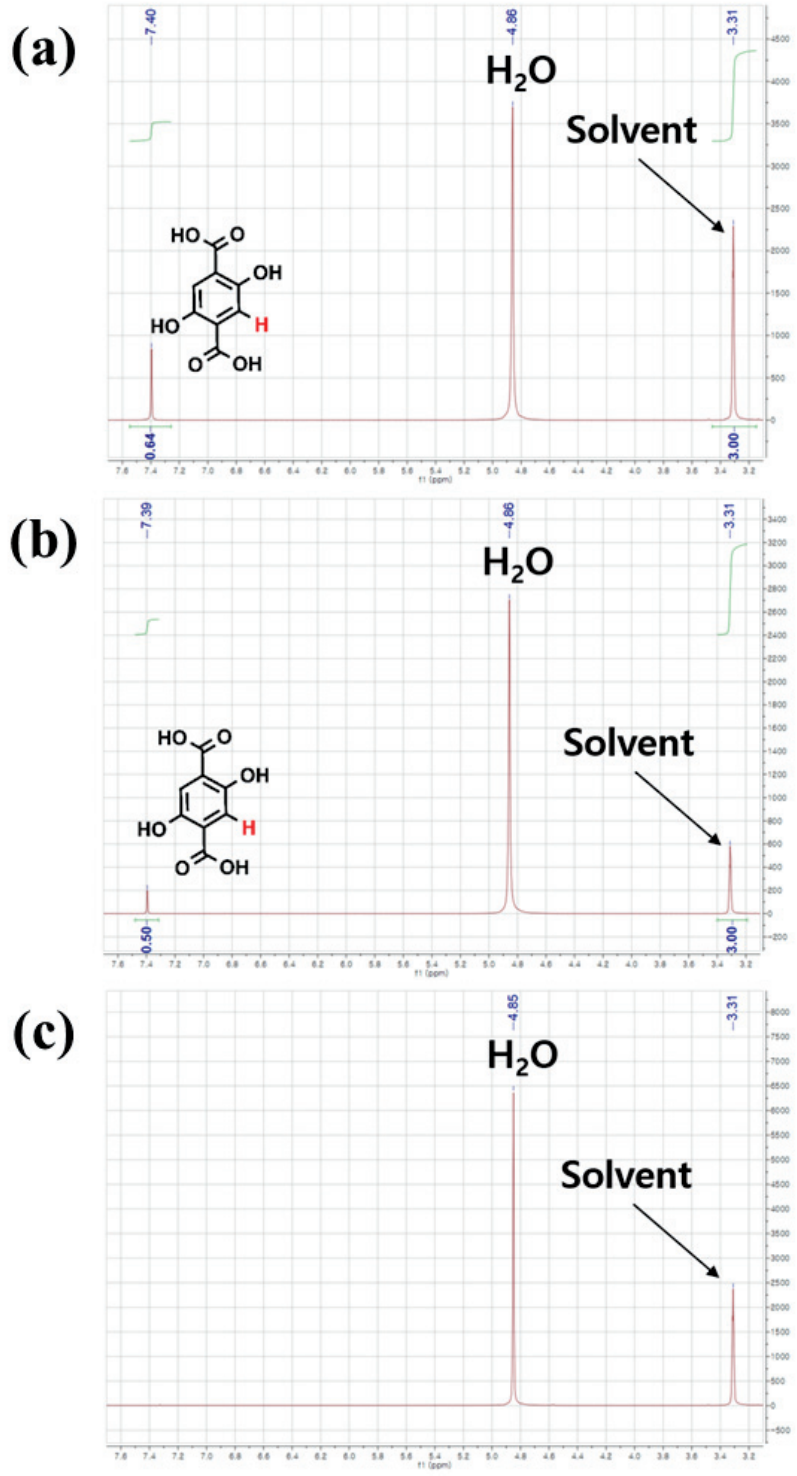

Figure 4.20. FT-NMR of (a) $H_2BDC\text{-}(OH)_2$ dissolved in CD_3OD (b) **MIL-53-H** soaked in CD_3OD (c) **MIL-53-H/DMF** soaked in CD_3OD. $H_2BDC\text{-}(OH)_2$ was encapsulated in **MIL-53-H**, but not encapsulated in **MIL-53-H/DMF**.

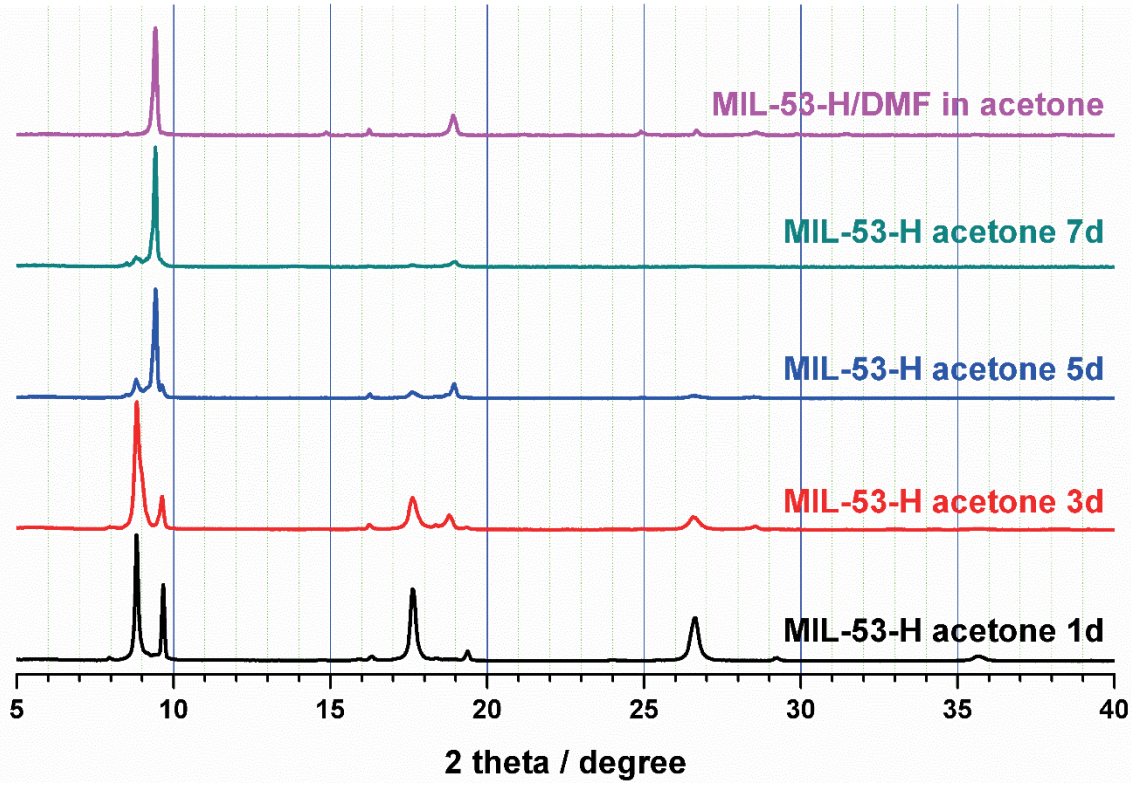

Figure 4.21. PXRD of **MIL-53-H** in acetone.

Thermal stability of MIL-53-H

Above 120 ℃, H_2O evaporated from **MIL-53-H** based on TGA analysis. Its crystallinity decreased and converted to different structures at 120 ℃ in vacuum to remove the water (**Figure 4.22**). Whereas, free $H_2BDC\text{-}(OH)_2$ remained inside the pore as can be seen from the similar binding mode before and after heating (**Figure 4.23**). As $H_2BDC\text{-}(OH)_2$ and H_2O play the important roles for synthesis of crystalline structure to maintain a rigid framework, the crystal structure was recovered to **MIL-53-H** when activated framework was immersed in water.

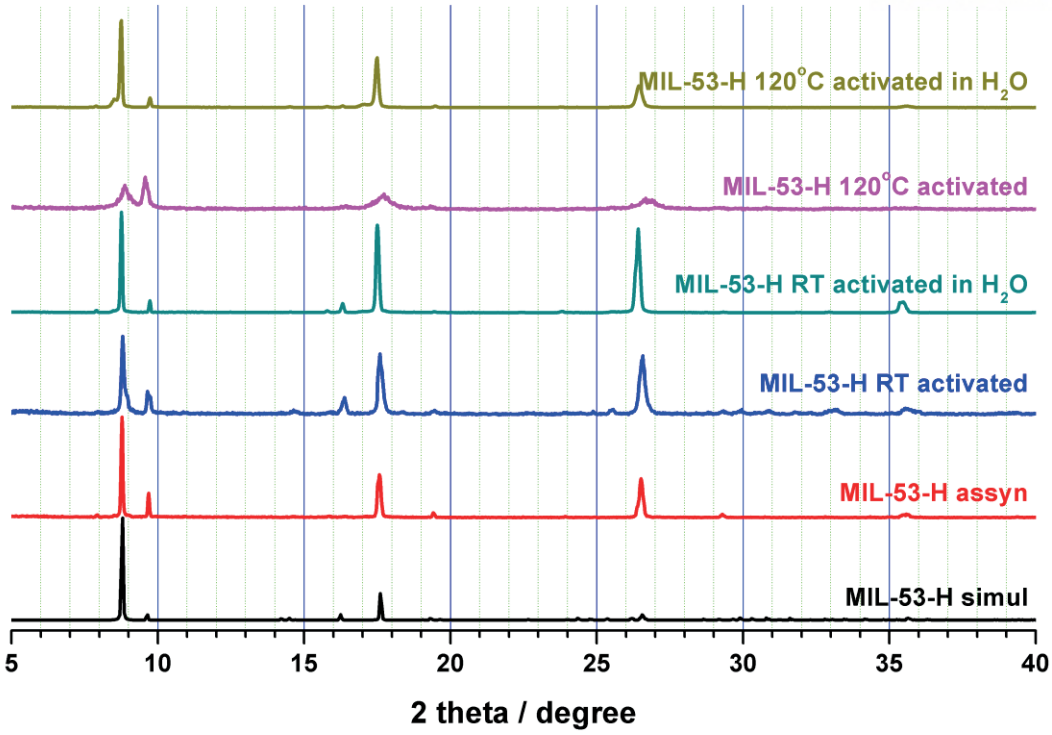

Figure 4.22. PXRD of **MIL-53-H** in different activation temperature for dried and H_2O soaking.

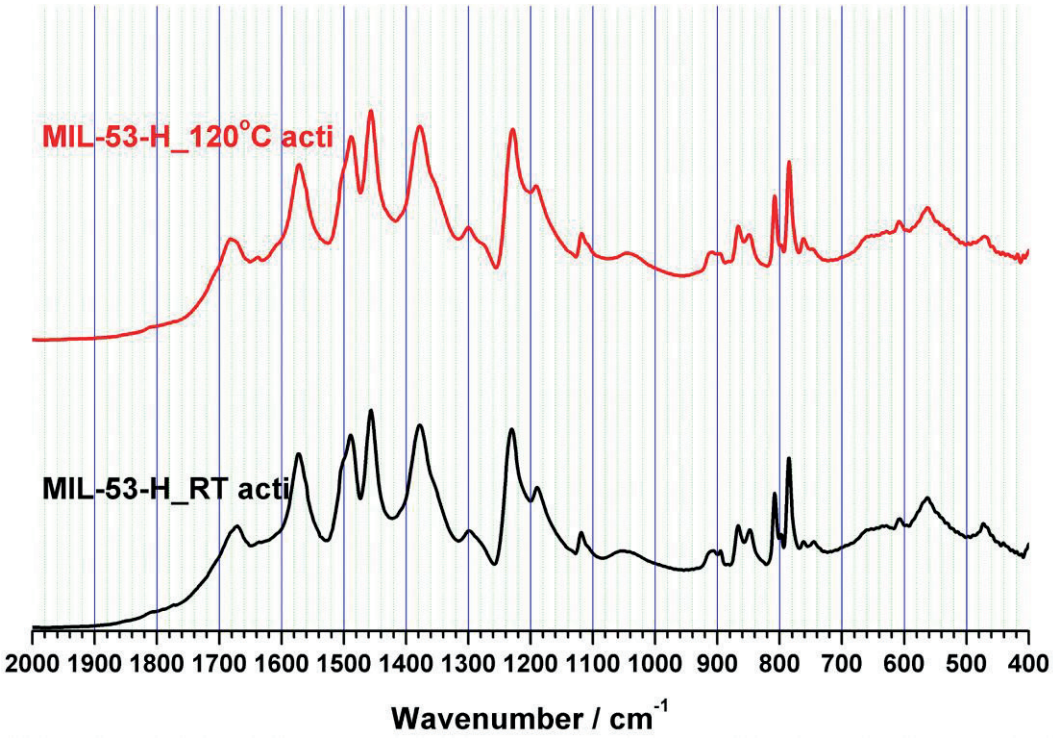

Figure 4.23. FT-IR of **MIL-53-H** in different activation temperature.

Gas sorption and water adsorption of MIL-53-H

Thermodynamic structure, **MIL-53-H/DMF,** is a flexible MOF, and CO_2 sorption isotherms behaviour at 195 K revealed the gate opening phenomenon at P = 0.3 bar. On the other hand, the activated form of **MIL-53-H,** lacks large enough pores to allow N_2 and CO_2 gases to pass through (**Figure 4.24**). **MIL-53-H** has higher hydrophilicity property that opened the pore to allow water molecules to be absorbed, 70 cm g^{-1} of water at P/P_0 = 0.2 and saturating thereafter (**Figure 4.25**).[48] Whereas, **MIL-53-H/DMF** absorbed water almost linearly, but during the desorption isotherms, water was evacuated at P/P_0 = 0.42 which may be due to the interaction between water and the frameworks. **MIL-53-H** has closed pore when H_2O was removed, but when exposed in air, water from humid environment is filled in the framework pore.

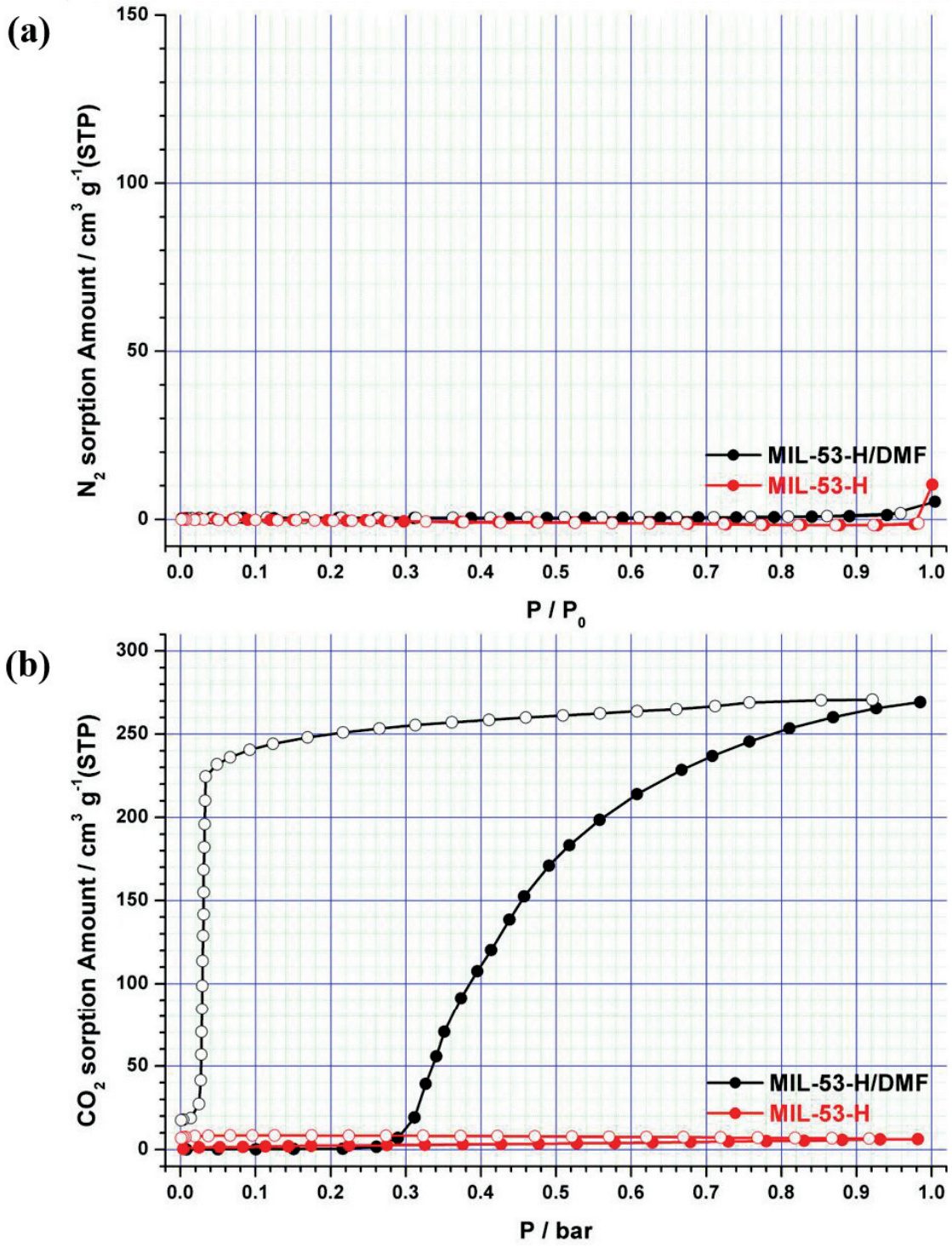

Figure 4.24. (a) N_2 sorption isotherm at 77 K and (b) CO_2 at 195 K sorption isotherm of **MIL-53-H** and **MIL-53-H/DMF**.

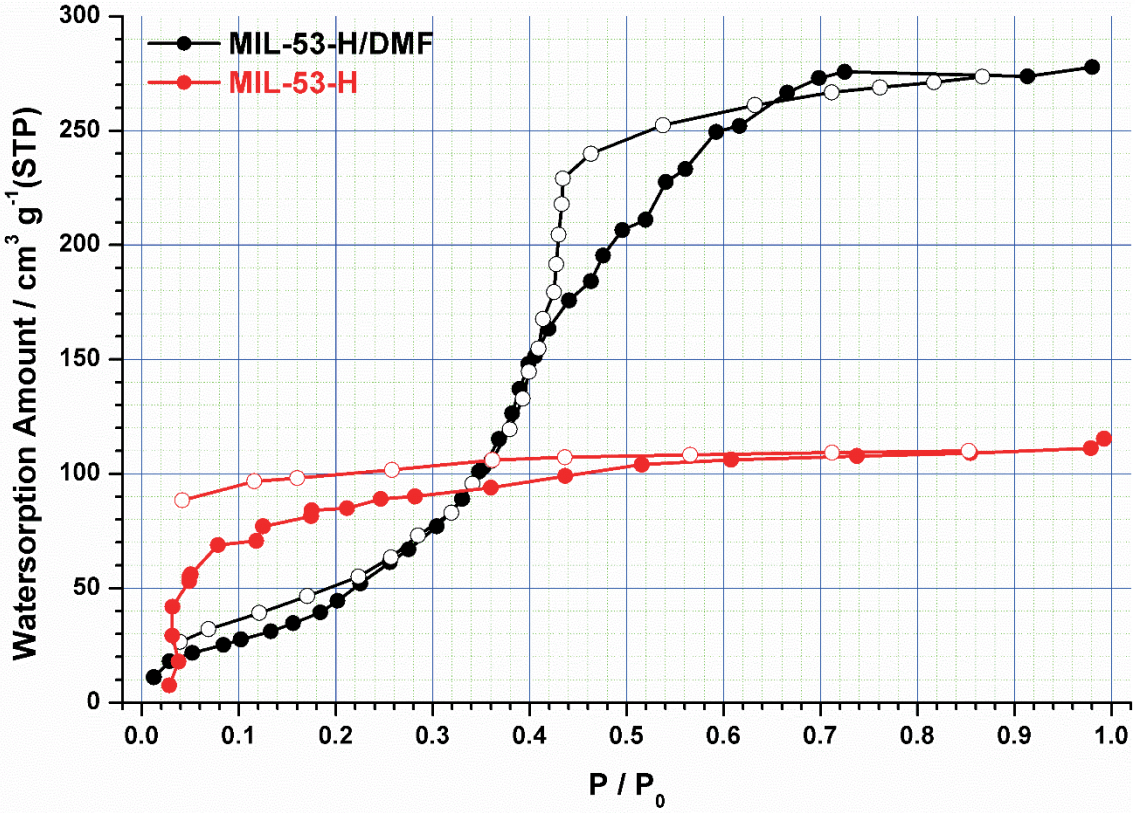

Figure 4.25. H_2O adsorption of **MIL-53-H** and **MIL-53-H/DMF**.

Fluorescence

Depending on the slight variation in acidity of H_2O (RT, pH: 6.4 ~ 7.0) and D_2O (RT, pD: 7.5), the metal-free organic fluorophore including hydroxyl groups uses reactive sites for H_2O and D_2O sensing.[32,35] **MIL-53-H** and **MIL-53-H/DMF** showed similar absorbance spectrum at 350 nm (**Figure 4.26**). Unlike **MIL-53-H/DMF**, which was unstable in water, **MIL-53-H** is stable in water and is used for fluorescence detection for H_2O (535 nm) in D_2O (550 nm) using ratiometric analysis (**Figure 4.27a**). In addition, the fluorescence maximum intensity decreased linearly with increasing H_2O content (**Figure 4.27b**). The hydroxyl group of the framework linker interacts with either H_2O or D_2O, which have different effect on electron transfer from framework linker to the free ligand and consequently fluorescence emission is affected. The LUMO of linker is -2.14 eV and the LUMO of ligand is -2.32 eV so electron transfer process is possible. According to the limit of detection of **MIL-53-H** towards H_2O in D_2O was determined to be less than 1%. Different in intensities for the mixture ratio of H_2O (dark green) and D_2O (bright yellow) can be easily seen from the fluorescence images taken in UV (**Figure 4.28**). Fluorescence quantum yields were also calculated for **MIL-53-H** in H_2O (21%) and D_2O (72%). As **MIL-53-H** was instinctively coordinated with H_2O from humidity as evident from water vapour sorption data, therefore, **MIL-53-H** exhibited the solid-state fluorescence emission at 530 nm similar to that immersed in H_2O (**Figure 4.29**).

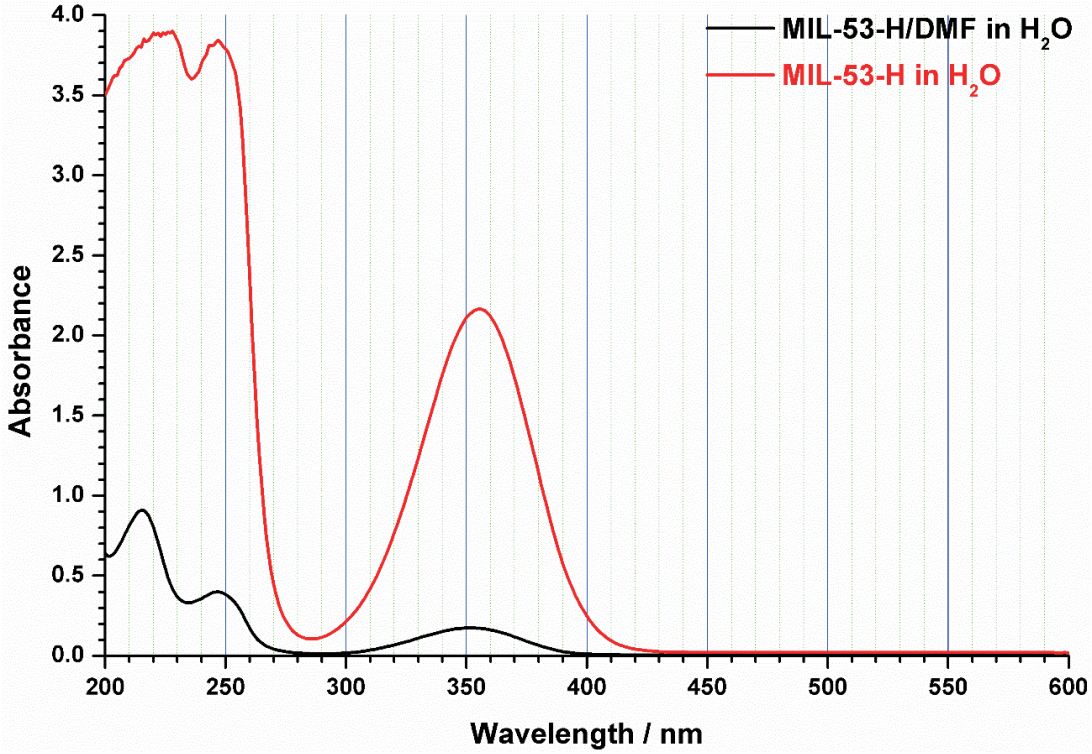

Figure 4.26. Absorbance spectrum of **MIL-53-H** and **MIL-53-H/DMF** in H_2O.

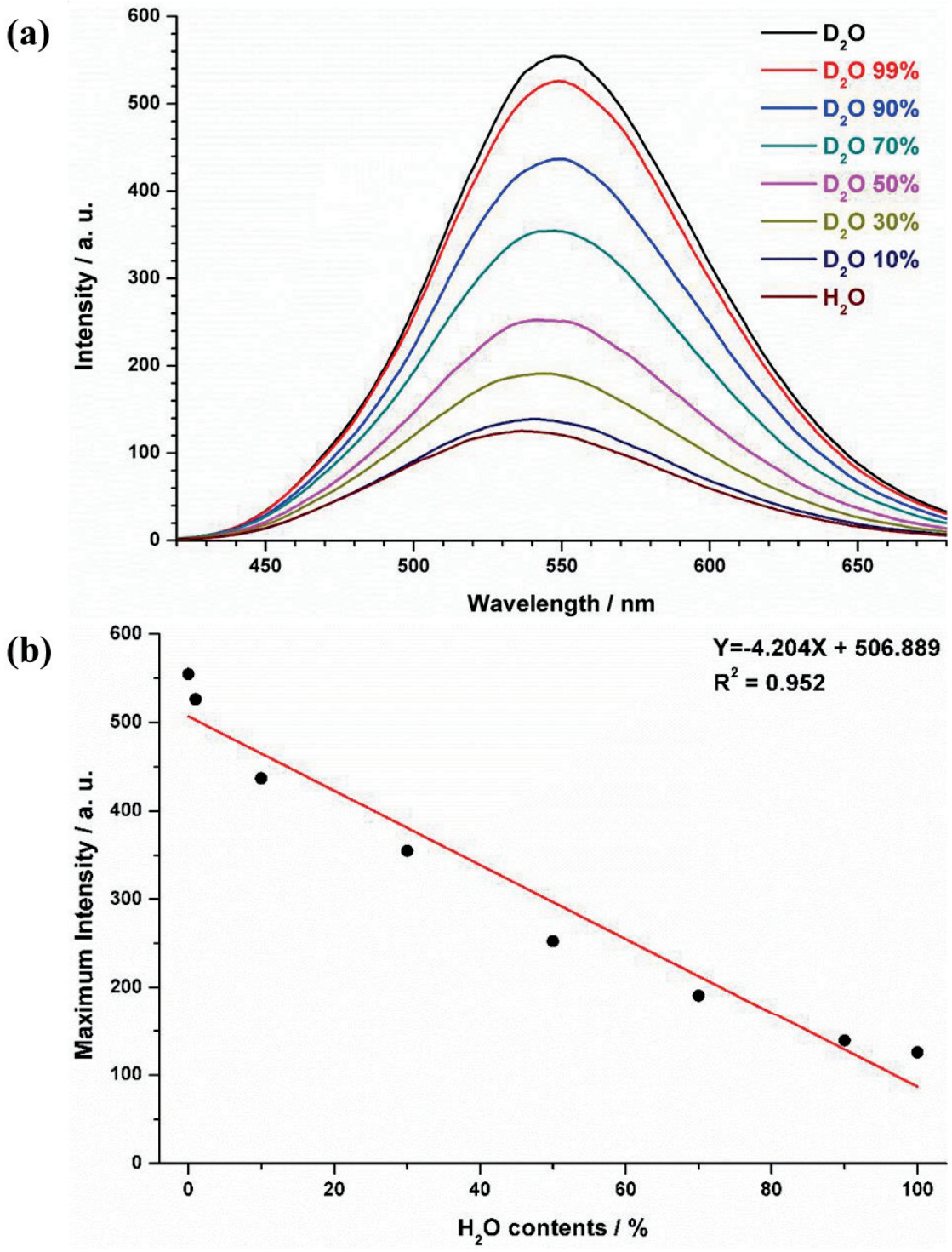

Figure 4.27. (a) Fluorescence spectrum of **MIL-53-H** sample in D_2O with different H_2O contents (b) The fluorescence maximum intensity with H_2O contents in D_2O.

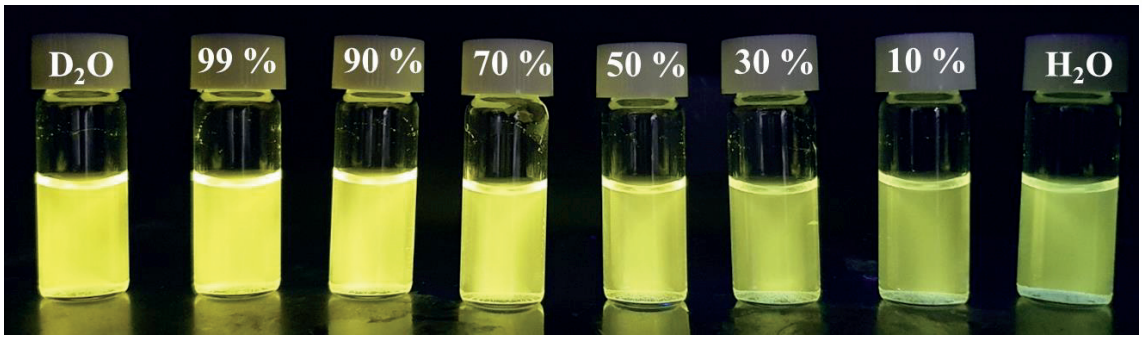

Figure 4.28. The fluorescence photo image of **MIL-53-H** from H_2O to D_2O in different ratio.

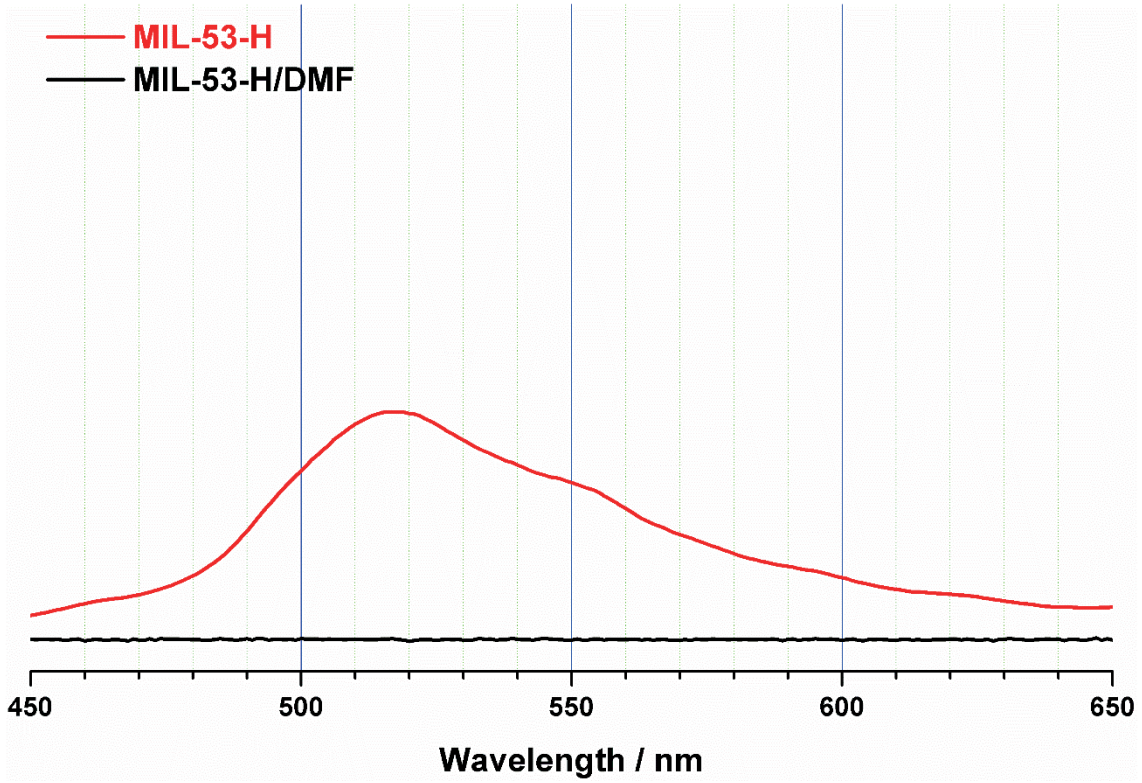

Figure 4.29. Solid fluorescence of **MIL-53-H** and **MIL-53-H/DMF.**

4.4 Conclusion

In summary, depending on the synthesis solvent condition, as-synthesized MIL-53(In)-$(OH)_2$ includes either free ligand or solvent from the pore. Until now, MIL-53(In)-$(OH)_2$ was synthesized using solvent mixture of H_2O and DMF (**MIL-53-H/DMF**), which includes removable solvent guest molecules in the pore. After removing guest molecule, activated **MIL-53-H/DMF** could not withstand sudden breathing behaviour in water. The particle was broken down into small particles from 40-50 μm to less than 10 μm and nanoparticle was seen in opaque aqueous solution. Free hydroxyl group is the detection sites for H_2O in D_2O by fluorescence. **MIL-53-H/DMF** indicated two fluorescence emission peaks in both H_2O and D_2O, which originates from bulk micro-sized crystals and nano-sized crystals, respectively. Nano-sized crystals have different binding mode in comparison to bulk crystals and ligands. In order to stabilize MIL-53(In)-$(OH)_2$, we first synthesized water stable structures of MIL-53(In)-$(OH)_2$ (**MIL-53-H**) that include the free ligands (H_2BDC-$(OH)_2$) interacting with the frameworks by using only water as a synthetic solvent. Excess 0.6 equivalent of free ligands are encapsulated in the pore to make the framework rigid and stable in water. **MIL-53-H** can be converted to the thermodynamic structure, **MIL-53-H/DMF**, when immersed in different polar solvents removing H_2BDC-$(OH)_2$ from the pore. **MIL-53-H** showed promising behaviour as a fluorescent sensor for detection of different ratios of H_2O in D_2O, and can detect less than 1% of H_2O. Until now, the encapsulated free ligand has gone unnoticed due to introduction of porosity by removing the guest molecules. However, through this work, the free ligands stabilize the MOF and opens up new opportunities for various application in water system.

4.5 References

1. Horike, S.; Shimomura, S.; Kitagawa, S. Soft porous crystals. *Nat. Chem*. **2009**, 1, 695-704.
2. Schneemann, A.; Bon, V.; Schwedler, I.; Senkovska, I.; Kaskel, S.; Fischer, R. A. Flexible metal-organic frameworks. *Chem. Soc. Rev*. **2014**, 43, 6062-6096.
3. Krause, S.; Hosono, N.; Kitagawa, S. Chemistry of Soft Porous Crystals: Structural Dynamics and Gas Adsorption Properties. *Angew. Chem. Int. Ed*. **2020**, 59, 15325-15341.
4. Coudert, F.-X.; Jeffroy, M.; Fuchs, A. H.; Boutin, A.; Mellot-Draznieks, C. Thermodynamics of Guest-Induced Structural Transitions in Hybrid Organic-Inorganic Frameworks. *J. Am. Chem. Soc*. **2008**, 130, 14294-14302.
5. Yuan, S.; Feng, L.; Wang, K.; Pang, J.; Bosch, M.; Lollar, C.; Sun, Y.; Qin, J.; Yang, X.; Zhang, P.; Wang, Q.; Zou, L.; Zhang, Y.; Zhang, L.; Fang, Y.; Li, J.; Zhou, H.-C. Stable Metal-Organic Frameworks: Design, Synthesis, and Applications. *Adv. Mater*. **2018**, 30, 1704303.
6. Bon, V.; Kavoosi, N.; Senkovska, I.; Kaskel, S. Tolerance of Flexible MOFs toward Repeated Adsorption Stress. *ACS Appl. Mater. Interfaces*. **2015**, 7, 22292-22300.
7. Haigis, V.; Coudert, F.-X.; Vuilleumier, R.; Boutin, A.; Fuchs, A. H. Hydrothermal Breakdown of Flexible Metal−Organic Frameworks: A Study by First-Principles Molecular Dynamics. *J. Phys. Chem. Lett*. **2015**, 6, 4365-4370.
8. Li, Z.; Fraile, J.; Viñas, C.; Teixidor, F.; Planas, J. G. Post-synthetic modification of a highly flexible 3D soft porous metal–organic framework by incorporating conducting polypyrrole: enhanced MOF stability and capacitance as an electrode material. *Chem. Commum*. **2021**, 57, 2523-2526.
9. Tan, F.; López-Periago, A.; Light, M. E.; Cirera, J.; Ruiz, E.; Borrás, A.; Teixidor, F.; Viñas, C.; Domingo, C.; Plana, J. G. An Unprecedented Stimuli-Controlled Single-Crystal Reversible Phase Transition of a Metal–Organic Framework and Its Application to a Novel Method of Guest Encapsulation. *Adv. Mater*. **2018**, 30, 1800726.
10. Serre, C.; Millange, F.; Thouvenot, C.; Noguès, M.; Marsolier, G.; Louër, D.; Férey, G. Very Large Breathing Effect in the First Nanoporous Chromium(III)-Based Solids: MIL-53 or $Cr^{III}(OH)\cdot\{O_2C{-}C_6H_4{-}CO_2\}\cdot\{HO_2C{-}C_6H_4{-}CO_2H\}_x\cdot H_2O_y$. *J. Am. Chem. Soc*. **2002**, 124, 13519-13526.
11. Loiseau, T.; Serre, C.; Huguenard, C.; Fink, G.; Taulelle, F.; Henry, M.; Bataille, T.; Férey, G. A Rationale for the Large Breathing of the Porous Aluminum Terephthalate (MIL-53) Upon Hydration. *Chem. Eur. J*. **2004**, 10, 1373-1382.
12. Anokhina, E. V.; Vougo-Zanda, M.; Wang, X.; Jacobson, A. J. $In(OH)\cdot BDC0.75BDCH_2$ (BDC = Benzenedicarboxylate), a Hybrid Inorganic-Organic Vernier Structure. *J. Am. Chem. Soc*. **2005**, 127,

15000-15001.

13. Férey, G.; Millange, F.; Morcrette, M.; Serre, C.; Doublet, M.-L.; Grenèche, J.-M.; Tarascon, J.-M. Mixed-Valence Li/Fe-Based Metal–Organic Frameworks with Both Reversible Redox and Sorption Properties. *Angew. Chem. Int. Ed*. **2007**, 46, 3259-3263.
14. Millange, F.; Serre, C.; Guillou, N.; Férey, G.; Walton, R. I. Structural Effects of Solvents on the Breathing of Metal–Organic Frameworks: An In Situ Diffraction Study. *Angew. Chem. Int. Ed*. **2008**, 47, 4100-4105.
15. Springuel-Huet, M.-A.; Nossov, A.; Adem, Z.; Guenneau, F.; Volkringer, C.; Loiseau, T.; Férey, G.; Gédéon, A. ^{129}Xe NMR Study of the Framework Flexibility of the Porous Hybrid MIL-53(Al). *J. Am. Chem. Soc*. **2010**, 132, 11599-11607.
16. Férey, G.; Serre, C. Large breathing effects in three-dimensional porous hybrid matter: facts, analyses, rules and consequences. *Chem. Soc. Rev*. **2009**, 38, 1380-1399.
17. Devic, T.; Horcajada, P.; Serre, C.; Salles, F.; Maurin, G.; Moulin, B.; Heurtaux, D.; Clet, G.; Vimont, A.; Grenèche, J.-M.; Ouay, B. L.; Moreau, F.; Magnier, E.; Filinchuk, Y.; Marrot, J.; Lavalley, J.-C.; Daturi, M.; Férey, G. Functionalization in Flexible Porous Solids: Effects on the Pore Opening and the Host-Guest Interactions. *J. Am. Chem. Soc*. **2010**, 132, 1127-1136.
18. Biswas, S.; Ahnfeldt, T.; Stock, N. New Functionalized Flexible Al-MIL-53-X (X = -Cl, -Br, -CH_3, -NO_2, -$(OH)_2$) Solids: Syntheses, Characterization, Sorption, and Breathing Behavior. *Inorg. Chem*. **2011**, 50, 9518-9526.
19. Ahnfeldt, T.; Gunzelmann, D.; Loiseau, T.; Hirsemann, D.; Senker, J.; Férey, G.; Stock, N. Synthesis and Modification of a Functionalized 3D Open-Framework Structure with MIL-53 Topology. *Inorg. Chem*. **2009**, 48, 3057-3064.
20. Cao, N.; Wang, H.; Ban, Y.; Wang, Y.; Yang, K.; Zhou, Y.; Zhao, M.; Deng, W.; Yang, W. Tuning of Delicate Host–Guest Interactions in Hydrated MIL-53 and Functional Variants for Furfural Capture from Aqueous Solution. *Angew. Chem. Int. Ed*. **2021**, 60, 1629-1634.
21. Martínez, F.; Orcajo, G.; Briones, D.; Leo, P.; Calleja, G. Catalytic advantages of NH2-modified MIL-53(Al) materials for Knoevenagel condensation reaction. *Microporous and Mesoporous Mater*. **2017**, 246, 43-50.
22. Mounfield, W. P.; Walton, K. S. Effect of synthesis solvent on the breathing behavior of MIL-53(Al). *J. Colloid Interface Sci*. **2015**, 447, 33-39.

23. Kundu, T.; Wahiduzzaman, M.; Shah, B. B.; Maurin, G.; Zhao, D. Solvent-Induced Control over Breathing Behavior in Flexible Metal–Organic Frameworks for Natural-Gas Delivery. *Angew. Chem. Int. Ed*. **2019**, 58, 8073-8077.
24. Kim, J. Y.; Zhang, L.; Balderas-Xicohténcatl, R.; Park, J.; Hirscher, M.; Moon, H. R.; Oh, H. Selective Hydrogen Isotope Separation via Breathing Transition in MIL-53(Al). *J. Am. Chem. Soc*. **2017**, 139, 17743-17746.
25. Nagy, M. E.; Aly, M. N.; Gaber, F. A.; Dorrah, M. E. Neutronic behavior of reactor moderated by mixtures of light and heavy waters at different ratios. *Ann. Nucl. Energy*. **2014**, 63, 548-555.
26. Wiberg, K. B. The Deuterium Isotope Effect. *Chem. Rev*. **1955**, 55, 713-743.
27. Schah-Mohammedi, P.; Schenderovich, I. G.; Detering, C.; Limbach, H.-H.; Tolstoy, P. M.; Smirnov, S. N.; Denisov, G. S.; Golubev, N. S. Hydrogen/Deuterium-Isotope Effects on NMR Chemical Shifts and Symmetry of Homoconjugated Hydrogen-Bonded Ions in Polar Solution. *J. Am. Chem. Soc*. **2000**, 122, 12878-12879.
28. Meijer, G.; Meulen, J. J. T.; Andresen, P.; Bath, A. Sensitive quantum state selective detection of H_2O and D_2O by (2+1)-resonance enhanced multiphoton ionization. *J. Chem. Phys*. **1986**, 85, 6914-6922.
29. Xiong, F.; Zhu, W.; Lin, H. An Evanescent Fiber Sensor for Detecting Low-level Content H_2O in D_2O Solutions. *Appl. Mech. Mater*. **2013**, 303, 59-62.
30. Olson, D. L.; Lacey, M. E.; Webb, A. G.; Sweedler, J. V. Nanoliter-Volume ^{1}H NMR Detection Using Periodic Stopped-Flow Capillary Electrophoresis. *Anal. Chem*. **1999**, 71, 3070-3076.
31. Dunning, S. G.; Nuñez, A. J.; Moore, M. D.; Steiner, A.; Lynch, V. M.; Sessler, J. L.; Holiday, B. J.; Humphrey, S. M. A Sensor for Trace H_2O Detection in D_2O. *Chem*. **2017**, 2, 579-589.
32. Luo, Y.; Li, C.; Zhu, W.; Zheng, X.; Huang, Y.; Lu, Z. A Facile Strategy for the Construction of Purely Organic Optical Sensors Capable of Distinguishing D_2O from H_2O. *Angew. Chem. Int. Ed*. **2019**, 58, 6280-6284.
33. Zhang, Y.; Chen, L.; Liu, Z.; Liu, W.; Yuan, M.; Shu, J.; Wang, N.; He, L.; Zhang, J.; Xie, J.; Chen, X.; Diwu, J. Full-Range Ratiometric Detection of D_2O in H_2O by a Heterobimetallic Uranyl/Lanthanide Framework with 4f/5f Bimodal Emission. *ACS Appl. Mater. Interfaces*. **2020**, 12, 16648-16654.
34. Xia, J.; Yu, Y.-L.; Wang, J.-H. Fe^{3+}-Catalyzed low-temperature preparation of multicolor carbon polymer dots with the capability of distinguishing D_2O from H_2O. *Chem. Commum*. **2019**, 55, 12467-12470.

35. Dong, B.; Lu, Y.; Song, W.; Kong, X.; Sun, Y.; Lin, W. A dual-site controlled fluorescent sensor for the facile and fast detection of H_2O in D_2O by two turn-on emission signals. *Chem. Commum*. **2020**, 56, 1191-1194.

36. Sharma, A.; Kim, D.; Park, J.-H.; Rakshit, S.; Seong, J.; Jeong, G. W.; Kwon, O.-H.; Lah, M. S. Mechanistic insight into the sensing of nitroaromatic compounds by metal-organic frameworks. *Commun. Chem.* **2019**, 2, 39.

37. Sharma, A.; Lim, J.; Jeong, S.; Won, S.; Seong, J.; Lee, S.; Kim, Y. S.; Baek, S. B.; Lah, M. S. Superprotonic Conductivity of MOF-808 Achieved by Controlling the Binding Mode of Grafted Sulfamate. *Angew. Chem. Int. Ed*. **2021**, 60,

38. Arvai, A. J.; Nielsen, C. *ADSC Quantum-210 ADX Program*; Area Detector System Corporation: Poway, CA, USA, 1983.

39. Otwinowski Z.; Minor, W. HKL3000 program: *in Methods in Enzymology*, ed. Carter, Jr. C. W.; Sweet, R. M. Academic Press, New York, 1997, vol. 276, part A, pp. 307.

40. Sheldrick, G. M. SHELX program, *Acta Crystallogr. Sect. C*, **2015**, *71*, 3−8.

41. Tang, Y.; Wu, H.; Cao, W.; Cui, Y.; Qian, G. "Luminescent Metal-Organic Frameworks for White LEDs. *Adv. Optical Mater*. **2020**, 2020, 2001817.

42. Ploetz, E.; Engelke, H.; Lächelt, U.; Wuttke, S**.** The Chemistry of Reticular Framework Nanoparticles: MOF, ZIF, and COF Materials. *Adv. Funct. Mater*. **2020**, 30, 1909062.

43. Yue, Y.; Qiao, Z.-A.; Fulvio, P. F.; Binder, A. J.; Tian, C.; Chen, J.; Nelson, K. M.; Zhu, X.; Dai, S. Template-Free Synthesis of Hierarchical Porous Metal-Organic Frameworks. *J. Am. Chem. Soc*. **2013**, 135, 9572-9575.

44. Feng, L.; Wang, K.-Y.; Powell, J.; Zhou, H.-C. Controllable Synthesis of Metal-Organic Frameworks and Their Hierarchical Assemblies. *Matter*, **2019**, 1, 801-824.

45. Sakata, Y.; Furukawa, S.; Kondo, M.; Hirai, K.; Horike, N.; Takashima, Y.; Uehara, H.; Louvain, N.; Milikhov, M.; Tsruoka, T.; Isoda, S.; Kosaka, W.; Sakata, O.; Kitagawa, S. Shape-Memory Nanopores Induced in Coordination Frameworks by Crystal Downsizing. *Science*. **2013**, 339, 193-196.

46. Lee, J. H.; Jeoung S.; Chung, Y. G.; Moon, H. R. Elucidation of flexible metal-organic frameworks: Research progresses and recent developments. *Coord. Chem. Rev*. **2019**, 389, 161-188.

47. Hadjiivanov, K. I.; Panayotov, D. A.; Mihaylov, M. Y.; Ivanova, E. Z.; Chakarova, K. K.; Andonova, S. M.; Drenchev, N. L. Power of Infrared and Raman Spectroscopies to Characterize Metal-Organic

Frameworks and Investigate Their Interaction with Guest Molecules. *Chem. Rev*. **2021**, 121, 1286-1424.

48. Liu, X.; Wang, X.; Kapteijn, F. Water and Metal-Organic Frameworks: From Interaction toward Utilization. *Chem. Rev*. **2020**, 120, 8303-8377.

Acknowledgement

I would like to express my deep and sincere gratitude to my research supervisor, Prof. Myoung Soo Lah for giving me the opportunity to do research and providing invaluable guidance throughout this research. His vast knowledge, diverse vision, scientific ethics, patience, and determination have deeply motivated me throughout my degree. He has taught me the methodology to carry out the research and to present the research works as clearly as possible. It was a great privilege and honor to work and study under his guidance. I would also like to thank him for his helpful nature of being available for students whenever needed, whether for research or personal reasons.

I was very lucky to be the part of such a nice lab with friendly and healthy environment. My thanks to my present lab members, Dr. Seung Bin Baek, Dr. Amitosh Sharama, Somi Won, Seungwan Han, Junmo Seong, Seonghwan Lee for being there for help and exchange of knowledge, both theoretically and experimentally. I also want to appreciate the efforts of my past lab members Minhak Oh, Dr. Dongwook Kim, Dr. Hyehyn Kim, Sunyoung Shin, Dr. Gyounghwa Jeong, and Dr. Seok Jeong to strengthen my knowledge and work during my research.

Finally, I am extremely grateful to my parents for their love, prayers, caring and sacrifices for educating and preparing me for my future. My special thanks to all my friends who have supported me throughout this roller coaster journey to achieve what I wanted.